Pulsed Electron Paramagnetic Resonance

Investigation of Molecular Magnetic Systems



A thesis submitted for the degree of Master by Research

Zhijie Huang

Lead Supervisor: Prof. Lapo Bogani

Co-Supervisor: Dr. Michael Slota

St Anne's College, Department of Materials

Oxford, Trinity term 2023



Abstract

Porphyrins, consisting of four pyrroles connected by methine bridges, can accommodate different types of metal ions or groups in the centre, because the four nitrogen atoms in the molecule function as outstanding ligands. In this thesis, a vanadyl group is incorporated in the centre in order to investigate the electron spin–spin interactions and coherence properties, because the vanadyl group in the nuclear spin-free carbon−sulfide ligands has been found to have a long coherence time. Graphenoids, composed of annulated benzene rings, have the same basic unit of graphene. Because of the delocalisation of electrons in π-conjugation structure, graphenoids have many interesting electronic properties, and therefore have obtained attention from researchers in different fields. Through introducing different defects and side groups in the structures and adjusting the size and shape of the molecules, it is possible to tune the magnetic and coherence properties of graphenoids.

In this thesis, we use electron paramagnetic resonance spectroscopy to investigate the magnetic and coherence properties of an ensemble of isolated paramagnetic molecules. Vanadyl porphyrin dimers with different spacers are discussed, and we especially focus on the electron spin–spin interactions in these molecules. We use strongly and weakly coupled representations to describe the spin systems of triply linked dimers and all other dimers, respectively, because of different strengths of isotropic exchange coupling, compared with both the hyperfine coupling and the electron Zeeman anisotropy. The noncoincidence effects of different interaction tensors play an important role in the CW-EPR spectra and need to be considered in simulations. We also investigated the coherence properties dependence on different exchange coupling strengths and attached side groups. Furthermore, we discuss the temperature dependence of the coherence properties and structural effects on the magnetic

properties by studying two types of graphenoids with two different defects, including two neighbouring five- and seven-membered rings and two disjoint five-membered rings.

Contents

Abstract i

Introduction 1

1. Theories and Concepts 5

1.1 Electron Spin 5

1.2 The Spin Hamiltonian 6

1.3 Quantum Coherence 9

1.4 Density Matrix 10

1.5 Polycyclic Aromatic Hydrocarbons 12

1.5.1 PAHs with armchair-edges 13

1.5.2 PAHs with zigzag-edge 14

1.6 Porphyrins 20

2. Methods 32

2.1 Electron Paramagnetic Resonance (EPR) 32

2.1.1 Continuous-wave EPR 33

2.1.2 Pulsed EPR 36

2.2 Measurement of the spin–spin-relaxation time 39

2.3 Measurement of the spin–lattice-relaxation time 45

2.3.1 Inversion Recovery 45

2.3.2 Picket-Fence pulse sequence 46

2.3.3 Spin–lattice relaxation mechanisms 47

2.4 Rabi oscillations 50

2.5 ESEEM Spectroscopy 51

2.5.1 Two-pulse ESEEM 51

2.5.2 Three-pulse ESEEM 54
2.6 HYSCORE Spectroscopy 56
2.7 DFT calculations of EPR parameters 58
3. Vanadyl Porphyrin dimers 62
3.1 Introduction 62
3.2 Magnetic properties 69
3.3 Spin dynamics 83
3.3.1 Spin–spin relaxation time 83
3.3.2 Spin–lattice relaxation time 89
3.3.3 Rabi oscillations 94
3.3.4 Instantaneous diffusion 97
3.4 Summary 99
3.5 Project Overview 102
4. Benzo-extended open-shell polycyclic aromatic hydrocarbons 103
4.1 Introduction 103
4.2 Magnetic properties 106
4.3 Coherence properties 115
4.4 Summary 121
4.5 Project Overview 124
5. Helical open-shell polycyclic aromatic hydrocarbons 126
5.1 Introduction 126
5.2 Magnetic properties 128
5.3 Coherence properties 134
5.4 Summary 139
5.5 Project Overview 141

6. Conclusions and perspectives 142

Additional data 146

Acknowledgements 147

List of Figures 148

List of Abbreviations 160

Publications 161

References 162

Introduction

A qubit is a fundamental unit to achieve quantum information processing, which can transform the current digital landscape significantly. Currently, there are several types of physical realisations of qubits and superconducting circuit technology is the most excellent one [1]. However, it is limited by the number of operating qubits[2]. The spin qubits, including electronic and nuclear spin qubits, are a new type of physical realization of qubits, which can be used for quantum information processing and attracted a lot of attention. We can use electromagnetic radiation to manipulate the spins. Twenty-five years ago, Kane proposed using spin impurities in semiconductors to do quantum computing [3]. Pla et al. demonstrated that it is possible to manipulate the electron spin qubit constrained in a phosphorus atom doped in silicon [4]. The coherence time in this qubit is up to 200 μs. Furthermore, nowadays, integrated circuit technology has reached an advanced stage. Therefore, it is promising to use the electron spins of phosphorus donor with solid-state qubits is limited by two factors. One is that we cannot control the spatial distribution of defect sites in the host materials very accurately because of the recent synthesis method [5]. Furthermore, we cannot modify the electronic and magnetic properties of the defect sites to scale them up and therefore get a large-scale architecture [5].

Thanks to the fast development of the synthesis method of organic molecules, we now have an alternative approach towards quantum information processing, which uses the electron and nuclear spins in molecules. We can use nuclear magnetic resonance (NMR) spectroscopy to manipulate the nuclear spins. Nuclear spins are less influenced by the environment and have long coherence times. However, it is challenging to tune the interactions between them in molecules [2]. Although electron spins show shorter coherence times than nuclear spins, they can be manipulated much faster using electron paramagnetic

resonance (EPR) spectroscopy. Furthermore, the interactions between electron spins can be tuned easily through molecular design. For example, Freedman group used two spectrally addressable qubits (an early transition metal Ti^{3+} and a late transition metal Cu^{2+}) to achieve single quantum gate operations in transition metal complexes [6].

Some novel chemical systems like graphenoids and porphyrins have recently shown many fascinating properties and promising applications [7,8]. Graphene is an intriguing two-dimensional material composed of sp^2-hybridized carbon atoms. Novoselov and Geim used a micromechanical cleavage approach to isolate graphene and investigated its excellent properties, and they were rewarded with a 2010 Nobel Prize in physics [9]. Graphenoids are novel molecules with the same honeycomb structure as graphene, which has excellent mechanical strength, extreme electrical properties and other unique properties [10]. Quasi-zero-dimensional graphenoids are nanographenes, which are the research subjects of this thesis. However, these graphenoids are very difficult to synthesise because of the limits of existing synthesis methods. Hence, much research on their interesting properties is still lacking and they need more investigations. The previous top-down synthesis method, such as longitudinal unzipping of carbon nanotubes [11], cannot control the edge structures or sizes accurately. However, with the development of more advanced synthesis methods, especially the bottom-up synthesis method, such as synthesis based on precursor molecules [12], nanographenes with atomically accurate structures can now be synthesised [13,14]. For example, chemists can now synthesise graphenoids with desired defects, such as non-hexagonal rings, such as pentagonal and heptagonal rings, and desired shapes regarding curvature, edge shape and size [15]. Therefore, we can investigate the relationship between molecular structure and its magnetic and coherence properties, which is the research emphasis of this thesis. Atomically precise graphenoids are promising to be used as molecular qubits and have already shown large quantum coherence times reported in

previous research [16,17]. Furthermore, such a research of the nanographenes can give insight into quasi-one-dimensional graphenoids, which are also known as graphene nanoribbons, because some nanographenes can be used as the periodic unit of graphene nanoribbons with corresponding edge structures. In contrast to graphene, graphene nanoribbons have finite energy band gaps because of quantum confinement and therefore are promising for novel semiconductors [18].

Another interesting chemical system is porphyrin, specifically vanadyl porphyrin. Porphyrins have attracted a lot of attention from researchers because they are abundant in biological systems and play an important role in biochemical processes. For example, magnesium porphyrin is one important part of chlorophyll, which is vital for photosynthesis [19]. The four nitrogen atoms in a porphyrin make them outstanding ligands to incorporate metal centres. Porphyrins with different metal centres have different interesting functionalities [20]. Recently, vanadyl porphyrins have been synthesised, and they have good coherence times, which means they can be used as qubits for quantum information processing [21]. Although some research on the vanadyl porphyrin monomer has been done recently, there is little research on the vanadyl porphyrin dimers. In this thesis, we have mainly investigated electronic interactions in this dimer, such as isotropic exchange coupling and dipolar coupling, and how different bridges affect them. Our work can significantly contribute to understanding the electronic interactions in more complicated vanadyl porphyrin tapes and rings with more porphyrin units. Furthermore, coherence properties in this family of dimers were also investigated to better understand the relationship between molecular structure and coherence properties. Our work can advance research into operations of two-qubit quantum gates, such as the CNOT gate, using transition-metal-based molecular systems.

This thesis is organised as follows. The first chapter introduces theories and concepts about electron spin and quantum coherence, and structures and properties of novel investigated materials, including polycyclic aromatic hydrocarbons and porphyrins. In the second chapter, we give an introduction of methods to investigate the materials. The experimental methods are the EPR technique, including CW- and pulsed EPR. The theoretical method is density functional theory. In this thesis, we use ORCA quantum chemistry software to calculate EPR-relevant parameters to confirm experimental results. In the third chapter, we discuss the experimental results of the vanadyl porphyrin dimers. We investigated the spin interactions within molecules and put emphasis on the couplings between electron spins. Then the relationship between the isotropic exchange coupling and coherence properties is clarified. Rabi oscillations are used to confirm the total spin in a triply-linked dimer and manipulate the electron spins. In the fourth chapter, we analyse the spin interactions within the benzo-extended open-shell polycyclic aromatic hydrocarbons and the temperature dependence of coherence properties. In the fifth chapter, we study the magnetic and coherence properties of helical open-shell polycyclic aromatic hydrocarbons. In the sixth chapter, we give a conclusion of these three projects and give insights into the future promising research. In the additional data, we present an HYSCORE experimental result and a corresponding simulation result of the *syn*-dimer.

1.Theories and Concepts

In this chapter, some fundamental theories and concepts of this thesis will be introduced. These are mainly physical concepts of EPR and quantum technologies, including electron spin, the spin Hamiltonian, and the density matrix, as well as structures and interesting properties of chemical systems, including polycyclic aromatic hydrocarbons (PAHs) and porphyrins.

1.1 Electron Spin

An electron has a spin quantum number (s), which equals ½, and it has two states corresponding to m_s = 1/2 (spin-up state) and m_s = -1/2 (spin-down state) corresponding to the spinors $\binom{1}{0}$ and $\binom{0}{1}$, respectively. In this thesis, the notation $|1\rangle$ will be used to represent the spin-up state and the notation $|0\rangle$ will be used to represent the spin-down state.

A general spin state can be expressed as the superposition of these two states, which can be mathematically expressed as[22]:

$$|\Psi(t)\rangle = \mathrm{c}_\alpha(t)|0\rangle + \mathrm{c}_\beta(t)|1\rangle, \tag{1.1}$$

Where $c_\alpha(t)$ and $c_\beta(t)$ are the complex coefficients containing amplitude and phase, which obey

$$|\mathrm{c}_\alpha(t)|^2 + \left|\mathrm{c}_\beta(t)\right|^2 = 1. \tag{1.2}$$

The spin angular-momentum operator of an electron ($\hat{\boldsymbol{S}}$) can be decomposed into three orthogonal components: $\hat{S}_x$, $\hat{S}_y$, and $\hat{S}_z$. The corresponding expectation value is

$$\boldsymbol{S} = \langle\Psi|\hat{\boldsymbol{S}}|\Psi\rangle. \tag{1.3}$$

The electron's magnetic moment is as follows:

$$\boldsymbol{\mu_e} = -g_e\mu_B\boldsymbol{S}, \tag{1.4}$$

where g_e stands for the free-electron Landé factor and μ_B stands for the Bohr magneton. The Bohr magneton is defined as:

$$\mu_B = \frac{e\hbar}{2m_e}, \tag{1.5}$$

where e is the electron charge, $\hbar$ is the reduced Plank constant, and m_e is the electron mass.

1.2 The Spin Hamiltonian

The main terms of the spin Hamiltonian involved in this thesis are as follows [23,24]:

$$\hat{H} = \hat{H}_{EZ} + \hat{H}_{HF} + \hat{H}_{ZFS} + \hat{H}_{EX} + \hat{H}_{DD} + \hat{H}_{NZ} =$$
$$\sum_i^N \mu_B \boldsymbol{B}^\dagger \boldsymbol{g} \hat{\boldsymbol{S}}_i + \sum_i^N \hat{\boldsymbol{S}}^\dagger \boldsymbol{A}_i \hat{\boldsymbol{I}}_i + \sum_i^N \hat{\boldsymbol{S}}_i{}^\dagger \boldsymbol{D} \hat{\boldsymbol{S}}_i + \sum_{i \neq j} \hat{\boldsymbol{S}}_i{}^\dagger \boldsymbol{J} \hat{\boldsymbol{S}}_j + \sum_{i \neq j} \hat{\boldsymbol{S}}_i{}^\dagger \boldsymbol{D}_{dip} \hat{\boldsymbol{S}}_j - \sum_i^N \boldsymbol{B}^\dagger \boldsymbol{g}_{n,i} \hat{\boldsymbol{I}}_i \tag{1.6}$$

Here, the electron Zeeman term ($\hat{H}_{EZ}$) describes the interaction between electron spins and the applied magnetic field, where μ_B is the electron Bohr magneton, $\boldsymbol{B}$ is the applied magnetic field, and g is the Landé factor, which is 2.00232 for the free electron. The hyperfine coupling term ($\hat{H}_{HF}$) describes the interactions between electron spins and nuclear spins, where $\boldsymbol{A}$ is the hyperfine coupling tensor, which has Fermi-contact and dipolar components. The Fermi-contact component is isotropic and originates from the electron spin density at the nucleus, whereas the dipolar component is anisotropic and originates from the electron spin residing at other places and interacting with the nuclear spin through dipolar interactions. Their expressions are as follows:

$$\hat{H}_{\mathrm{HF,dd}} = \frac{\mu_0}{4\pi r^3} g \mu_B g_n \mu_n \left[\frac{3}{r^2} \left(\hat{\boldsymbol{S}}\boldsymbol{r}\right)^\dagger \left(\hat{\boldsymbol{I}}\boldsymbol{r}\right) - \hat{\boldsymbol{S}}^\dagger \hat{\boldsymbol{I}}\right], \tag{1.7}$$

$$\hat{H}_{\mathrm{HF,contact}} = \frac{2\mu_0}{3} g \mu_B g_n \mu_n |\Psi_0(0)|^2 \hat{\boldsymbol{S}}^\dagger \hat{\boldsymbol{I}}, \tag{1.8}$$

where μ_0 is the vacuum permeability, g_n is the nuclear g factor, μ_B is the electron's Bohr magneton, μ_n is the nuclear Bohr magneton, r is the distance between the electron and the

nuclear spin, and $|\psi_0(0)|^2$ is the spin density at the nucleus. The spin density $|\psi_0(0)|^2$ and nucleus g factor can determine the sign of the isotropic hyperfine coupling. $\hat{\boldsymbol{I}}$ represents nuclear spins, r is the distance between the electron and nuclear spins, and $\boldsymbol{r}$ is the corresponding vector. All other parameters in these two equations have been introduced in the previous part. In the case of rapid tumbling in a liquid solution, where the dipolar term can be averaged to zero, and the hyperfine coupling is isotropic, the expression can be further reduced to:

$$\hat{H}_{\mathrm{HF}} = \hat{H}_{\mathrm{HF,contact}} = \frac{2\mu_0}{3} g\mu_B g_n \mu_n |\Psi_0(0)|^2 \hat{S}_Z \hat{I}_Z. \tag{1.9}$$

If there are several nuclear hyperfine couplings, they can be added algebraically as follows:

$$\hat{H}_{\mathrm{HF}} = \sum_i^N a_{\mathrm{iso},i} \hat{S}_Z \hat{I}_Z, \tag{1.10}$$

where $a_{\mathrm{iso}} = \frac{2\mu_0}{3} g\mu_{\mathrm{B}} g_{\mathrm{n}} \mu_{\mathrm{n}} |\Psi_0(0)|^2$.

The parameter D is the zero-field splitting tensor, which describes the energy-splitting strength without an applied magnetic field. The physical origin of the zero-field splitting can be dipole–dipole interactions or the second-order effect of spin–orbit coupling in a spin system with $s > 1/2$. In its eigenframe, this term can be diagonalised and reduced to:

$$\hat{H}_{\mathrm{ZFS}} = D\left(\hat{S}_z^2 - \frac{S(S+1)}{3}\right) + E(\hat{S}_x^2 - \hat{S}_y^2), \tag{1.11}$$

where $D = 3/2D_z$ and $E = (D_x - D_y)/2$.

The parameter J is the exchange-coupling term, which describes the exchange-interaction strength between two electron spins. In this thesis, I consider only the most critical isotropic term in graphenoids. Therefore, in this case, this term can be reduced to

$$\hat{H}_{\mathrm{ex}} = J\hat{\boldsymbol{S}}_1^T \hat{\boldsymbol{S}}_2, \tag{1.12}$$

where to a first-order approximation J can be expressed as follows:

$$J = -2\left\langle \phi_a(1)\phi_b(2) \middle| \frac{e^2}{4\pi\varepsilon_0 r} \middle| \phi_a(1)\phi_b(2) \right\rangle, \tag{1.13}$$

where ϕ_a and ϕ_b are the normalised spatial molecular orbitals, ε_0 is the vacuum permittivity, and r is the distance between electrons. Therefore, the J-coupling strength depends on the overlap of the electron spins through the chemical bond.

In porphyrin dimeric structures, because of g-anisotropy[6], J is an anisotropic term and can be expressed as:

$$J_{\mathrm{iso}} = (J_a + J_b + J_c)/3, \tag{1.14}$$

where J_a, J_b, and J_c are the principle values of the corresponding J tensor.

A system with two coupled spins is described with a singlet and a triplet state. When $J > 0$, the ground state is the singlet state. Otherwise, the ground state is the triplet state.

Furthermore, $\boldsymbol{D}_{\mathrm{dip}}$ is the dipolar-interaction tensor of two electron spins. The expression of the corresponding spin Hamiltonian is:

$$\widehat{H}_{\mathrm{DD}} = \frac{\mu_0}{4\pi r^3} g_1 g_2 \mu_B^2 [\widehat{\boldsymbol{S}}_1^T \widehat{\boldsymbol{S}}_2 - \frac{3}{r^2} (\widehat{\boldsymbol{S}}_1 \boldsymbol{r})^T (\widehat{\boldsymbol{S}}_2 \boldsymbol{r})], \tag{1.15}$$

where g_1 and g_2 are the g-factors of these two electron spins, and r is the distance between them.

In most cases, in the high-field approximation, the electron Zeeman interaction is much larger than the electron dipolar interaction. Then this term can be reduced to:

$$\widehat{H}_{\mathrm{DD}} = \frac{\mu_0}{4\pi r^3} g_1 g_2 \mu_B^2 (1 - 3\cos^2\theta) \hat{S}_{1z} \hat{S}_{2z}, \tag{1.16}$$

where $\hat{S}_{1z}$ and $\hat{S}_{2z}$ are the z components of two electron-spin operators, and θ is the angle between the two electron spins. In summary, the exchange coupling is determined by the overlap of the orbitals of the unpaired electrons. However, the dipolar coupling is not through bond and is determined by the distance between the unpaired electrons. The last term is the nuclear Zeeman interaction, which describes the interaction between a nuclear spin and the applied magnetic field. The energy splittings for electrons and nuclei are $g\mu_{\mathrm{B}}B_0$ and $g_{\mathrm{n}}\mu_{\mathrm{B}}B_0$, respectively.

Since the electron g factor and nuclear g factor are usually of the same order of magnitude, the electron magneton $\mu_{\mathrm{B}} = \frac{e\hbar}{2m_{\mathrm{e}}}$ is usually three orders of magnitude larger than the nuclear magneton $\mu_{\mathrm{n}} = \frac{e\hbar}{2m_{\mathrm{n}}}$ because of the much smaller mass of the electron compared with the nuclei, which gives much larger energy splittings for electrons than for nuclei. So, these splittings are usually not observable in EPR spectra. Rather than being excited by microwave radiation (GHz), the nuclear transitions are excited by radio frequency radiation (MHz).

1.3 Quantum Coherence

Classical computers store and process information in binary "0" and "1" states. A potential quantum computer can use superposition states, such as $a|0\rangle + b|1\rangle$. The number of states that can be represented simultaneously grows exponentially as the number of qubits increases because of superposition. During the quantum-operation process, the same operation is performed on all the possible states at the same time and achieve quantum parallelism, which would lead to a speedup in computation speed compared with classical computing, such as implemented in Shor's algorithm for integer factorization[25].

As shown in Figure 1.1, the Bloch sphere can visually show quantum states. The two poles of the Bloch sphere correspond to standard basis vectors $|0\rangle$ and $|1\rangle$, respectively. Each point on the sphere surface corresponds to a pure quantum state $|\Psi\rangle$, which can be mathematically described as

$$|\Psi\rangle = \cos(\theta/2)|0\rangle + \mathrm{e}^{\mathrm{i}\varphi}\sin(\theta/2)|1\rangle. \quad (1.17)$$

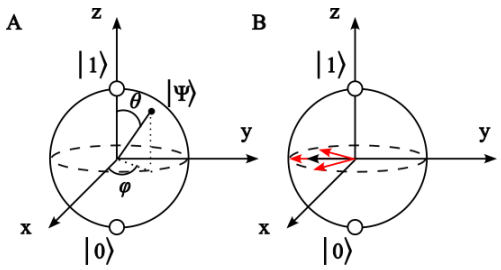

Figure 1.1 Schematic illustration of the Bloch sphere and a general pure quantum state (A) and the mixed quantum state of a decoherent ensemble (B). When the individual spins are in alignment, the spin state of the system is in a pure state and can be represented by a point on the surface of the Bloch sphere. However, if the individual spins are not in alignment, it is in a mixed state and can be represented by a point inside the Bloch sphere.

$|\Psi\rangle$ represents a general qubit state, θ encodes the components of the superposition state in each of the two eigenstates, and φ is the phase of this qubit state. When the two-level quantum system begins to lose coherence because of interaction with the environment, the pure state becomes a mixed state, which could be represented as the points inside the Bloch sphere. And the mathematical description is similar to equation 1.17, except that there is an additional parameter *k*,

$$|\Psi\rangle = k[\cos\left(\frac{\theta}{2}\right)|0\rangle + e^{i\varphi}\sin(\theta/2)|1\rangle], \tag{1.18}$$

where *k* represents the length of the vector representing this mixed state and is smaller than one.

1.4 Density Matrix

An ensemble of identical quantum systems is more conveniently described by the density-matrix approach. According to the definition, the density matrix is the outer product of the wave function and its conjugate [22]. For an ensemble, the density matrix can be described as

$$\rho(t) = |\Psi\rangle\langle\Psi| = \sum_k p_k \, |\Psi_k(t)\rangle\langle\Psi_k(t)|, \tag{1.19}$$

where p_k is the fraction of the Ψ_k state in this spin ensemble [22]. For each state in this spin ensemble, the density matrix can be expressed as

$$\rho(t) = |\Psi(t)\rangle\langle\Psi(t)| = \sum \rho_{mn}(t) \, |n\rangle\langle m|, \tag{1.20}$$

where $\rho_{mn}(t)$ represents the matrix elements and evolves with time [22]. Coherences are given by off-diagonal elements in the density matrix, which represent the superposition between different energy levels. Populations are given in diagonal elements, which represent the possibility of the ensemble in one of these states.

The Liouville–von Neumann equation describes the dynamic behaviour of a quantum system:[26]

$$i\hbar \frac{\partial \hat{\rho}}{\partial t} = [\hat{H}, \hat{\rho}]. \tag{1.21}$$

The solution can be reduced to such a form

$$\hat{\rho}(t) = \hat{U}(t)\hat{\rho}(0)\hat{U}^{-1}(t), \tag{1.22}$$

where $\hat{U}(t)$ represents the evolution operator.

When $\hat{H}$ is time-independent, such as the spin Hamiltonian when the flip-flop processes of the electron spins and nuclear spins are very slow, the mathematical description of $\hat{U}(t)$ can be further reduced to the following simple form[27]

$$\hat{U}(t) = e^{-i\hat{H}t}. \tag{1.23}$$

1.5 Polycyclic Aromatic Hydrocarbons

Polycyclic aromatic hydrocarbons are molecules that have many periodically annulated benzene rings and are also called molecular graphene. They have more than one benzene ring with a structure size between 1 and 5 nm. In 1964, Clar proposed the important sextet rule, which are now used to predict the stability of aromatic systems. The sextet rule states that although there can be many resonant structures for an aromatic system, the resonant structure with the largest number of sextet rings is the most stable and contributes the most to the structure. In 1921, Crocker put forward the concept of the aromatic sextet and showed that the sextet of the valence electrons can lead to the benzene's aromatic stability [28]. Then in 1931, Pauling et al. [29] posited that the benzene's aromatic stability is because of the delocalised π electrons that can be represented by valence bond representations, namely resonance structures, and the increasing number of resonance structures lead to stability, as the delocalized electrons are distributed more evenly across the entire molecule. Furthermore, Doering [30] showed the $4n+2$ rule that if a conjugated molecule has $4n+2$ conjugated electrons, it will be aromatic, but if a conjugated molecule has $4n$ conjugated electrons, it will be antiaromatic. Here, n takes integer values.

PAHs have attracted much attention from several scientific fields because of their interesting electronic and optoelectronic properties. For example, this type of π-conjugated system can be functionalised by molecular design. Recently, many π-conjugated systems have been designed as organic field-effect transistors (FETs). These devices are essential and promising building units for flexible and cheap organic circuits. They can be used also as a platform to investigate the structure–property relationship, such as the mobility of carriers in the π-conjugated system and the ratio of on-state to off-state current. Figure 1.2 shows some typical edge structures.

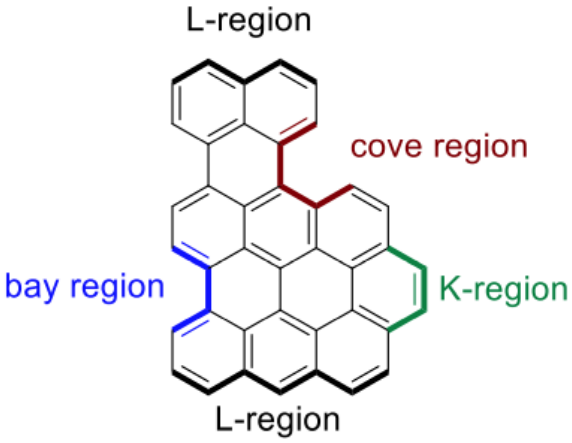

Figure 1.2 Schematic of four typical periphery structures of PAHs, including bay region, L-region, K-region, and cove-region. Figure adapted from Ref. [8].

1.5.1 PAHs with armchair-edges

Figure 1.3 shows the chemical structure of a typical PAH with armchair edges, which is hexa-peri-benzocoronene (p-HBC). In 1995, Müllen et al.[31] reported that they used mild experimental conditions to produce hexa-peri-benzocoronene (p-HBC) effectively. Since then, many kinds of PAHs with armchair edges have been synthesised. Different aliphatic chains with different geometries attached to the PAHs could improve the solubility and contribute to the organization process, as shown in Figure 1.4.

Wu et al. [10] showed that monomers in solution can compile into columnar assembly because of the π-interactions between them. Then, nanophase separation process can make the columns become a super-molecular organization. The intercolumn volume in the super-molecular organization is filled by alkyl side groups.

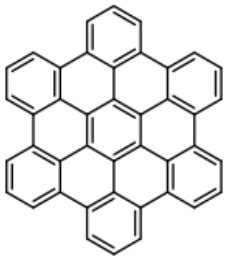

Figure 1.3 Chemical structure of the hexa-peri-benzocoronene (p-HBC) [8].

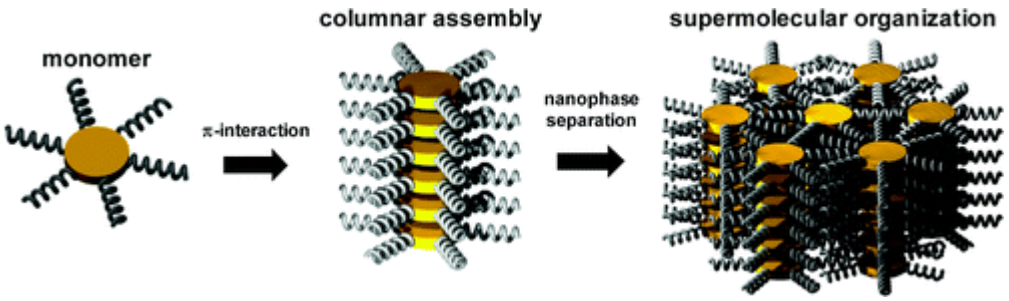

Figure 1.4 Schematic diagram of the organisation of alkyl-substituted PAHs. First, monomers stack into columns through π-interaction. Then, columns group into a super-molecular organisation through nanophase separation. Figure adapted from Ref. [10].

1.5.2 PAHs with zigzag-edge

Chemists can get partial zigzag-edge PAHs by adding extra benzene rings onto the bay region of the structure. For example, Kastler et al. [32] synthesised a family of partially zigzag PAHs by inducing phenanthrenyl units into precursors. When the periphery of the PAH changes from armchair to zigzag, the symmetry of the molecule changes, inducing a change in its electronic properties. However, the number or type of alkyl side groups do not have a significant influence on the electronic properties.

Another important zigzag PAH is an acene with benzene rings fused in the linear direction. There is a strong relationship between the number of benzene rings in [n]acenes and their electronic properties. Specifically, lower [n]acenes usually are insulators and higher [n]acenes are semiconductors or even metallic conductors[33]. Pentacene is such a type of zigzag PAH; because of its instability in air and under light, its synthesis and application as a semiconductor have been hindered significantly. However, Herwig et al. [33] proposed a new method to synthesise pentacene in the solid states. Figure 1.5 shows the chemical structure of the pentacene.

Recently, Zuzak et al.[34] used on-surface dehydrogenation method to synthesise undecacenes. High-resolution non-contact AFM imaging was used to observe the structures of these molecules, and scanning tunnelling spectroscopy (STS) was used to measure the transport gap in these molecules. Figure 1.6 shows the on-surface dehydrogenation method used to synthesise this family of molecules.

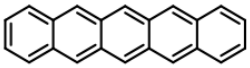

Figure 1.5 Chemical structure of the pentacene.

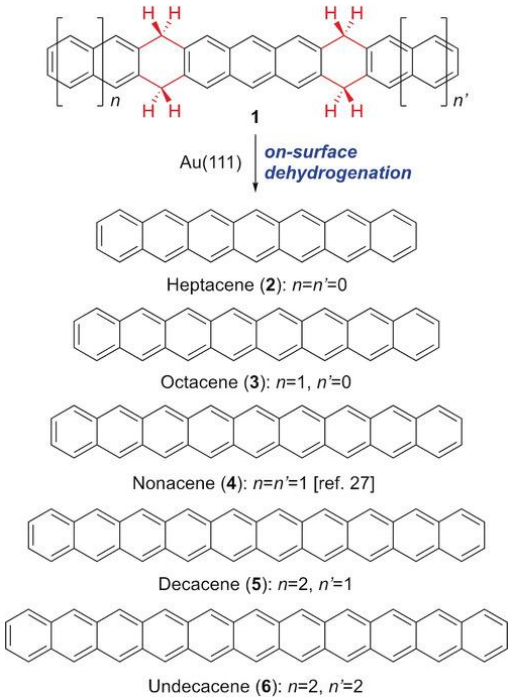

Figure 1.6 Heptacene, Octacene, nonacene, decacene, and undecacene synthesised using on-surface methods. Figure adapted from Ref. [34].

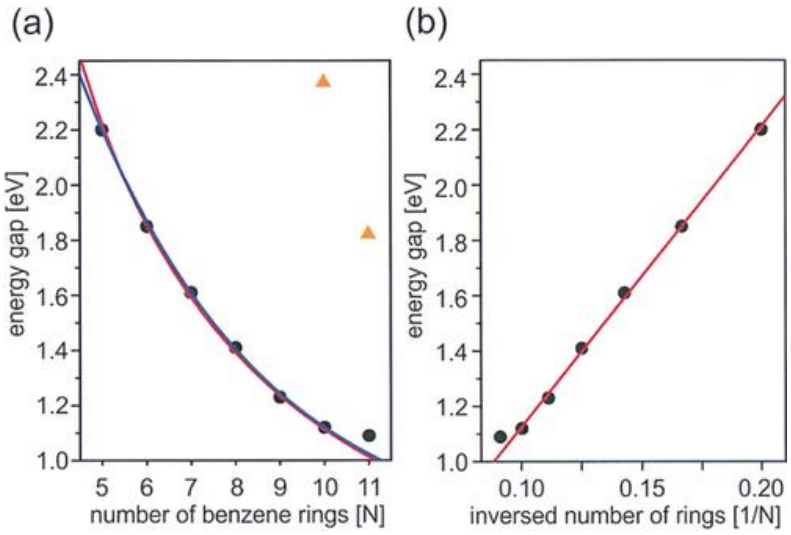

Figure 1.7 (a) The energy gap versus the number of benzene rings in a series of acenes with the fit results, blue line: exponential model, red line: inverse model. (b) The inversed number of rings versus the energy gap in a series of acenes with the fit results. Figure adapted from Ref. [34].

Figure 1.7 shows the energy gap measured by STS for this series of acenes. There is an exponential or inverse relationship between the number of benzene rings in the acenes and the energy gap. This research demonstrated that long acenes can be synthesised using the hydroacene precursors, and other long and interesting acenes might also be synthesised using this advanced method.

Electronic properties and chemical stability can be modified by the peripheral structures[15]. For example, molecules with zigzag edges usually show a large HOMO–LUMO gap and have good chemical stability. However, the molecules with armchair edges always have a small HOMO–LUMO gap, are chemically unstable, and easily deteriorate under ambient conditions. Furthermore, heteroatom doping is the other essential method to modify the properties of PAHs effectively[35]. For example, heteroatom doping can be used to tune the HOMO–LUMO gap, optical absorption spectra, and electron-spin distributions, depending on the type, placement, and number of heteroatom donors in the structure.

However, current synthesis methods cannot achieve atomically precise doping, and many challenges regarding synthesis need to be overcome to use heteroatom doping to tune the properties of PAHs[36].

Figure 1.8 shows the chemical structures of phenalene and its nitrogen-doped derivatives, with doped nitrogen at different positions of the structure. The structure 4a is a neutral diradical structure, while its resonance structure 4b is a zwitterionic structure. The nitrogen–carbon bond is similar to a double bond since their bond lengths are similar. Moreover, the neighbouring carbon atoms contribute most to the excess spin density in the triplet state. The other fascinating aspect is that these molecules are the core unit of zigzag graphene nanoribbons, which are very promising for spintronics.

Open-shell PAHs are the subject of investigation in this thesis since they have unpaired electrons in their structures[37]. Investigation of their magnetic and quantum properties is still in the infantile stage and needs researchers to carry out. It is fascinating to explore the relationship between molecular structure and both magnetic and coherence properties. However, their open-shell structures make PAHs very unstable and requires strict conditions to synthesise[37].

So far, the synthesis of PAHs has two routes, the aromatic-core extension method and the two-stage synthesis method[8]. First, the core-extension method is also known as the annulative π-extension (APEX) reaction, which is essential for the diversification of PAHs[8]. Figure 1.9 shows one of the mainstream approaches of the APEX reaction, which uses the hexaphenylbenzene molecule to synthesise hexabenzocoronene (HBC) through a cyclodehydrogenation reaction.

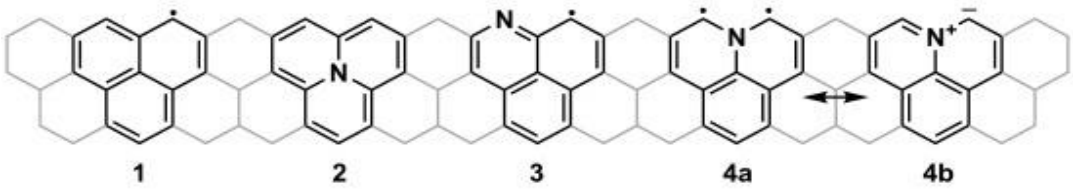

Figure 1.8 Chemical structures of phenalene 1 and three aza derivatives 2–4. 2, 3, and 4 (4a and 4b) have a doped N atom at different positions of the structure. 4a and 4b are two resonance structures of the same molecule. Figure adapted from Ref. [38].

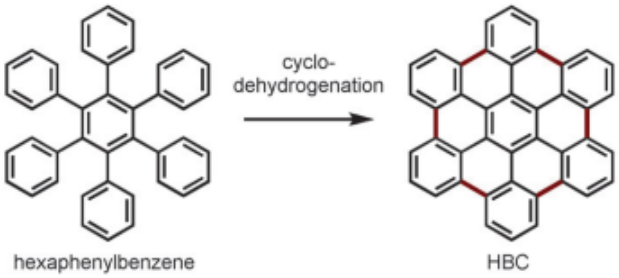

Figure 1.9 One typical employed APEX method of PAHs. A hexaphenylbenzene molecule is used to synthesise a hexabenzocoronene (HBC) through the cyclo-dehydrogenation reaction. Figure adapted from Ref. [8].

Furthermore, the two-stage synthesis method generally includes a precursor synthesis stage and a cyclodehydrogenation stage. The precursor synthesis uses benzenes and other basic small molecules to form important precursors. Cyclodehydrogenation is then used to form ring-fused π-conjugation systems. This method includes on-surface synthesis and solution-mediated synthesis. So far, the two-stage method is the best and most widely used method to synthesize novel PAHs.

Recently, PAHs have been used as a new type of molecule to hold qubits for quantum information processing[39]. Figure 1.10 shows the four types of strategies to obtain qubits in carbon-based materials. The top-left graph is a single electronic spin in a carbon nanotube,

and the coherence time is around 30 ns[40]. The top-right is the structure of a fullerene with a heteroatom inside. The coherence time is around 70 μs[41]. The bottom-left graph is the structure of functionalized GNR with the nitronyl nitroxide (NIT) radical. Slota et al.[42] used stable, spin-bearing NIT radicals to inject electron-spin density into the graphene nanoribbons. They found the predicted delocalized magnetic edge states by comparing the CW-EPR spectra of NIT-GNR with the non-graphitized reference molecule NIT-polyphenylene using multi-frequency EPR spectroscopy. Furthermore, they investigated the spin–spin interactions for the radical spins along the GNR and found good fits. The coherence time is around 3 μs. In 2019, Lombardi et al. tailored the sp^2-carbon framework to obtain the molecular graphenoids with two unpaired electrons. They investigated the spin–spin interactions within the structure, relaxation mechanisms, and coherence properties. They investigated effect of the environment on the coherence time of the molecules by using different solvents, including d-toluene and CS_2. In a CS_2 solvent, because of the nonactive nuclei, the coherence time is much larger than that in a d-toluene solvent. The coherence time reaches 0.24 ms in a CS_2 solvent with dynamical decoupling at 120 K. Furthermore, they performed nutation experiments to get the Rabi oscillations, showing that the qubits within this molecule can be manipulated to any arbitrary state.

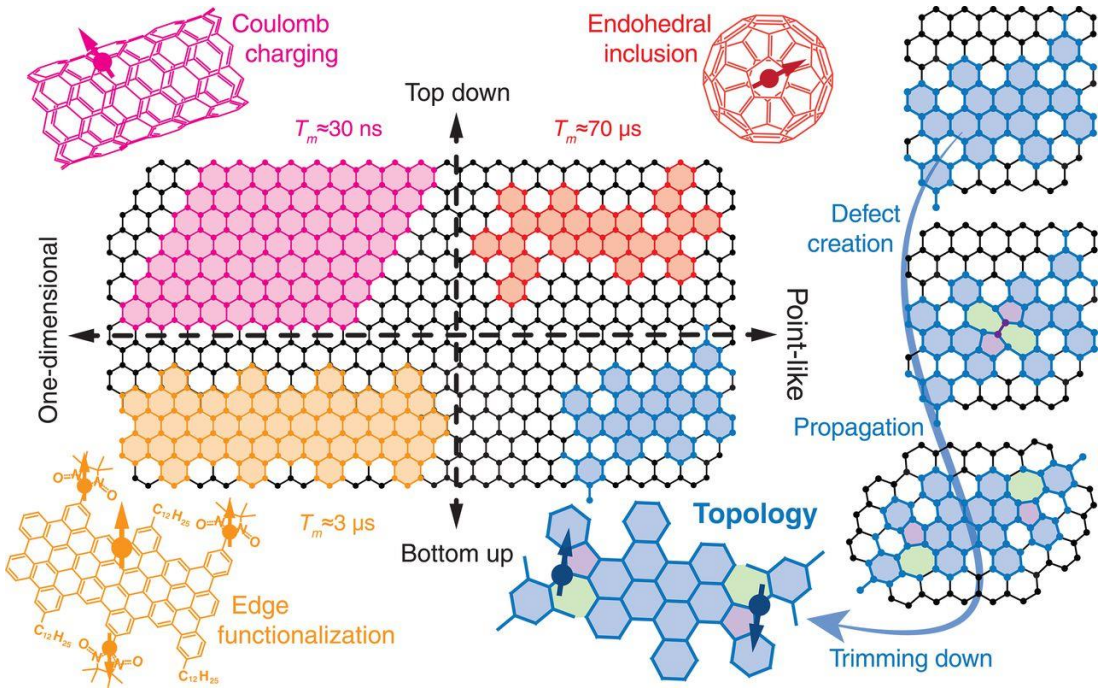

Figure 1.10 Quantum units in carbon-based materials with different strategies, including coulomb charging in nanotubes, endohedral inclusion in C_{60} molecules, edge functionalization of GNRs, and defects in graphenoids. Figure adapted from Ref. [39].

1.6 Porphyrins

Porphyrins are class of molecules universal in biological systems that play an important role in life on Earth. For example, haemoglobin contains a porphyrin with an iron ion in the center, which is the red pigment found in red blood cells [43].

This molecule transports oxygen from the lungs to tissues and removes carbon dioxide from tissues to the lungs [44]. In the structure of a porphyrin, there are four pyrrole units whose α positions are connected by methine bridges. The left image in Figure 1.11 shows the simplest porphyrin structure, porphine, whose periphery is all occupied by hydrogen atoms (hydrogen atoms here are omitted for clarity). The carbon locants on the macrocycle are as follows: the carbon in the methine bridge is the *meso*-carbon, the quarternary carbon is the α-carbon, and the pyrrole carbon is the β-carbon. Because of the

four nitrogen atoms in the structure, various metal atoms or other groups can be incorporated into the cavity of the structure to create various kinds of interesting metalloporphyrins. At the same time, we can modify the functionality of the porphyrin by introducing metal ions or other groups.

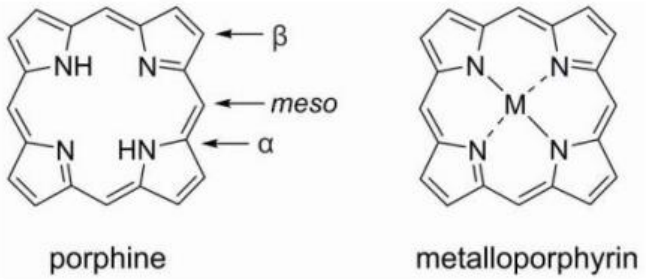

Figure 1.11 The chemical structures of a porphyrin and a related metalloporphyrin. The α-, β-, and meso-carbon are shown in the left schematic of porphine structure. M represents a metal ion incorporated in the right schematic of metalloporphyrin structure. Figure adapted from Ref. [20].

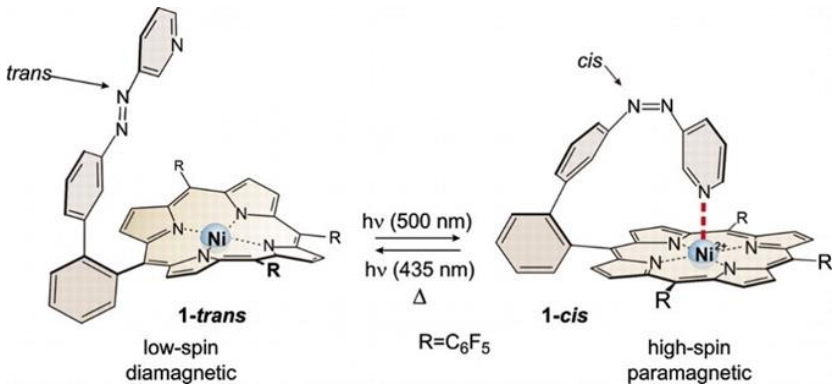

Figure 1.12 Azopyridine functionalised Ni-porphyrin with light-induced magnetic-switching properties. The left one is the low-spin diamagnetic structure and the right one is the high-spin paramagnetic structure. Under blue-green radiation (500 nm), the low-spin state transforms to a high-spin state. However, under violet-blue radiation (435 nm), the high-spin state transforms to a low-spin state. Figure adapted from Ref. [45].

For example, Venkataramani et al. [45] used nickel(II) porphyrin to switch the magnetic properties in this structure using light. Under blue-green radiation (500 nm), this molecule transforms from a *trans* structure to a *cis* structure [45]. At the same time, this molecule transforms from a low-spin state ($s = 0$) to a high-spin state ($s = 1$), because Ni^{2+} tends to form a low-spin state ($s = 0$) in a planar structure but forms a high-spin state ($s = 1$) in a square pyramidal structure [45]. More interestingly, this process can be reversed by using violet-blue light (435 nm) [45]. Furthermore, this process can be repeated thousands of times without degradation [45]. The transformation between a low- and high-spin state is shown in Figure 1.12.

The copper(II) porphyrins have been used as biochemical rulers in pulsed double electron–electron resonance (DEER) to test the accuracy of this technique. For example, Bowen et al. [46] used orientation-selective DEER to probe a family of porphyrin-based Cu–Cu dimers and porphyrin-based Cu–nitroxides, as shown in Figure 1.13.

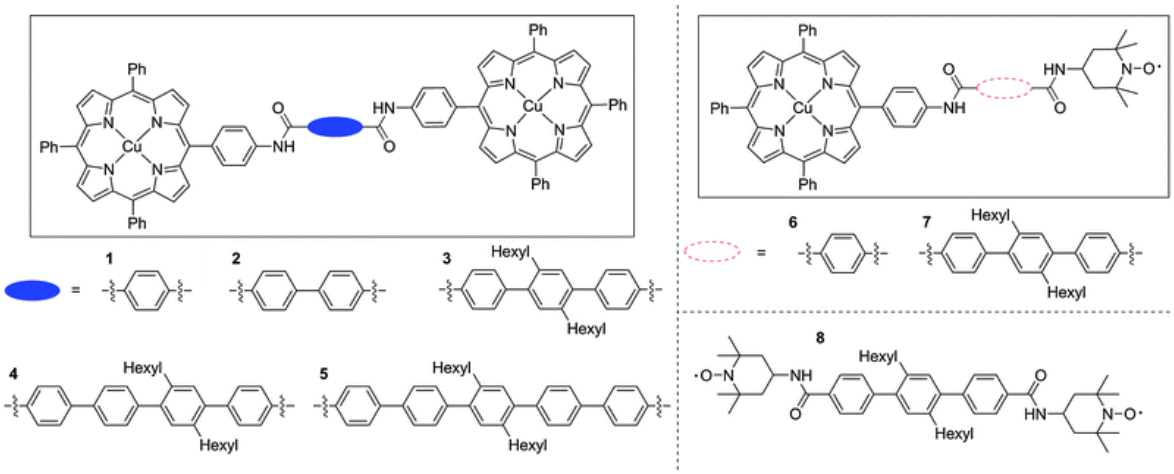

Figure 1.13 Chemical structures of the copper(II)-based molecules. 1, 2, 3, 4, and 5 are the bridges used in porphyrin-based Cu–Cu dimers. 6 and 7 are the bridges used in porphyrin-based Cu–nitroxide. 8 is a nitroxide–nitroxide molecule. Figure adapted from Ref. [46].

Their research demonstrated that data from orientation-selective DEER, via using a parameterised model that accounts for the flexibility, specifically the rotation freedom, of a spin system, can give useful information about a system's structure. Nowadays, researchers can use a template-directed strategy to construct complex porphyrin nanorings. In this method, coordination interactions between the porphyrin and a template induce metalloporphyrin precursors, and then these metalloporphyrin precursors interact with each other to get the cyclic multi-porphyrin molecule [47].

Wang et al. gave a good review of this templated-directed synthesis method [47]. The template-directed synthesis method can successfully make large-size macrocycles and mechanically interlocked molecules. For example, the Anderson group has successfully synthesised a lot of interesting porphyrin oligomers using this method [48,49]. Figure 1.14 shows some of these interesting chemical structures. The left one is a double-strand, conjugated zinc-porphyrin ladder. Anderson group used ^{1}H NMR spectra to confirm the structure of these molecules. The middle one is a zinc-porphyrin nanoring also synthesised by his group[48]. In the past, researchers have synthesised a lot of belt-shaped porphyrin rings because these rings have interesting electronic π delocalization over the surfaces of their structures. However, most such rings do not have a π-delocalization pathway around the whole macrocycle. In this project, the Anderson group used a template-directed trimerization of a zinc porphyrin dimer to produce a π-conjugated porphyrin nanoring. The schematic on the right of Figure 1.14 shows a porphyrin nanotube. Six zinc porphyrin dimers are connected by the template-directed coupling reaction to form twelve carbon–carbon bonds. This porphyrin nanotube structure has a volume of 4.5 nm^3. The conjugation intensity is greater than that of the six zinc porphyrin rings [50]. The bindings between the coordination sites of the zinc porphyrins and the ligands is the most important point in creating these structures. Because of their highly symmetrical structure and π-conjugated

properties, zinc porphyrins have numerous applications in supramolecular self-assembly, photonics and molecular electronics.

Svatek et al. [51] used electrospray to deposit the zinc porphyrin rings to an Au surface, where three-dimensional stacks formed. By using scanning tunnelling microscopy (STM), they measured the heights of these three-dimensional stacks and found that they have one to four layers of zinc porphyrin rings, with each layer having a height of around 0.32 nm. The flexibility of zinc porphyrin rings leads to a shape deviating from a circle, but as the number of stacking rings increases, the bending stiffness also increases. So, this research has opened up the possibility of using noncovalent interactions between molecules to modify the mechanical properties and shape of macromolecules.

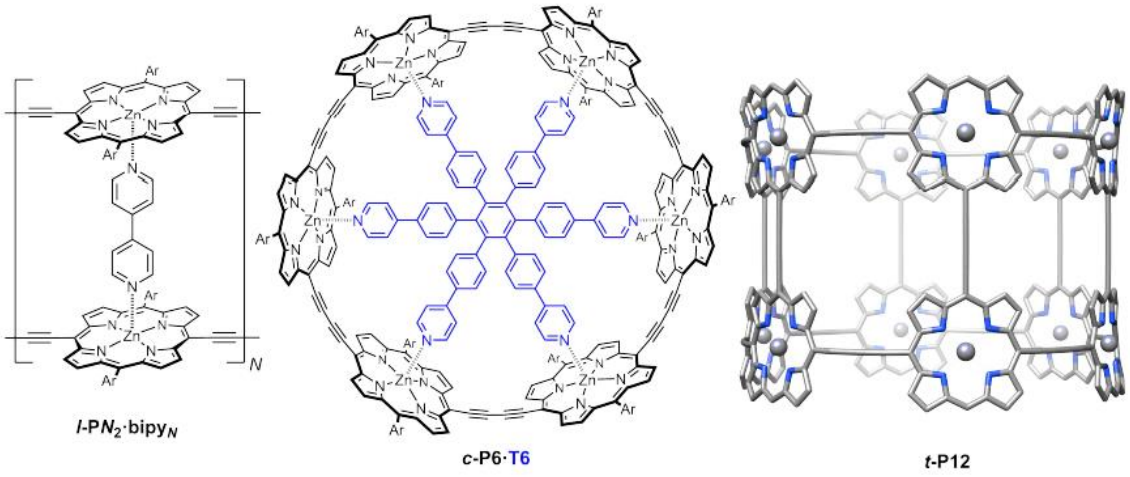

Figure 1.14 Chemical structures of a porphyrin ladder, a porphyrin nanoring, and a porphyrin nanotube. Two strands of porphyrins are connected by 4,4'-bipyridine molecules in the Zn-porphyrin ladder. Six Zn-porphyrin molecules are linked by butadiynes and a hexapyridyl ligand. The nanotube is composed of twelve Zn-porphyrin molecules, and every porphyrin molecule is π conjugated to three neighbouring porphyrin molecules. Figure adapted from Ref. [48-50].

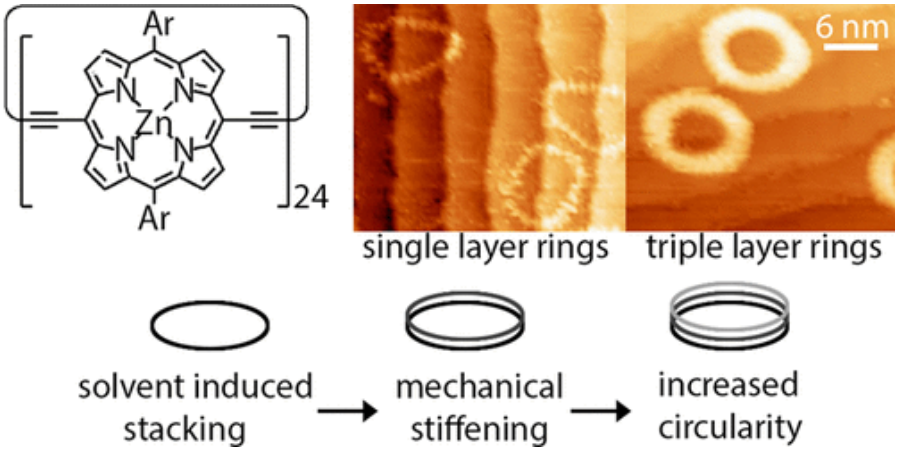

Figure 1.15 Chemical structure of the porphyrin ring, the scanning tunnelling microscopy (STM) images of the single-layer rings and triple-layer rings, and the influence of the stacking process on the shape and mechanical properties of the macromolecular aggregates. Figure adapted from Ref. [51].

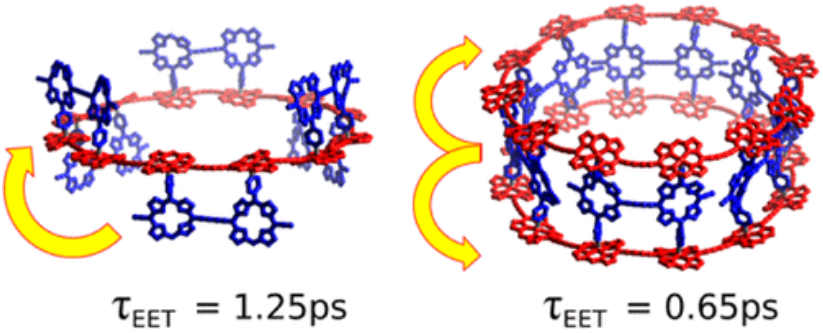

Figure 1.16 The schematic diagrams of the double- and triple-stranded complexes and their respective energy transfer times. The energy transfer time of double-stranded complexes is 1.25 ps. However, that of the triple-stranded complexes is much shorter, 0.65 ps. Figure adapted from Ref. [52].

Figure 1.15 displays the chemical structure of the porphyrin ring used in their research and the STM images of the single-layer and triple-layer porphyrin rings. Furthermore, this figure shows us the influence of stacking on the shape and mechanical properties of the macromolecular aggregates. Porphyrin rings can be used to make

supramolecular multistrand nanorings to mimic the energy transfer in the natural light-harvesting process.

Parkinson et al. [52] used the zinc porphyrin nanorings to create light-harvesting supramolecular complexes. The interesting property relies on their energy-transfer rate, which is on the sub-picosecond scale and can compete with the natural light-harvesting system. Figure 1.16 displays the schematic diagrams of these two complexes. The energy-transfer time of the double-stranded complex is around two times that of the triple-stranded complex, which confirms the multidirectional energy-funnelling process in the triple-stranded complexes. This research shows that these zinc porphyrin-based complexes could be applied in solar harvesting.

The porphyrin nanorings have another intriguing application involved in host–guest chemistry. The porphyrin nanorings can be used to form cyclic multi-porphyrins, which have large cavities and can bind large guest molecules inside. For example, Song et al. [53] synthesised two types of hexameric hosts. One has three zinc porphyrins and three free base porphyrins, but the other one has six zinc porphyrins. The guest molecules they used are tripyridyl arene (TP) and dipyridyl-substituted free-base (DPFb) porphyrin, as shown in Figure 1.17.

In this host–guest structure, the dative bonding between the pyridyl and zinc contributes to the connection between the host and the guest. Song et al. also investigated energy transfer rate, pathways, and mechanisms among the host and guest. This research opens up the possibility of efficient light harvesting with the host structure and then transferring the energy to the trapping site-guest structure [53].

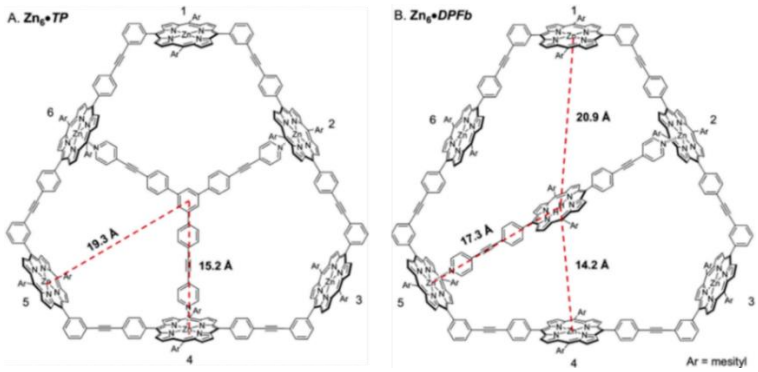

Figure 1.17 A: Chemical structure of a hexameric porphyrin with a guest of tripyridyl arene (TP) B: Chemical structure of a hexameric porphyrin with a guest of dipyridyl-substituted free base porphyrin (DPFb). Figure adapted from Ref. [53].

The porphyrins can be typically connected in two patterns. One is connected by a linker, and the linker could be *p*-phenylene, *o*-phenylene, *m*-phenylene, vinylene, ethynylene, butadiynylene, and so on. The other one is fused. Figure 1.18 shows these two patterns. Research interest in porphyrin dimers has two aspects. One aspect is both the unpaired electron-spin density distributions within dimeric structures and the electron spin–spin interactions. The other aspect is potential applications of porphyrin dimers in molecular electronics, such as single-molecule transport: they can be used as building blocks for molecular electron-spin-based quantum-information processing, such as a two-qubit CNOT gate operation.

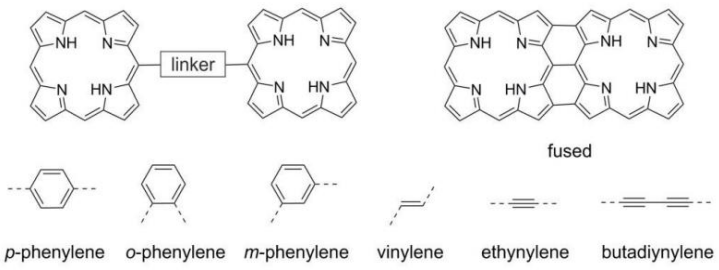

Figure 1.18 The porphyrin dimer structures with different linkers on the left and the fused porphyrin dimer structure on the right. The linkers are shown at the bottom. Figure adapted from Ref. [54].

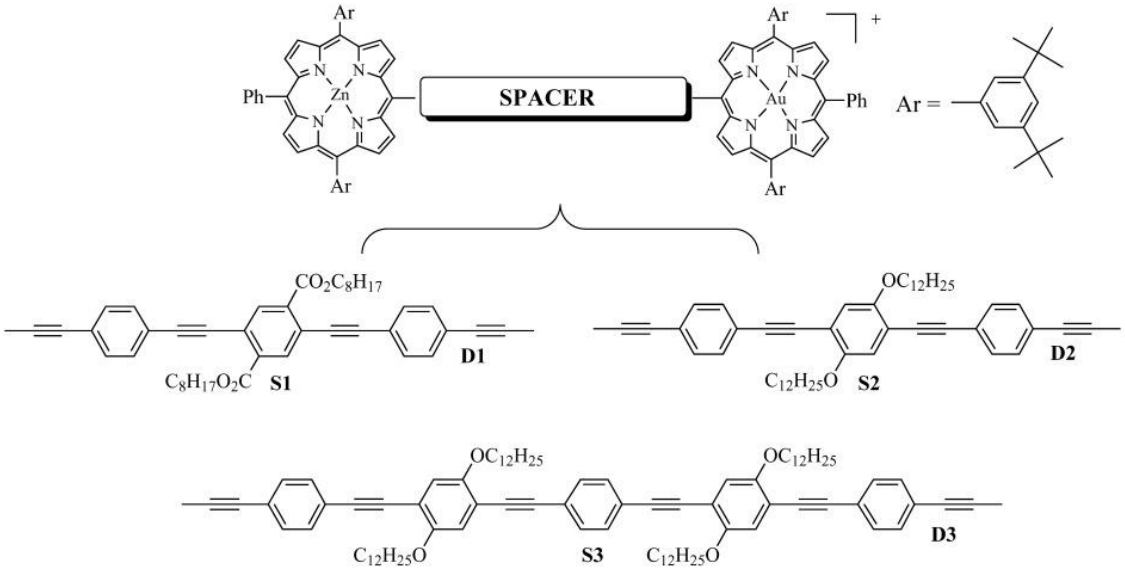

Figure 1.19 Chemical structures of the heterometallated porphyrin dyads (D1, D2, and D3) with different spacers (S1, S2, and S3). Figure adapted from Ref. [55].

The previous research mainly used zinc porphyrin to create supramolecules because zinc has many advantages, such as high stability, and ease to characterize. Nowadays, people turn to use all kinds of transition metals or lanthanides as the core metal ions in the porphyrin structure. Homometallated porphyrins can be used to make linear, cyclic, and polymeric complexes. Hence, heterometallated porphyrin complexes have become a very interesting research topic recently.

Odobel et al.[55] synthesised a series of zinc(II)-gold(III) bisporphyrins. The structures are shown in Figure 1.19. They investigated two triaryl porphyrins bridged in the *meso* position by an alkyne spacer. The distance between the two porphyrins' centres varies from 3.2 nm to 4.5 nm. The electronic interactions between the porphyrin rings are very strong because of the direct connection of the porphyrin rings through the alkyne spacer. Subjecting zinc porphyrin to light at room temperature can transform the dyad from the ZnP–S–AuP$^+$ state to the $^{+\bullet}$ZnP–S–AuP$^\bullet$ state. This new state exists for hundreds of

picoseconds, and returns to the ground state through an intermediate triplet ZnP state. Gold porphyrin can also be excited, and this process transfers energy to the triplet ZnP. This research shows that energy can be transferred quickly and efficiently in the bis-porphyrin structure over a long distance by means of a light excitation process.

Quantum-information processing

Nowadays, thanks to the progress of bottom-up synthesis methods, it has become possible to fabricate atomically precise molecules. So, we can fine-tune the environment of qubits and qubit–qubit interactions by adjusting the structure of molecules, which makes possible quantum-gate operations using molecular electron spins based on transition metals.

Recently, Kugelgen et al. [6] created a family of molecules containing two different qubits with different *g* factors. Cu(II) is a heavy transition metal with a *g* factor larger than 2, and Ti(III) is a light transition metal with a *g* factor smaller than 2. When under the same magnetic field, the two metal ions have electron spins with different Zeeman energies. Hence, it is possible to control these two qubits separately using microwaves with different frequencies. Figure 1.20 shows both the XRD structures of this family of molecules with different spacer lengths and their corresponding CW spectra in organic solutions using X-band at 77 K. In order to obtain good fits, they first did the fits of Cu(II) and Ti(III) monomer structures to obtain the *g* factor, hyperfine couplings of the metals, and the linewidths. Then they fit the CW-ERP spectra of these dyad structures by keeping these three parameters fixed and allowing the electron spin–spin interactions to vary within reasonable ranges. The reason is that these three parameters are negligibly influenced by interactions between the two metal ions in the dyad structures, and this treatment reduces the unknown parameters and get fit results easier without losing accuracy. After that, they investigated the spin–lattice relaxation time and coherence time. They used pulse sequences to do single-qubit gate

operations, such as a NOT gate, on both the monomers containing only Ti(III) or Cu(II) and dyads containing both Ti(III) and Cu(II).

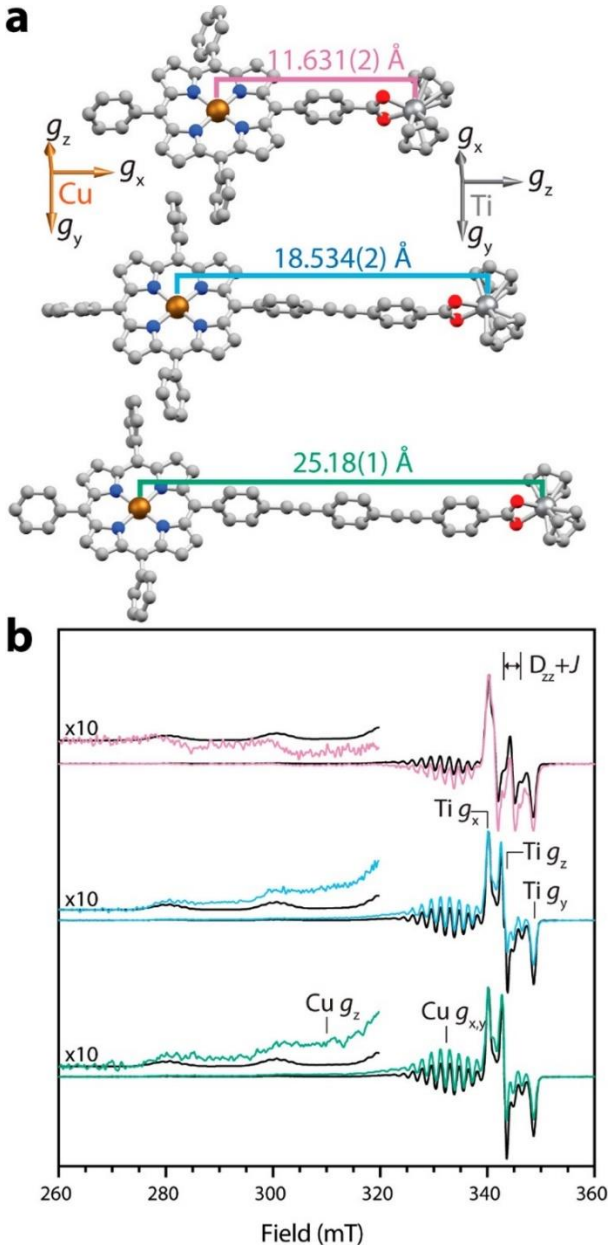

Figure 1.20 a: XRD structure of these three molecules containing Cu(II) and Ti(III) with different separation distances. The *g* tensor frames of unpaired electron spins of Cu and Ti atoms are shown in the graph, respectively. b: The CW-EPR spectra of these three molecules using X-band in solution state at 77 K, respectively. Figure adapted from Ref. [6].

Figure 1.21 (a) shows the nutation experiments they did to manipulate the qubits in these molecules. Figure 1.21 (b) shows the pulse sequences they used to read out the $\langle S_x \rangle$,

<S_y>, and <S_z> components, respectively. Figure 1.21 (c) describes two specific density matrices to compare the ideal and experimental density matrices. Figure 1.21 (d) represents the fidelity of the single-qubit gate operations, including $+x$, $-x$, $+y$, $-y$, $+z$, $-z$, and the Hadamard gate, in all these molecules. They demonstrated that the introduced electron spin in a dyad would not cause the other electron spin to lose coherence because of different resonance frequencies of the two electron spins, and thus in a modular two-qubit system, it is possible to manipulate the electron spins individually.

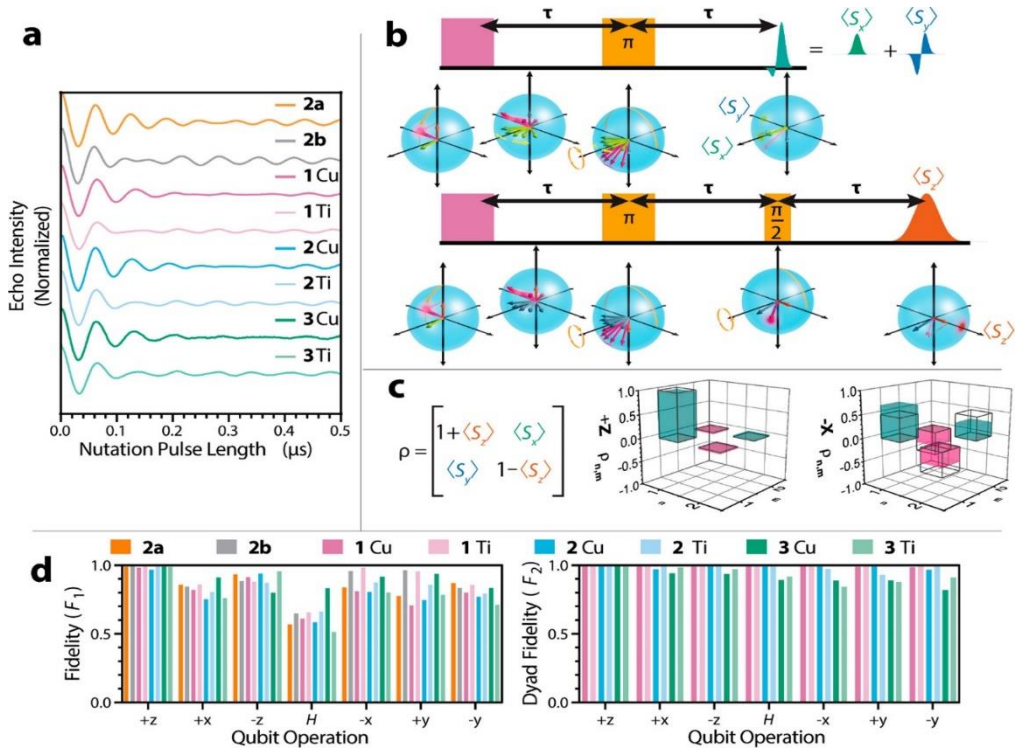

Figure 1.21 (a) Nutation experiments of unpaired electron spins for these molecules, (2a: Cu-only complex, 2b: Ti-only complex). (b) Pulse sequences used to extract <S_x>, <S_y>, and <S_z> and the Bloch representation of these pulse sequences. (c) Density matrices for ideal density matrices (black outline) and the measured density matrices (colour filling), respectively. (d) The fidelity graphs of the monomers and dyads for these molecules. Figure adapted from Ref. [6].

2.Methods

2.1 Electron Paramagnetic Resonance (EPR)

In order to explain the Zeeman effect clearly, we take a spin-1/2 system without couplings with nuclear spins as an example. The m_S = 1/2 and m_S = −1/2 states have two energies in an external magnetic field. The m_S = 1/2 state has a higher energy than m_S = −1/2 state. The energy difference is proportional to the strength of the magnetic field. The populations of these two states follow the Boltzmann distribution. Under microwave radiation, a spin transition can occur when both the microwave frequency is resonant with the energy difference and the selection rules $\Delta S = 0$ and $\Delta m_S = \pm 1$ are satisfied. Figure 2.1 shows the energy splitting of a spin-1/2 system and the derivative-like absorption spectrum at X-band for a free electron with g = 2.0023.

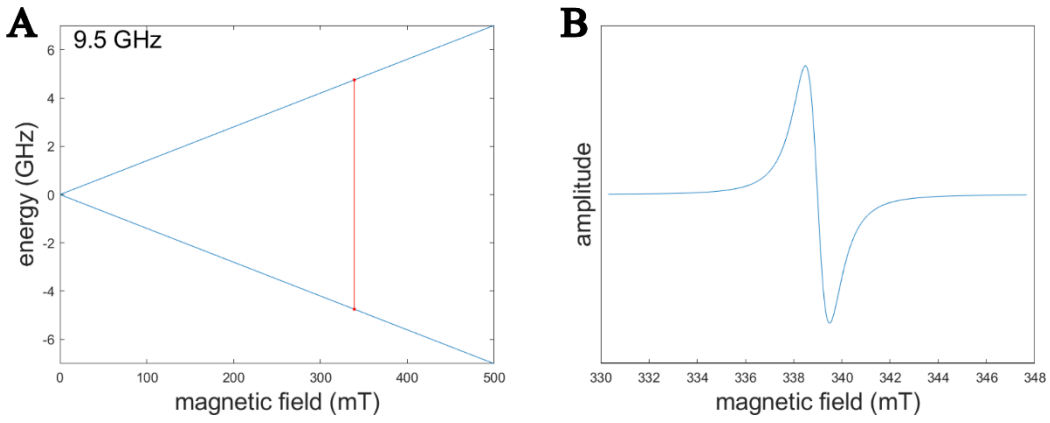

Figure 2.1 (A) Diagram of energy levels of a spin-1/2 system in a magnetic field at X-band (9.5 GHz). The red line represents the transition frequency. (B) The corresponding derivative-like absorption spectrum.

2.1.1 Continuous-wave EPR

In a continuous-wave EPR experiment (CW-EPR), the microwave frequency is kept constant, while the magnetic field is swept. When the transition condition is satisfied at certain magnetic-field positions, there is an absorption signal in the spectrum. All these lines constitute a CW-EPR spectrum. The basic components of an EPR instrument include a magnet (providing the magnetic field with strength in the tesla range), a microwave source (providing microwaves with frequencies in the GHz range), a cryostat (controlling the temperature of the sample from 4 K to 293 K), a detection system (detecting the microwave power after it penetrates the sample), a resonator (creating a magnetic field B_1 at the position of the sample), a lock-in amplifier (filtering out other frequencies or phases of signals in the spectrum), and a circulator (ensuring that only the reflected microwave can reach the detector). Figure 2.2 shows the schematic diagram of a CW-EPR spectrometer.

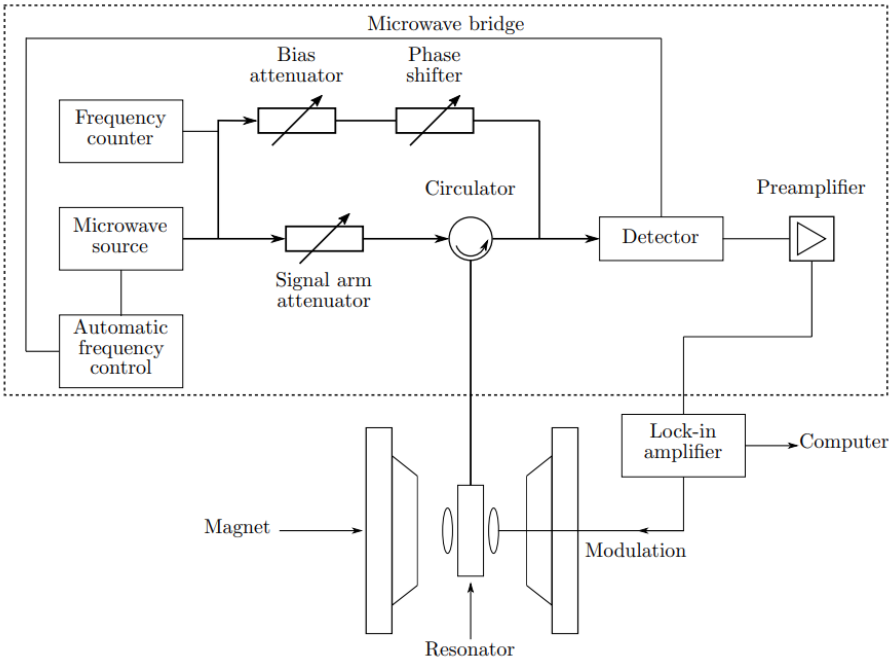

Figure 2.2 Schematic diagram of a CW-EPR spectrometer. The function of each individual part of CW-EPR spectrometer is described in the main text. Figure adapted from Ref. [26].

The frequencies of the microwave usually used include 9.5 GHz (X band), 34 GHz (Q band), and 94 GHz (W band). A proportion of generated microwaves go into the signal arm of the microwave bridge, and the remaining microwaves go into the reference arm of the microwave bridge. The microwave power in the signal arm goes through waveguides into the resonator cavity. The signal arm attenuator here adjusts the power of the microwave. The circulator directs the microwave power in the signal arm to the resonator and the reflected microwave power to the detection system. The microwave power in the reference arm is adjusted by the bias attenuator, and the relative phase of the microwave in the signal and reference arm can be adjusted by the phase shifter. At very low microwave powers, the detector could not work according to the square law. Hence, the reference arm is to keep the detection microwave power above a minimum value to work normally. The additional microwave power offered by the reference arm is called bias, which is normally set to achieve a detector current of 200 μA[56].

The cavity concentrates the microwave at the sample, whose quality factor is defined as Q

$$Q = \frac{\nu_{\mathrm{res}}}{\Delta\nu} = \frac{2\pi * \text{stored energy}}{\text{dissipated energy per cycle}} . \tag{2.1}$$

The Q factor scales with the energy stored in the resonator and the sensitivity of the detection of the signal. A high Q value is demanded in CW mode to get a high-quality CW spectrum, while a low Q value is usually required in Pulse mode to excite a large bandwidth of spins with different resonant frequencies. The Q value in a measurement is adjusted by adjusting the iris arm in the instrument since the iris influences the coupling of the resonator to the waveguide. When the resonator is critically coupled, the Q factor is very large, around 6000. However, when the resonator is over coupled, Q factor decreases to around 100.

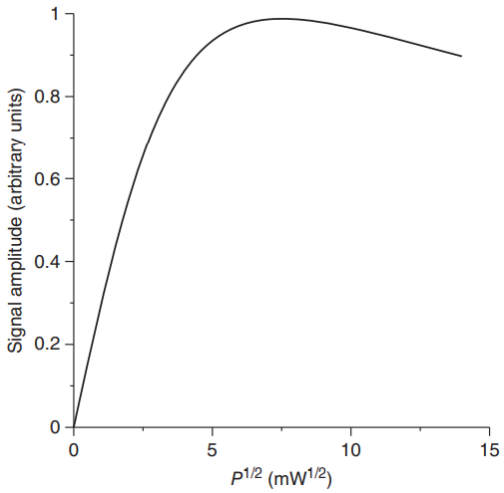

Figure 2.3 The amplitude of CW-EPR signal dependence on the microwave power. When the microwave power is small, the signal amplitude is proportional to the square root of the microwave power. However, when the microwave power is above a certain threshold, the signal decreases as the microwave power increases. Figure adapted from Ref. [26].

A standing wave at the resonant frequency of the resonator is created inside the resonator, and the maximum magnetic field is right at the position of the sample. After being generated by the microwave source, the microwaves go through the waveguide, are redirected by the circulator, and enter the resonator.

The magnet generates the external magnetic field B_0. The side coils in the resonator modulate the magnetic field with a modulation strength ΔB. The lock-in amplifier mixes the signal from the signal and reference arms, enhancing the signal-to-noise ratio scaling with modulation strength ΔB. However, the modulation strength should be smaller than 1/3 of the linewidth of the signal in order to keep the signal not distorted. The resulting signal becomes a sinusoidal modulation and has a first-derivative-like shape.

Figure 2.3 shows the amplitude of a CW-EPR signal depending on the microwave power, which is divided into two parts, including a linear range and a saturation range. In the linear range at low power, the signal amplitude is proportional to the square root of the

microwave power. In contrast, this law breaks down because of the saturation problem at high power. In the saturation range, the rate of the microwave-induced transition is larger than the relaxation rate.

In order to fit a CW-EPR spectrum, there are several steps to consider. First, we need to establish a spin Hamiltonian for n electron spin with electron spins S interacting with N nuclei with nuclear spins I according to the material's structure. Then, we need to consider the material and experiment's conditions. For example, whether the material is measured in solid state, including powders, single crystals, and frozen solutions, or in solution states, in which we need to distinguish between slow, intermediate and fast motions. Then we can check the literature to get similar material's spin parameters to get the dominating spin Hamiltonian, which could contribute to the ESR spectra as well as reasonable values for these dominating spin Hamiltonian parameters. We also need to establish all the tensors' frames and rotate them onto the molecular frame. Furthermore, we can use DFT calculation results as references for some complex systems.

2.1.2 Pulsed EPR

The crucial difference between the pulsed and CW-EPR is that in pulsed EPR, a sequence of pulses in the ns timescale is used rather than a continuous microwave irradiation. A TWT (Travelling Wave Tube) is used to amplify the microwave power. The pulse duration, strength and phases can be tuned in each channel ($+x$, $-x$, $+y$, $-y$). The Q factor in pulsed mode is usually around 100, much smaller than in CW mode, to minimise the duration of the ringdown of the pulse and avoiding destroy the instrument, especially for a short relaxing sample. The ringdown is the process that the energy of microwave restored in the resonator decreases exponentially. During the process of the ringdown, the dissipating energy goes

from the resonator into the detector. The typical ringdown time for an over-coupled resonator is around 100 ns.

The amplitudes of the ringdown and pulses are relatively large, which are rather destructive to the detector. Therefore, a protection pulse must be set up to prevent these damages, but it could not be too long to cover the FID or echo signal. The pulse lengths usually employed are in the range of 8–1000 ns. According to the empirical equation between bandwidth $\Delta\nu$ and pulse length t_p: $\Delta\nu = 1.2/t_p$. The corresponding bandwidth is in the range of 1–150 MHz.

Figure 2.4 shows the schematic diagram of a pulse EPR spectrometer. The pulses are formed by turning on the PIN (P-type Intrinsic N-type) diode with fixed amplitudes and phases ($+x$, $-x$, $+y$, $-y$). The amplitudes of these pulses are low; therefore, they need to be amplified by the TWTA (Travelling Wave Tube Amplifier).

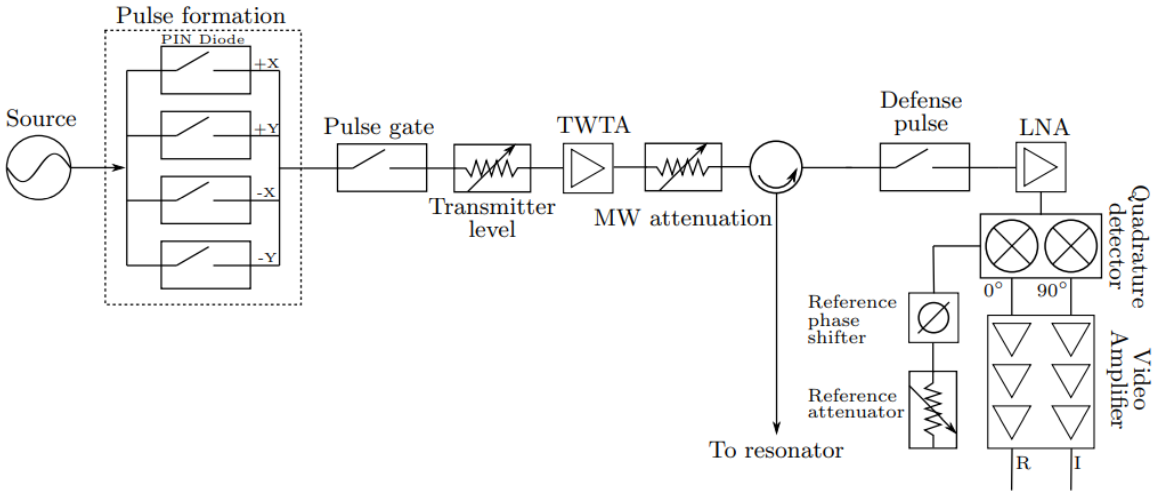

Figure 2.4 Schematic diagram of a pulsed EPR spectrometer. The function of each individual part of the pulsed EPR is shown in the main text. Figure adapted from Ref. [17].

The transmitter level is used to adjust the power of the pulses going into the TWTA. When the powers of the pulses are amplified by the TWTA, we can use the MW attenuation to decrease the power to the amplitude we want exactly. When we decrease the amplitude of the microwave by 6 dB, the power of the mw could be doubled. The power of the reflected pulses and ringdown of the pulses are quite strong, which would destroy the LNA (Low Noise Amplifier), so there is a defence pulse to protect the detection system. After the signal is amplified by the LNA, the signal enters the quadrature detector. The reference arm is used to add a bias current of 200 μA to make the detector work in the linear regime.

2.2 Measurement of the spin–spin-relaxation time

The spin–spin relaxation time (T_m) is obtained by the Hahn echo pulse sequence, as shown in Figure 2.5. First, a π/2 pulse along the *x*-axis (along the *y*-axis is similar) is used to rotate the equilibrium magnetization of the electron spin ensemble from the +*z* direction to the −*y* direction in the rotating frame. Then, during the first delay time *τ*, spin packets with different resonance frequencies begin to fan out in the *xy* plane. The on-resonance spin packet remains in the −*y* direction, while the spin packets with higher resonance frequencies rotate anti-clockwise, and the ones with lower resonance frequencies rotate clockwise in the *xy*-plane. Then, another π pulse along the *x*-axis is applied to rotate all the spin packets by 180°, which makes the spin packets with higher resonance frequencies lag behind the ones with lower resonance frequencies. After another delay time *τ*, the spin packets with higher frequencies catch up with the ones with lower frequencies at the +*y* direction and form an echo there.

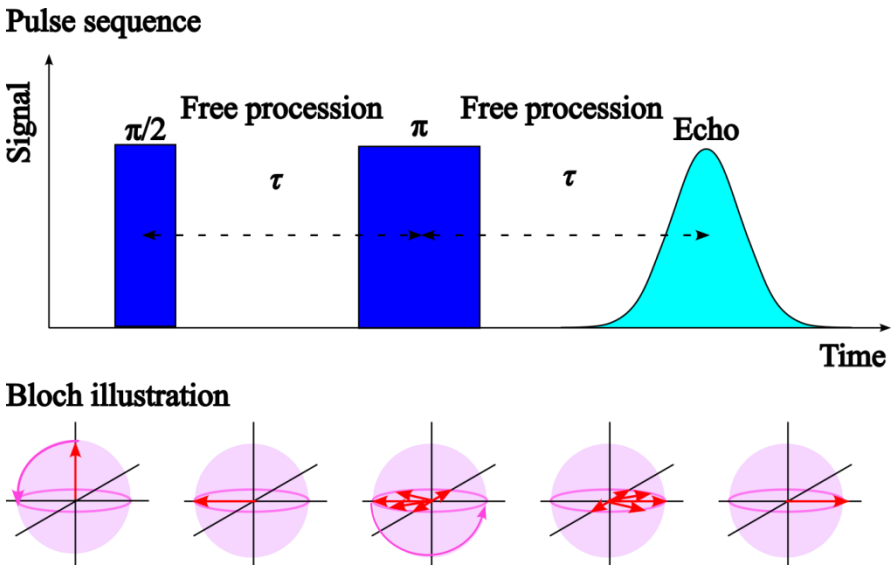

Figure 2.5 The pulse sequence of Hahn echo and its corresponding illustration in the Bloch sphere. The π/2-pulse rotate a spin from +*z* direction to the *xy*-plane, and the π-pulse invert a spin's orientation in the xy plane.

By increasing the delay time τ stepwise, we could get the time trace of the echo signal strength. Phenomenologically, T_m can be extracted from the time trace using such a stretched-exponential model

$$Y(2\tau) = Ae^{-\left(2\tau/T_m\right)^{\beta}}, \tag{2.2}$$

where A represents a factor, β represents a stretched parameter indicating the reasons causing spin–spin relaxation, T_m represents the spin–spin relaxation time, $Y(2\tau)$ is the signal strength at time 2τ, 2τ is the interim time. The A, β, and T_m are free parameters. If there are strong nuclei modulations in the time trace, in order to extract the nuclei modulations, Fourier transformation of the time traces can be done and we obtained the main nuclear modulation frequency and fit the time traces with such an improved model:

$$Y(2\tau) = Ae^{-\left(2\tau/T_m\right)^{\beta}}[1 + k_1\sin(\omega\tau + \varphi_1) + k_2\sin(2\omega\tau + \varphi_2)], \tag{2.3}$$

where ω represents the nuclei frequency, 2ω represents the first harmonic of the nuclear frequency, k_1 and k_2 are modulation depths, and φ_1 and φ_2 represent the phase shifts.

Spin–spin-relaxation mechanisms

The spin–spin-relaxation time T_2 is the actual coherence time of an individual quantum system. During the measurement, we need to use microwave pulses to measure the T_2, and the pulses have some inhomogeneity problems, so the coherence time we obtain is actually T_2^*. If we use advanced methods to suppress the inhomogeneities, such as CPMG pulse, the coherence time we obtain is T_m for an ensemble. The relationship between them is $T_2^* \leqslant T_m \leqslant T_2$[17]. If there are no nuclear spins in the spin system, the spin–spin relaxation can also be affected by the dipolar interactions between electron spins. In this case, the spin–spin

relaxation time depends on the average distance between electrons and has such an equation[27]:

$$T_m = C r_{\mathrm{avg}}^3, \tag{2.4}$$

where C is a constant, r_{avg} is the average distance between unpaired electrons.

Several decoherence channels exist in a specific case, including spectral diffusion, instantaneous diffusion and spin–lattice relaxation. The instantaneous diffusion means that if one spin α in the ensemble is excited by the pulse and its neighbouring spin β is also excited during the same pulse, so after the pulse, spin α will have a different resonance frequency because of the changed dipolar coupling between spin α and β compared with its resonance frequency before the pulse. There are two methods to decrease such an effect to increase T_{m}. One is to decrease the concentration of the paramagnetic molecules in the solvent. The other one is to use an extrapolation experiment by decreasing the flip angle, the fraction of on-resonance spins equivalently, stepwise in the Hahn echo to extract the T_{m}. The instantaneous diffusion rate has a relationship with the concentration of electron spins and the flip angle. The mathematical expression is as follows[27]:

$$\frac{1}{T_{\mathrm{ID}}} = C \frac{\pi}{9\sqrt{3}} \frac{\mu_0 g_1 g_2 \beta_e^2}{\hbar} \sin^2 \frac{\theta}{2}, \tag{2.5}$$

where T_{ID} represents the decay rate of coherence because of the instantaneous diffusion, C represents the concentration of the electron spins, g_1 and g_2 represent the g factor of the observed spin and excited spin, respectively, and θ represents the flip angle.

The spectral diffusion describes the phenomenon that during the free-precession time, the stochastic flip-flop process of neighbouring nuclear spins or electron spins contributes to the change of the spin's resonance frequency. Most spin systems usually have magnetic nuclear spins. In this case, the nuclear flip flops, also known as nuclear spin diffusion, might influence the dephasing of electron coherence significantly. Previously, researchers used deuterated solvents for the solution sample to decrease the magnetic noise from nuclear spins

and increase the T_m significantly, because a ^2H nucleus has a much smaller gyromagnetic ratio than a ^1H nucleus. Furthermore, researchers found that the nuclear spin diffusion process almost does not depend on temperature[57]. Several methods have been developed to increase the coherence time by decreasing nuclear spin diffusion processes. One of them is the dynamical nuclear decoupling, including Carr–Purcell–Meiboom–Gill (CPMG) pulse, XY pulse etc[58]. These dynamical decoupling methods can decrease the spin system–environment interaction and increase the coherence time. Generally, a train of pulses with the same interval of τ_d is applied to the spin system to refocus the evolution of the spin system-environment. If the interval between the dynamical decoupling pulses τ_d is shorter than the correlation time τ_e of the environment of the spin system, the coherence time can be effectively increased[59]. Federico et al. used the CPMG pulse sequence to achieve the dynamical nuclear decoupling in graphenoids and found that when the inter-pulse spacing equals the inverse of the Larmor frequency of the nucleus with the largest modulation, this method has the most significant impact[58,60]. The fact is that this method could make the coherence time approach the dephasing time. Figure 2.6 shows all the advanced pulses they have used in this project[60]. The first pulse in all of these dynamical decoupling pulses is a $\pi/2$ pulse with x phase, and all the following pulses after the first $\pi/2$ pulse are π pulses. CP pulse sequence only contains the π-pulses with an x-phase. CPMG pulse sequence contains π-pulses with a y-phase. The XY4 pulse sequence contains π-pulses with both the x and y phases. The XY8 pulse sequence also contains the π-pulses with both x and y phase, but it contains 8 π-pulses, with the previous 4 π-pulses and the following 4 π-pulses having inverse phase orders. XY16 pulse sequence contains the π-pulses with x, $-x$, y, $-y$ phases. The phase difference between the first $\pi/2$-pulse and the following π-pulse makes the CPMG pulse sequence more effective in dealing with pulse errors, compared with the CP pulse sequence[59].

Figure 2.7 shows the time traces of T_m of molecular graphenoids and the fitting lines at 100 K using five types of dynamical decoupling pulses. With increasing number of the π-pulses, the coherence time is increased significantly. When CPMG20 pulse sequence was used, the coherence time was even at the magnitude of order of 100 microseconds [60].

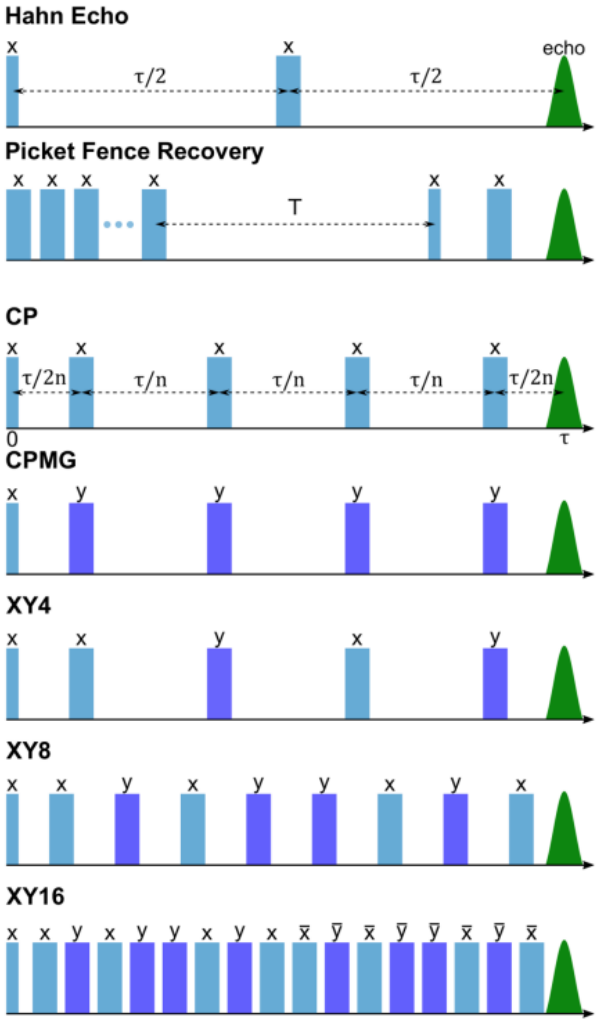

Figure 2.6 Advanced pulse sequences for dynamical decoupling, including Hahn echo, CP, CPMG, XY4, XY8, XY16, and a pulse sequence (Picket fence recovery) for measuring T_1 [60].

The other important decoherence channel in these research samples is molecular motion, such as the methyl group, which could be part of the matrix d8-toluene, and also

appears in the paramagnetic molecule [61,62]. For example, Jeschke et al. investigated methyl group tunnelling using EPR [63]. The rotation barrier and temperature determine the methyl group motion [64]. When thermo-energy is above the rotation barrier, classical reorientation happens. When the temperature is very low, quantum rotational tunnelling happens because of the overlap of the three localized wave functions. The overlap of the three localized wave functions lifts the three degenerate methyl group states into one ground state A, and two degenerate excited states E_a and E_b. The hyperfine couplings would further lift the degeneracy of these excited states [63]. They used three-pulse ESEEM to get the quantum tunnel frequency of the methyl group in Mn-methyl pairs, and found that when the temperature is lower than 30 K, the quantum tunnel frequency is kept constant, and if the temperature falls within the range of 30 K to 70 K, the quantum-tunnel frequency is decreasing as the temperature increases [63].

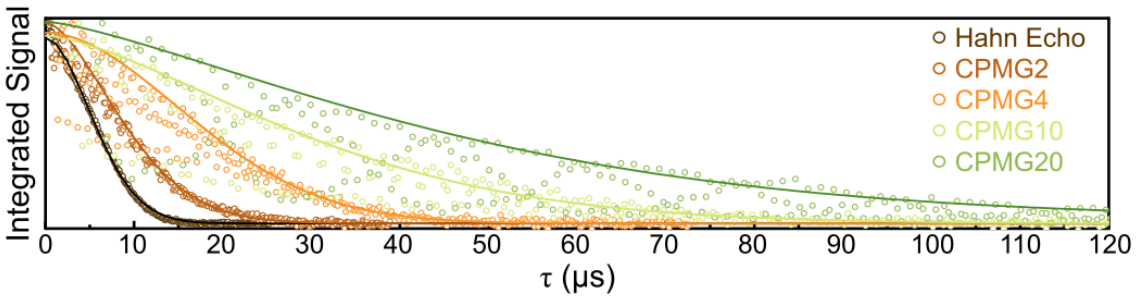

Figure 2.7 Time traces of T_m at 100 K by using different dynamical pulse sequences, including Hahn Echo, CPMG2, CPMG4, CPMG10, and CPMG20. As the number of π-pulses increases, the coherence time increases significantly. Figure adapted from Ref. [60].

2.3 Measurement of the spin–lattice-relaxation time

2.3.1 Inversion Recovery

Figure 2.8 shows the pulse sequence of inversion recovery and the corresponding illustration in the Bloch sphere. First, a π-pulse rotates the magnetisation from the up to the down direction. Then after a delay time of *t*, a π/2-pulse is used to rotate the magnetisation from *z*-direction to *xy*-plane. Afterwards, a refocusing π-pulse is used for detection. The delay time *t* is increased incrementally to obtain the time trace of spin–lattice relaxation.

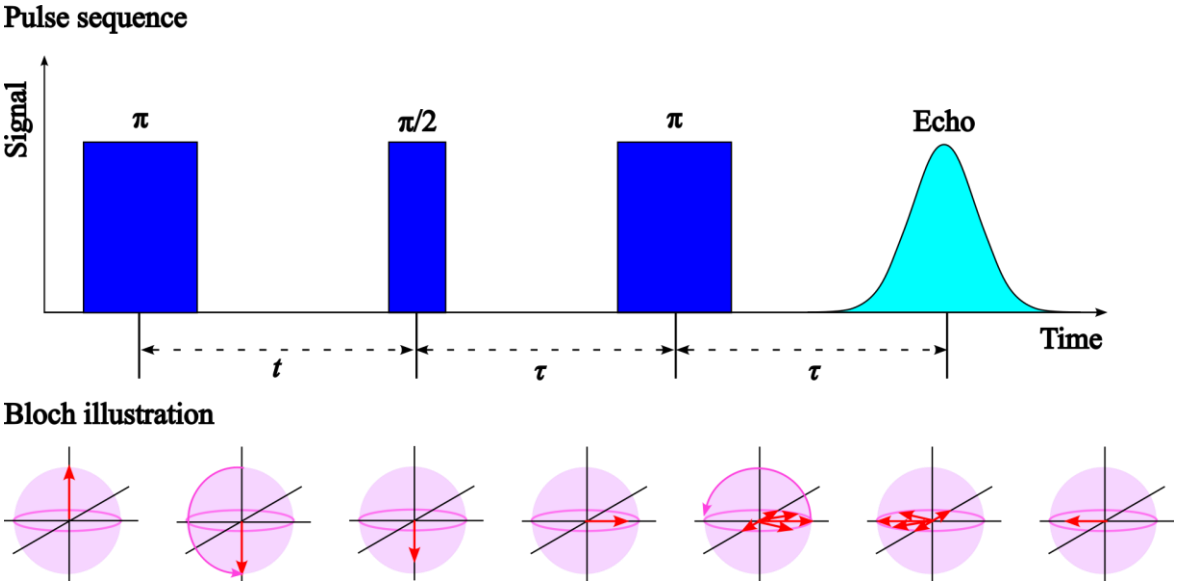

Figure 2.8 The pulse sequence of inversion recovery and its corresponding Bloch sphere illustration. The first π-pulse inverts a spin from spin-up state to spin-down state, the π/2-pulse rotates a spin from *z* direction into the *xy*-plane, and the second π-pulse inverts the spin's orientation in the *xy*-plane.

2.3.2 Picket-Fence pulse sequence

Figure 2.9 shows the Picket Fence pulse sequence and the corresponding Bloch sphere illustration. First, a series of π-pulses is used to demagnetise the spin system. The number of π-pulses in this work was set to 28. Then after a delay *t*, the spin system gradually returns to its original state. Afterwards, a Hahn-echo pulse sequence is used to rotate the magnetisation from the *z*-direction to the *xy*-plane and get the intensity of the refocusing echo. Here the delay *t* is increased incrementally to obtain the time trace of spin–lattice relaxation.

In the inversion recovery pulse sequence, since the first π-pulse could only excite a portion of the whole spins, during the delay *t*, the unexcited spins could transfer their magnetisation to the excited spins making the recovery rate faster. This process is called spectral diffusion[27]. The Picket Fence pulse sequence is less affected by spectral diffusion and therefore is more accurate in identifying T_1. After obtaining the time trace of spin–lattice relaxation, we used a double exponential equation to extract T_1. The equation is as follows:

$$y = A_1 e^{-\frac{t}{T_1}} + A_2 e^{-\frac{t}{T_{fd}}} + y_0, \tag{2.6}$$

where T_1 represents spin–lattice relaxations time and T_{fd} represents all fast decaying processes. The fast decaying contribution is typically much larger than the spin–lattice relaxation, so $A_1 >> A_2$. Therefore, we can extract the spin relaxation time by comparing the two rates.

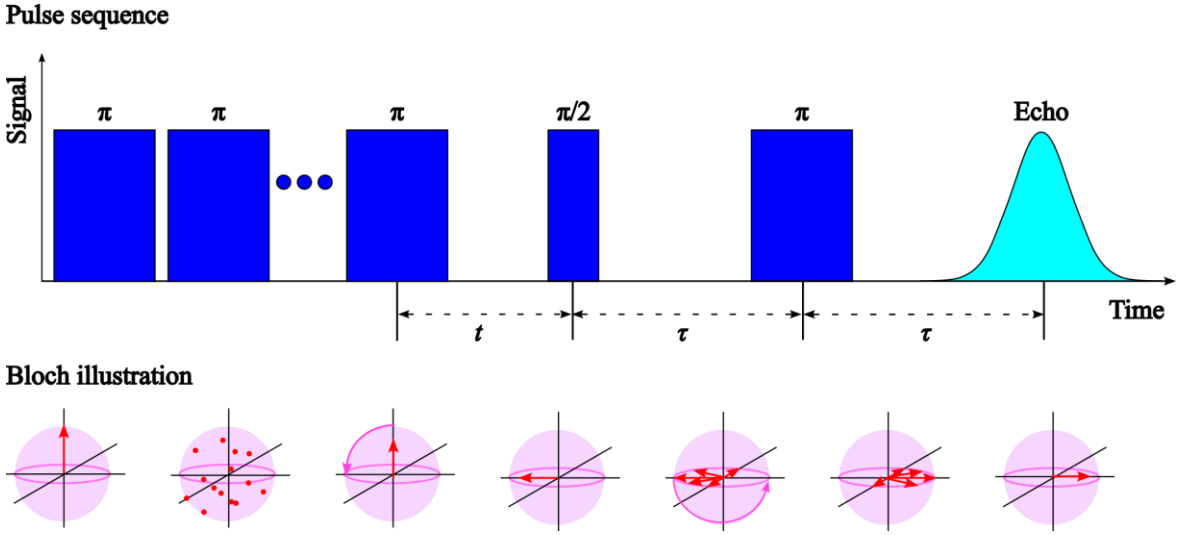

Figure 2.9 The pulse sequence of the Picket Fence and its corresponding illustration in the Bloch sphere. The original a series of π-pulses demagnetize the spin system, a π/2-pulse rotates a spin from *z* direction into *xy* plane, and a π-pulse inverts a spin's orientation in the *xy*-plane.

2.3.3 Spin–lattice relaxation mechanisms

The spin–lattice relaxation process involves the transfer of energy between the Zeeman energy of spin and the thermal energy of the lattice. Many relaxation processes involve the Debye model describing the phonon vibrational modes of the solids. The vibrational frequencies extend from 0 to a cutoff frequency, which is $v = k_B\theta_D/h$, where the k_B represents Boltzmann's constant, h represents the Plank constant, and the θ_D represents the Debye temperature.

Direct process

This process satisfies the demand that the Zeeman energy equals the lattice phonon energy, which is a one-phonon process. The rate of direct process about the temperature is as follows: [26]

$$\frac{1}{T_1} = \mathrm{A_{dir}} T, \tag{2.7}$$

where A_{dir} represents an experimentally determined parameter. Such a linear dependence on the temperature is a significant characteristic of the direct process. Furthermore, this process usually dominates in the low-temperature range.

Raman process

A virtual excited spin state is required to involve in this process, and the excitation energy is smaller than the Debye temperature. The Zeeman energy equals the two phonons' energy difference. This process can be mathematically described by using this equation [26]

$$\frac{1}{T_1} = \mathrm{A_{Ram}} \left(\frac{T}{\theta_{\mathrm{D}}}\right)^9 \int_0^{\frac{\theta_{\mathrm{D}}}{T}} x^8 \frac{\mathrm{e}^x}{(\mathrm{e}^x - 1)^2}\, \mathrm{d}x, \tag{2.8}$$

where A_{Ram} represents an experimentally determined parameter. When the temperature is well below the Debye temperature, this relaxation rate has a dependence on T^9. However, when the temperature is well above the Debye temperature, this relaxation rate has a T^2 dependence.

Orbach process

The Orbach process is similar to the Raman process since it also involves two phonons to complete the energy transfer. However, the difference is that it involves an actual excited spin state rather than a virtual one. This process is described by this equation [26]

$$\frac{1}{T_1} = \mathrm{A_{orb}} \frac{\Delta_{\mathrm{orb}}^3}{\mathrm{e}^{\Delta_{\mathrm{orb}}/k_{\mathrm{B}}T} - 1}, \tag{2.9}$$

where Δ_{orb} is the energy of the excited state, and $\mathrm{A_{orb}}$ is an experimentally determined parameter.

Local-mode process

The previous relaxation processes all involve long-range phonon modes. The local-mode process involves a vibrational frequency of a local molecular group. The local-mode relaxation rate has a dependence on temperature as follows: [26]

$$\frac{1}{T_1} = \mathrm{A_{loc}} \frac{e^{\Delta_{loc}/k_B T}}{(e^{\Delta_{loc}/k_B T}-1)^2}, \tag{2.10}$$

where Δ_{loc} represents the energy of the local mode, and A_{loc} represents an experimentally determined parameter.

In order to visualise these relaxation processes, Figure 2.10 shows the schematic illustration of these relaxation processes.

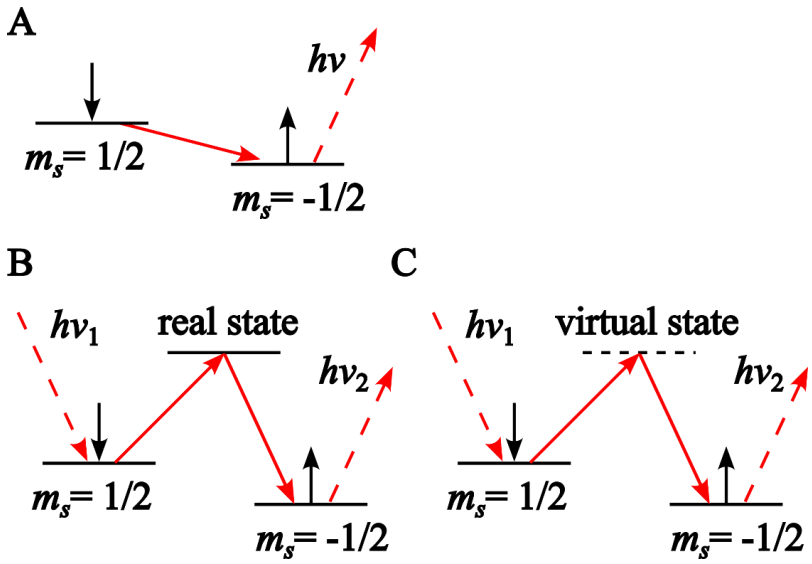

Figure 2.10 The schematic illustration of the spin–lattice-relaxation processes, including direct process (A), Orbach process (B), and Raman process (C).

2.4 Rabi oscillations

Rabi-oscillation experiments are used to manipulate the spin into any arbitrary state in the Bloch sphere. Furthermore, Rabi frequency, also known as the nutation frequency, can be used to identify the spin quantum number of a spin system. Figure 2.11 shows the pulse sequence of a Rabi oscillation experiment and its corresponding Bloch sphere illustration. First, a pulse with a length of T is applied to the spin system; then, after a delay time, a Hahn echo sequence is used for detection. The length of the first pulse is increased incrementally making the magnetisation rotate in the Bloch sphere. The delay after the first pulse is around $5T_{\mathrm{m}}$ of the spin system to eliminate the *xy*-component of the magnetization but keep the *z*-component. For a specific transition in a spin system, when the microwave can only excite a transition from m_s to m_s+1, the Rabi frequency is as follows:

$$\omega(m_s, m_s + 1) = \frac{g\mu_{\mathrm{B}}B_1}{\hbar}[S(S+1) - m_s(m_s+1)]^{1/2}, \tag{2.11}$$

where B_1 represents the intensity of the microwave and S the total spin quantum number. For example, for a spin system with spin quantum number $S = 1$, $\omega(-1,0) = \omega(0,-1) = \frac{\sqrt{2}g\mu_{\mathrm{B}}B_1}{\hbar}$, for a spin system with spin quantum number $S = 1/2$, $\omega(-1/2,1/2) = \frac{g\mu_{\mathrm{B}}B_1}{\hbar}$. So, the nutation frequency ratio between these two systems is $\sqrt{2}$. However, if the microwave irradiation is not selective, the bandwidth of the microwaves exceeds the difference of frequencies of these two transitions, which is zero-field splitting D. Both $|-1\rangle \rightarrow |0\rangle$ transition and $|0\rangle \rightarrow |1\rangle$ transitions are excited, making the nutation frequency become $\frac{g\mu_{\mathrm{B}}B_1}{\hbar}$, which is the same as the nutation frequency of spin-1/2 system.

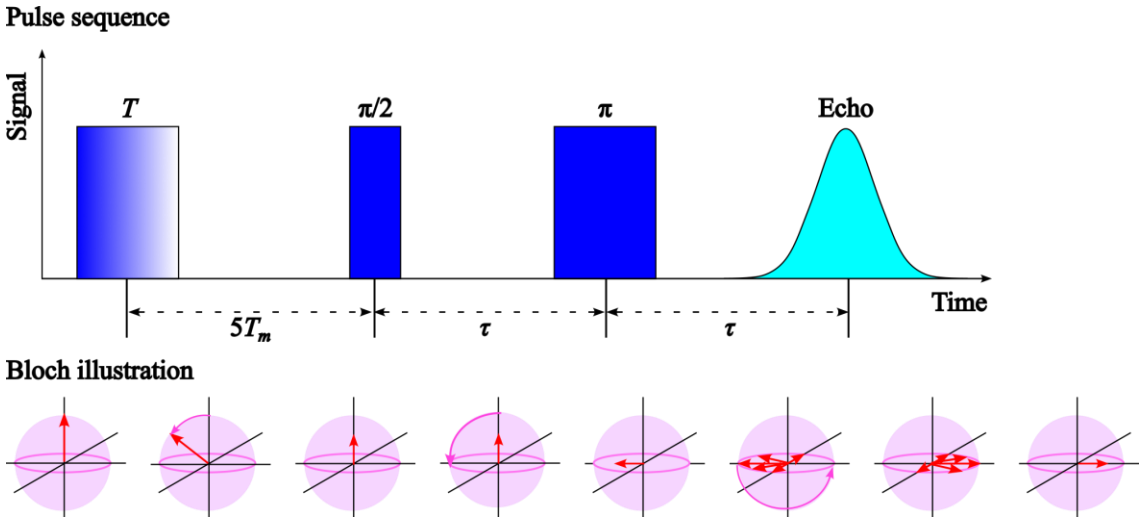

Figure 2.11 The pulse sequence of the Rabi oscillations experiment and its corresponding Bloch sphere illustration. The first variable pulse rotates a spin in the Bloch sphere, and the specific position relies on the length and power of the microwave. The *z*-component then is detected using a Hahn-echo pulse sequence.

2.5 ESEEM Spectroscopy

ESEEM spectroscopy is a type of hyperfine spectroscopy and is used to detect the hyperfine couplings in spin systems.

2.5.1 Two-pulse ESEEM

Figure 2.12 displays the two-pulse ESEEM pulse sequence is the same as the Hahn echo mentioned in the previous section. The first $\pi/2$-pulse electron creates electron coherence, including allowed and forbidden electron coherences. Then these electron coherences evolve during the following delay τ. Afterwards, a π-pulse mixes these electron coherences, and after another delay τ, the refocusing echo is measured. The time trace of the signal intensity can be modulated because of hyperfine couplings with coupled nuclei and also decays exponentially because of the decoherence properties of the electron spin.

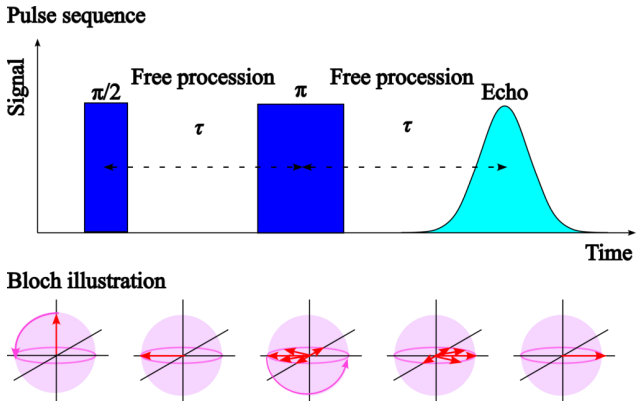

Figure 2.12 The pulse sequence of two-pulse ESEEM and its corresponding illustration in the Bloch sphere. The two-pulse ESEEM pulse sequence is the same as the Hahn echo.

In order to mathematically describe the two-pulse ESEEM effect, we first consider a simple case: an electron spin (S = 1/2) weakly coupled to a nuclear spin (I = 1/2). The weak coupling means that the hyperfine coupling is much smaller than the Larmor frequency of the nuclear. The spin Hamiltonian of this spin system is as follows:

$$\hat{H}_0 = \hat{H}_{EZ} + \hat{H}_{NZ} + \hat{H}_{HF} = \omega_S \hat{\boldsymbol{S}}_Z + \omega_I \hat{\boldsymbol{I}}_Z + A\hat{\boldsymbol{I}}_Z\hat{\boldsymbol{S}}_Z + B\hat{\boldsymbol{I}}_X\hat{\boldsymbol{S}}_Z, \tag{2.12}$$

where the electron spin is at the origin of the laboratory frame, and the nuclear spin is in the xz-plane, the ω_S and ω_I are the Zeeman frequencies of the electron and nuclear spins, respectively, the A is A_{zz} and B is the $\sqrt{A_{zx}^2 + A_{zy}^2}$. The A_{zx}, A_{zy}, and A_{zz} are the elements of the hyperfine-coupling matrix. After some induction, we can get the mathematical expression of the ESEEM modulation effect as follows: [26],

$$V_{2p}(\tau) = 1 - \frac{k}{4}[2 - 2\cos(\omega_{12}\tau) - 2\cos(\omega_{34}\tau) + \cos(\omega_-\tau) + \cos(\omega_+\tau)], \tag{2.13}$$

where k represents the modulation depth and equals $\sin^2(2\eta)$ and η is defined as:

$$\eta = \frac{\eta_\alpha - \eta_\beta}{2}, \tag{2.14}$$

where $\eta_{\alpha,\beta} = \tan^{-1}\left(-\frac{m_S B}{m_S A + \omega_I}\right)$.

ω_{12} and ω_{34} are the nuclear frequencies under the influence of hyperfine coupling of the electron spin, which are defined as follows: [26]

$$\omega_{12} = \left(\omega_I + \frac{A}{2}\right) cos\eta_\alpha - \frac{B}{2} cos\eta_\beta, \tag{2.15}$$

$$\omega_{34} = \left(\omega_I - \frac{A}{2}\right) cos\eta_\alpha + \frac{B}{2} cos\eta_\beta. \tag{2.16}$$

ω_+ and ω_- are the combination frequencies of the nuclear frequencies and their expressions are as follows,

$$\omega_\pm = \omega_{12} \pm \omega_{34}. \tag{2.17}$$

Equation 2.13 describing the modulation effect assumes that the pulses used in the pulse sequence are hard and the excitation bandwidth is larger than the absolute value of nuclear Larmor frequency ω_I and hyperfine-coupling constants, including *A* and *B*. However, if the excitation bandwidth $\Delta\omega$ is in such a range: $\min(\omega_{12},\omega_{34}) < \Delta\omega < \max(\omega_{12},\omega_{34})$, the modulation term only contains the smaller one of the two nuclear Larmor frequencies. If the excitation bandwidth $\Delta\omega$ is in such a range: $\Delta\omega < \min(\omega_{12},\omega_{34})$, the modulation term contains neither of these two nuclear Larmor frequencies.

When the electron spin is coupled with several different nuclear spins, which is more common in the practical condition, the refocusing echo intensity is modulated in such a way observing the product rule [26],

$$V_{2\mathrm{p,tot}}(\tau) = \prod_{i=1}^{N} V_{2\mathrm{p},i}(\tau), \tag{2.18}$$

where $V_{2\mathrm{p},i}(\tau)$ corresponds to the modulation of the different magnetic nuclear spins.

If we combine the modulation with the decoherence of the electron spin, the complete theoretical expression of the time trace of refocusing echo intensity is as follows: [26]

$$V'_{2p}(\tau) = e^{(-2\tau/T_m)} V_{2p}(\tau). \tag{2.19}$$

This equation means that the time trace of refocusing echo is an exponentially decaying data line combined with modulations from the coupled nuclear spins.

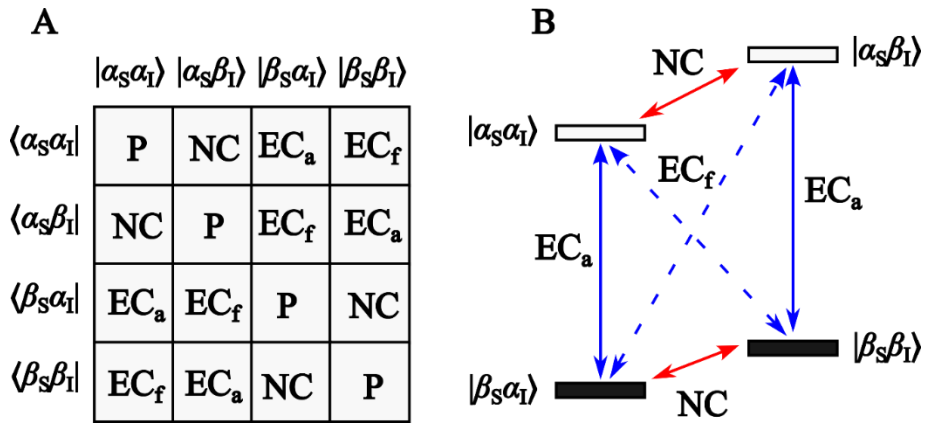

Figure 2.13 (A) Density matrix for an S = ½, I = ½ spin system. P represents polarization, NC represents nuclear coherence, EC_a represents allowed electron transitions, and EC_f represents forbidden electron transitions. (B) The corresponding energy-level diagram of this four-level system. The solid red lines represent nuclear coherence, the solid blue lines represent allowed electron coherence, and the dashed blue lines represent forbidden electron coherence.

The density matrix and energy-level diagram can be used to help understand the ESEEM effect. Figure 2.13 shows the density matrix and corresponding transitions for an S = ½, I = ½ coupled system. Initially, two lower energy levels are populated. The first π/2-pulse in two-pulse is non-selective, and both selective and non-selective electron coherences are excited. The π-pulse lead to a mixing of electron coherences.

2.5.2 Three-pulse ESEEM

The three-pulse ESEEM is a better technique to investigate hyperfine coupling than two-pulse ESEEM. As we can see in Figure 2.14, the first two π/2-pulses create nuclear coherences, and then these nuclear coherences evolve during the following delay, which is increased stepwise. Finally, another π/2-pulse is used to transform the nuclear coherences into electron coherence.

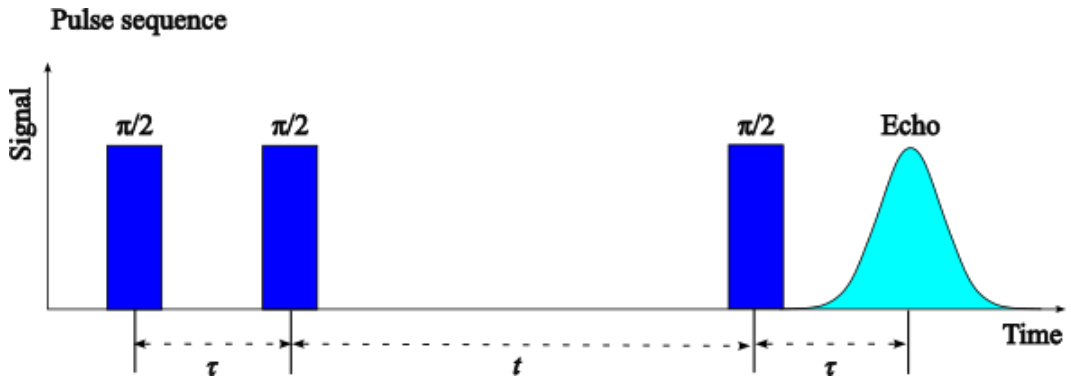

Figure 2.14 The pulse sequence of three-pulse ESEEM. The first π/2-pulse generates electron coherence, the second π/2-pulse converts electron coherence into nuclear coherence, and the final π/2-pulse converts nuclear coherence back into electron coherence.

The modulation decay is determined by the coherence time of nuclear spins ($T_{m,n}$). Since the coherence time of nuclear spins ($T_{m,n}$) is approximately at the order of spin–lattice relaxation time of electron spin (T_{1e}), which is usually much larger than the coherence time of electron spin (T_{2e}), the spectral linewidth of peaks in three-pulse ESEEM is much narrower than the spectral linewidth of two-pulse ESEEM. The mathematical description of the three-pulse ESEEM modulation for the same spin system containing electron spin S = 1/2 and nuclear spin S = 1/2 is as follows:[26]

$$V_{3p}(\tau,t)=\frac{1}{2}\left\{\left[1-\frac{k}{2}\left[1-\cos\left(\omega_\beta\tau\right)\right][1-\cos(\omega_\alpha(t+\tau))\right]+\left[1-\frac{k}{2}\left[1-\cos\left(\omega_\beta\tau\right)\right][1-\cos(\omega_\alpha(t+\tau))\right]\right\}=\frac{1}{2}\{V_{3p}^{\alpha}(\tau,t)+V_{3p}^{\beta}(\tau,t), \quad (2.20)$$

where $\omega_{\alpha,\beta}=|\omega_{12,34}|$, since the sign of the nuclear Larmor frequency in this expression does not influence the result.

For a spin system where electron spin is coupled with several magnetic nuclear spins, the total modulation effect is as follows: [26]

$$V_{3\mathrm{p}}(\tau,t)=\frac{1}{2}\left[\prod_{i=1}^{N}V_{3\mathrm{p}}^{\alpha}(\tau,t)+\prod_{i=1}^{N}V_{3\mathrm{p}}^{\beta}(\tau,t)\right]. \quad (2.21)$$

According to the equation, we could see fewer spectral peaks in the modulation spectrum since there are no combination frequencies ($\omega_{\pm}$). However, the disadvantage of the three-pulse ESEEM is that there could be a blind spot because of specific τ values satisfying this equation $\cos(\omega_{\alpha/\beta}\tau) = 1$. So, it is reasonable to take several different τ values to get different three-pulse ESEEM spectra.

2.6 HYSCORE Spectroscopy

Figure 2.15 shows the pulse sequence of HYSCORE [26]. Compared with the three-pulse ESEEM sequence, there is one additional π-pulse in the HYSCORE sequence.

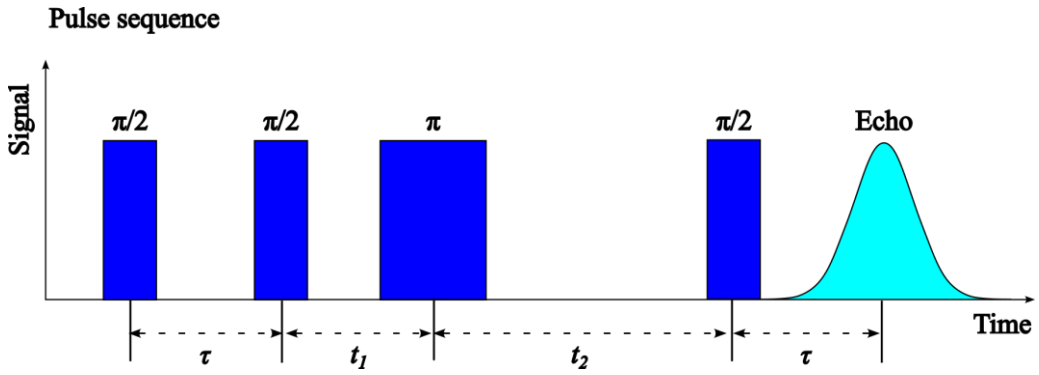

Figure 2.15 The pulse sequence of HYSCORE. The first π/2-pulse generates electron coherence, the second π/2-pulse converts electron coherence into nuclear coherence, the third π-pulse mixes different nuclear coherence, and the final π/2-pulse converts nuclear coherence back into electron coherence.

The first two π/2-pulses can create nuclear coherence. Then during the following delay t_1, the nuclear coherence evolves with a frequency ω_{12} or ω_{34}. However, the π-pulse completes the interchange of these two nuclear coherences, which means that the π-pulse

can make the nuclear coherence with a frequency ω_{12} transfer to the nuclear spin with a frequency ω_{34} and also make the nuclear coherence with a frequency ω_{12} transfer to the nuclear spin with a frequency ω_{34}.

Figure 2.16 displays a schematic diagram of HYSCORE spectrum corresponding to a spin system with $S = 1/2$ and $I = 1/2$. When the hyperfine coupling is much smaller than the hyperfine-free nuclear Larmor frequency ($|A| < 2\omega_I$), the peaks at the positions of (ω_{12},ω_{34}) and (ω_{34},ω_{12}) are shown in the first quadrant. When the hyperfine coupling is much larger than the hyperfine-free nuclear Larmor frequency ($|A| > 2\omega_I$), the peaks at the positions of ($-\omega_{12}$,ω_{34}) and (ω_{34},$-\omega_{12}$) are shown in the second quadrant. When the values of these two parameters are similar ($|A| \approx 2\omega_I$), the peaks are shown in both quadrants. The yellow peaks in the spectrum are the interesting peaks that correspond to the weak coupling, whereas the green peaks are interesting peaks relevant to the strong coupling. In these two types of cross peaks, the distance between the two peaks contains information on the hyperfine coupling. The blue peaks, called diagonal peaks, are because of the imperfection of the π-pulse in the HYSCORE pulse sequence. The π-pulse normally does not flip all the spins, so these nuclear coherences do not interchange after that π-pulse. Therefore, it is reasonable to reduce the length of the π-pulse and increase the excitation bandwidth. The red peaks, known as axial peaks, are trivial and should be disregarded.

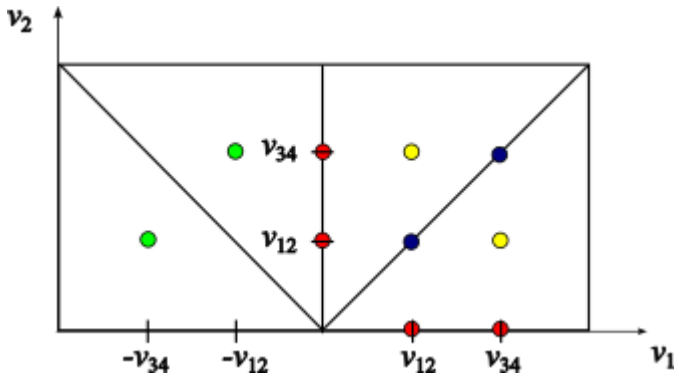

Figure 2.16 Schematic diagram of the HYSCORE spectrum corresponding to a spin system with $S = 1/2$ and $I = 1/2$. This spectrum is the Fourier transformation result of the time-trace signal. The horizontal axis ν_1 corresponds to the Fourier transformation result of t_1 and the vertical axis ν_2 corresponds to the Fourier transformation result of t_2. The nontrivial peaks are the cross peaks from which we could extract hyperfine couplings.

2.7 DFT calculations of EPR parameters

In this thesis, DFT calculations using ORCA software were done in order to help understanding the experimental results. A brief review of the Density Functional Theory is shown there [65,66]. This is the many-body Schrödinger equation without external fields:

$$\left[-\sum_i \frac{\hbar^2}{2m_e}\nabla_i^2 - \sum_I \frac{\hbar^2}{2M_I}\nabla_I^2 - \sum_{i,I} \frac{e^2}{4\pi\epsilon_0}\frac{Z_I}{|\boldsymbol{r}_i - \boldsymbol{R}_I|} + \frac{1}{2}\sum_{i\neq j} \frac{e^2}{4\pi\epsilon_0}\frac{1}{|\boldsymbol{r}_i - \boldsymbol{r}_j|} + \frac{1}{2}\sum_{I\neq J} \frac{e^2}{4\pi\epsilon_0}\frac{Z_I Z_J}{|\boldsymbol{R}_I - \boldsymbol{R}_J|}\right]\Psi = E_{\text{tot}}\Psi \quad (2.22)$$

where m_e is the mass of an electron, M_I is the mass of I-th nucleus, $\boldsymbol{r}_i$ is the coordinate of the i-th electron, $\boldsymbol{R}_I$ is the coordinate of the I-th nucleus and Z_I is the atomic number of the I-th nucleus. The first term is the kinetic energy of electrons. The second term is the kinetic energy of nuclei. The third term is the potential energy between an electron and a nucleus. The fourth term is the potential energy between electrons. The fifth term represents the potential energy between nuclei. There are N electrons and M nuclei in the system. $\Psi(\boldsymbol{r}_1, \boldsymbol{r}_2, \ldots, \boldsymbol{r}_N, \boldsymbol{R}_1, \boldsymbol{R}_2, \ldots, \boldsymbol{R}_N)$ is the many-body wavefunction, which depends on the ordinates of the electrons and nuclei. E_{tot} is the total energy of the ground state of this system. This

equation is too complex to get an analytical solution, so some approximations need to be induced to simplify this question.

First, the Born–Oppenheimer approximation is used to assume the nuclei are all frozen. Compared with electrons, the nuclei typically have a mass three orders of magnitude larger than electrons. Therefore, the kinetic energy of nuclei is approximated as 0, and the potential energy between nuclei is a constant so that the previous equation can be reduced to

$$\left[-\sum_i \frac{\hbar^2}{2m_e}\nabla_i^2 - \sum_{i,I}\frac{e^2}{4\pi\epsilon_0}\frac{Z_I}{|\boldsymbol{r}_i - \boldsymbol{R}_I|} + \frac{1}{2}\sum_{i\neq j}\frac{e^2}{4\pi\epsilon_0}\frac{1}{|\boldsymbol{r}_i - \boldsymbol{r}_j|}\right]\Psi = E_{\text{tot}}\Psi. \tag{2.23}$$

Second, the independent electron approximation is used to assume that the electrons are independent of each other. The many-body wavefunction can be reduced to $\Psi = \prod_i \varphi_i(\boldsymbol{r}_i)$, which transforms a 3*N*-dimensional equation to *N* three-dimensional equations. Therefore, the famous Kohn–Sham equation is expressed as:

$$-\sum_i \frac{\hbar^2}{2m_{\text{e}}}\nabla_i^2\varphi_i + (V_{\text{n}} + V_{\text{H}} + V_{\text{x}} + V_{\text{c}})\varphi_i = \varepsilon_i\varphi_i\,, \tag{2.24}$$

where the first term is the electron kinetic energy, the second term V_{n} is external nuclear potential, the third term V_{H} is the potential energy of each electron, also known as Hartree potential, V_{x} is the exchange potential because of the Pauli exclusion principle preventing two electrons occupying the same quantum state, V_{c} is the correlation energy resulting from electron-electron repulsion. Then, the electron density $n(r)$ is introduced to substitute the wavefunction. The definition of electron density $n(r)$ is as follows:

$$n(\boldsymbol{r}) = \sum_i |\varphi_i(\boldsymbol{r})|^2 \tag{2.25}$$

Therefore,

$$E[n] = \int \mathrm{d}\boldsymbol{r}\, n(\boldsymbol{r})\, V_{\text{n}}(\boldsymbol{r}) - \sum_i \int \mathrm{d}\boldsymbol{r}\, \varphi_i^*(\boldsymbol{r})\frac{\nabla^2}{2}\varphi_i(\boldsymbol{r}) + \frac{1}{2}\iint \mathrm{d}\boldsymbol{r}\mathrm{d}\boldsymbol{r}'\frac{n(\boldsymbol{r})n(\boldsymbol{r}')}{|\boldsymbol{r} - \boldsymbol{r}'|} + E_{\text{xc}}[n]. \tag{2.26}$$

The first term represents the external potential between the electrons and the nuclei, the second term is the kinetic energy of the electrons, the third term is the Hartree potential, the final term is the exchange and correlation energy between two electrons, which is an unknown functional of the electron density. The previous problem of solving the Coulomb interaction between electrons transforms into getting suitable functionals that could work in specific material systems. Much literature has reported functionals that could work properly in some instances. The practical calculation procedure is like that: first, the nuclear coordinates are specified, and the initial guess for electron density is put in to calculate V_H and V_{xc}. Then these two terms are used to get a new density by solving this equation. If the difference between the new and initial density is over a predefined threshold, the new density will be used to get another V_H and V_{xc}. This iteration will continue until the difference is below that predefined threshold.

Since the molecules in this thesis contain the open shell structure, we must consider the spin degree of freedom. In the spin-restricted treatment, electrons with opposite spins are restricted to the same spatial orbital, which could be applied to a close-shell structure. In contrast, the unpaired electrons with opposite spins occupy different spatial orbitals in the spin-unrestricted treatment.

The functional used in this thesis is B3LYP, which is a type of hybrid functional and works well in the system of organic radicals [67]. At the same time, the basis set could also influence the calculation results. The basis set is the known wavefunctions used to describe the unknown molecular orbitals φ. The localised-orbital basis set is used in our molecules. Gaussian-type orbitals (GTO) and Slater-type orbitals (STO) are the most commonly used basis sets. The GTOs are easier to calculate, although the STOs are more accurate. GTOs are used more in the DFT calculation software nowadays. The basis sets used in this thesis are EPR-II and ERP-III, which can perform well in calculating the EPR-relevant parameters

for organic radicals [68,69]. The *g* factor and hyperfine couplings can be obtained with good accuracy compared with experimental results, but the zero-field splitting and *J* coupling are less accurate [68]. One possible reason is that the geometry of the molecules used in this thesis is in the gas phase separately, but during the experiment, the molecules need to be solved in a solvent. The solvent would change the geometry of the molecule and therefore influence the calculation results.

3.Vanadyl Porphyrin dimers

3.1 Introduction

Transition-metal complexes have recently been investigated by many groups because of their interesting magnetic and quantum properties. Compared with other molecular systems, vanadium complexes have quite long coherence times, up to ~ 1 ms [70]. The relationship between molecules' coherence properties and structures has been investigated. For example, Atzori et al. investigated the influence of molecules' coordination environments on their coherence properties [71]. They found that oxovanadium(IV) in a square pyramidal coordination has a larger coherence time than vanadium(IV) in an octahedral coordination from 4 K to room temperature, because the former has a larger spin–lattice relaxation time than the latter, and an oxovanadium(IV) moiety has less restriction on coherence time [71].

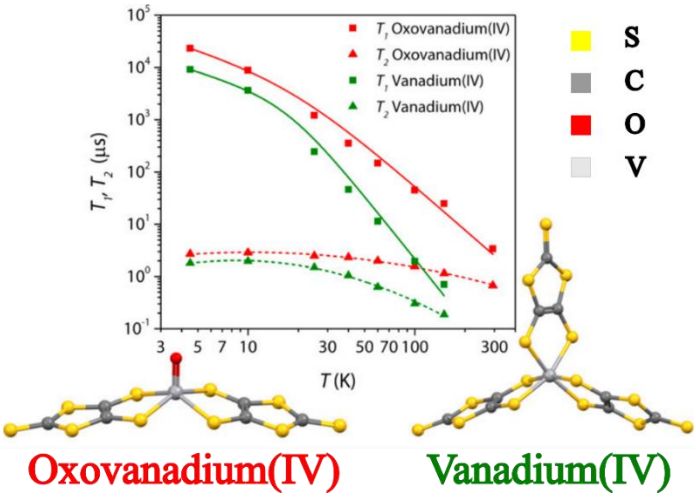

Figure 3.1 Chemical structures of Oxovanadium(IV) and Vanadium(IV) complexes, and their corresponding coherence time and spin–lattice-relaxation times, respectively. Both the spin–lattice- and spin–spin-relaxation times of Oxovanadium(IV) are larger than that of vanadium(IV). Figure adapted from Ref. [71].

Figure 3.1 shows the chemical structures of these two types of molecules and the coherence and spin–lattice-relaxation times. In their research, Atzori et al. demonstrated that molecules that have ligands with no nuclear spin have significantly longer coherence times. Oxovanadium(IV) can have a larger coherence time than its vanadium counterpart, which can be as high as 1.04 μs. Furthermore, they observed Rabi oscillations, demonstrating that vanadyl-based complexes are promising materials for quantum-gate operations. Such oscillations mean that basic gate operations (such as the NOT gate) are possible, which can be used to perform more complicated quantum-gate operations. Furthermore, Yu et al. investigated a family of vanadyl complexes and analogous VS_6 complexes that were resolved in different solvents of different polarities [72]. Their results showed that a stronger solute–solvent interaction led to a remarkable increase in T_1, because stronger solute–solvent interactions can rigidify the molecular structure and decrease molecular vibrations of low energy, thereby elongating the unpaired electron spin's coherence time [72].

They used the spin-diffusion-barrier models shown in Figure 3.2 to explain the coherence properties in this family of molecules [72]. Dipolar interactions between the unpaired electron spin and nearby nuclear spins (within a set radius of the electron spin) cause the resonance frequency of the nuclear spins to shift. This suggests that these nearby nuclear spins are not involved in nuclear-spin diffusion, and thus do not contribute to the electron spin's decoherence. For an electron spin in a protiated solution, the radius of the spin-diffusion barrier is around 3–10 Å [73]. In a deuterated solution, it is smaller because the magnetic moment of deuterons is smaller than protons'. Therefore, the radius of the spin-diffusion barrier in a deuterated environment decreases to meet the requirements imposed by the dipolar interactions between the electron and nuclei.

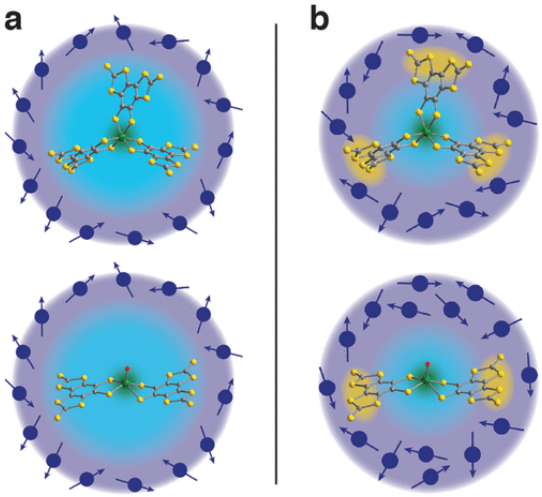

Figure 3.2 Spin diffusion barrier model for $(Ph_4P)_2[VO(C_8S_8)_2]$ and $(Ph_4P)_2[V(C_8S_8)_3]$ in (a) 1:1 Dimethylformamide: Toluene and (b) 1:1 Dimethylformamide-d7:Toluene-d8, respectively. The purple colour represents the region, where the nuclear spins contribute to the decoherence of the unpaired electron spin. The blue colour represents the spin-diffusion-barrier region, where the nuclear spins almost do not contribute to the decoherence. The yellow colour represents the region where the nuclear-spin-free ligands replacing the solvent molecules. The green colour represents the region where the unpaired electron distributes. Figure adapted from Ref. [72].

As shown in Figure 3.2, the blue region is the volume within the spin-diffusion barrier, the purple region shows nuclei contributing to the electron spin's decoherence, the green region indicates the electron-spin distribution, and the yellow region represents the ligands with no nuclear spins that replace the nuclei in the solvent that contributed to the electron spin's decoherence. Comparing the radii of the spin-diffusion barriers of these two molecules, 1:1 Dimethylformamide: Toluene and 1:1 Dimethylformamide-d7:Toluene-d8, we can see clearly that the former has a spin-diffusion barrier of larger radius because of the larger magnetic moment of the protons in the solvent. In the 1:1 DMF: Tol solvent, since the ligands of these two molecules are within the spin-diffusion barrier, the coherence

properties are similar. In the 1:1 Dimethylformamide-d7:Toluene-d8 solvent, however, the three $C_8S_8^{2-}$ ligands in $(Ph_4P)_2[V(C_8S_8)_3]$ lead to fewer deuteron ions of solvent close to the central electron spin. So, $(Ph_4P)_2[V(C_8S_8)_3]$ has a larger coherence time than $(Ph_4P)_2[VO(C_8S_8)_2]$.

Recently, the Sessoli group synthesised a *meso-meso* linked vanadyl porphyrin dimer to explore its potential for quantum information processing [21]. They found that the isotropic exchange coupling is at the order of magnitude of 0.01 cm^{-1} (300 MHz) [21]. The coherence time of meso–meso-linked vanadyl porphyrin dimer is similar to that of vanadyl porphyrin monomer [21]. DFT results show that the tilting angle between the two planes of vanadyl porphyrin has a large impact on the isotropic exchange coupling [21]. When the two planes are perpendicular to each other, the *J* coupling is at the minimum [21]. However, when the two planes are parallel, the *J* coupling is at the maximum [21].

Our project focused on vanadyl porphyrins, in which the magnetic centres are fixed and electrons can transfer within the π-backbone structure. This type of molecule can be used to investigate the influence of both exchange couplings and side groups on coherence properties. Furthermore, after figuring out how this system loses coherence, we can move on to performing quantum-gate operations, such as one-qubit gate operations containing X, Y, Z, and Hadamard, and two-qubit gates, including the CNOT and SWAP gates. The left graph in Figure 3.3 depicts the side and top views of the vanadyl porphyrin monomer structure. The vanadium atom is contained in the vanadyl ion (VO^{2+}), which is connected to four nitrogen atoms in the plane. Vanadium has an electron configuration of $[Ar]3d^1$, which means it is paramagnetic with a ½ spin. When the vanadyl ion is incorporated into the porphyrin, it creates a distorted square-planar geometry with the unpaired electron in the d_{xy} orbital. Figure 3.4 shows the electronic structure of the vanadyl porphyrin monomer. We performed DFT calculations using the quantum-chemistry software Orca, with the PBE0

functional [74], the CP(CPP) basis set used for the V atom, and the EPR-II basis set for other atoms [75]. Furthermore, we used a finer grid around the V atom to improve the accuracy of calculations. Four lobes of the unpaired electron's orbital point towards the four meso positions of the porphyrin, most of the electron-spin distribution is centred on the d_{xy} orbital of the vanadyl ion while not much is in the porphyrin plane. In copper(II) and silver(II) porphyrins, however, the unpaired electrons reside in the $d_{x^2-y^2}$ orbital and interact with the N atoms in the ligand through a σ bond [76,77].

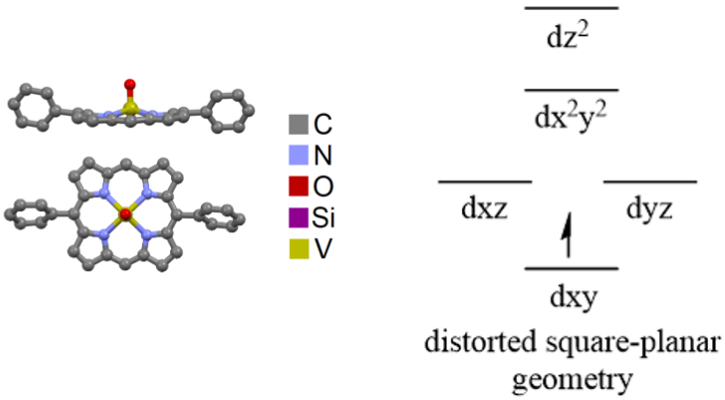

Figure 3.3 The left schematic shows the side view and top view of the chemical structure of the vanadyl–porphyrin monomer. The right schematic shows the electronic configuration of VO^{2+} ion. The unpaired electron resides in the d_{xy} orbital.

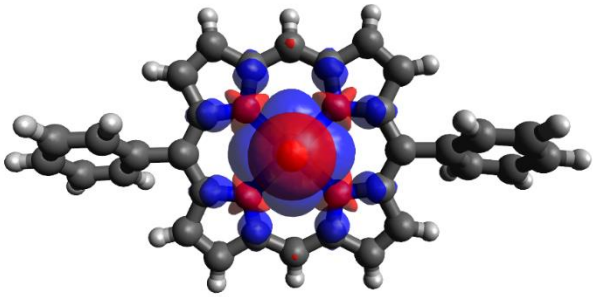

Figure 3.4 Electronic structure of vanadyl porphyrin monomer. The blue colour represents positive spin densities, and the red colour represents negative spin densities. The majority of unpaired electron-spin density resides on the vanadyl ion, and a little resides on the porphyrin ligand.

The chemical structures of the vanadyl porphyrin dimers are shown in Figure 3.5. The dimeric structures are butadiyne-linked, acetylene-linked, singly linked, *syn*-triply fused and *anti*-triply fused, respectively. The dihedral angle between the two porphyrin planes in the singly linked molecule is 84.24°. The four aryl groups in bl-dimers labelled with asterisks are attached with THS and tBu groups. All other dimers have the same side groups at the same position of their structures.

The different side groups were achieved through using different molecules at the first stage of the synthesis procedure. For example, if we use a free-base porphyrin monomer with THS side group at the first stage, we can get vanadyl porphyrin monomer with THS side groups. t-Bu side groups are useful for growing crystals for X-ray diffraction analysis, whereas flexible side chains, such as $-Si(C_6H_{13})_3$ in our case, confer higher solubility and prevent aggregation.

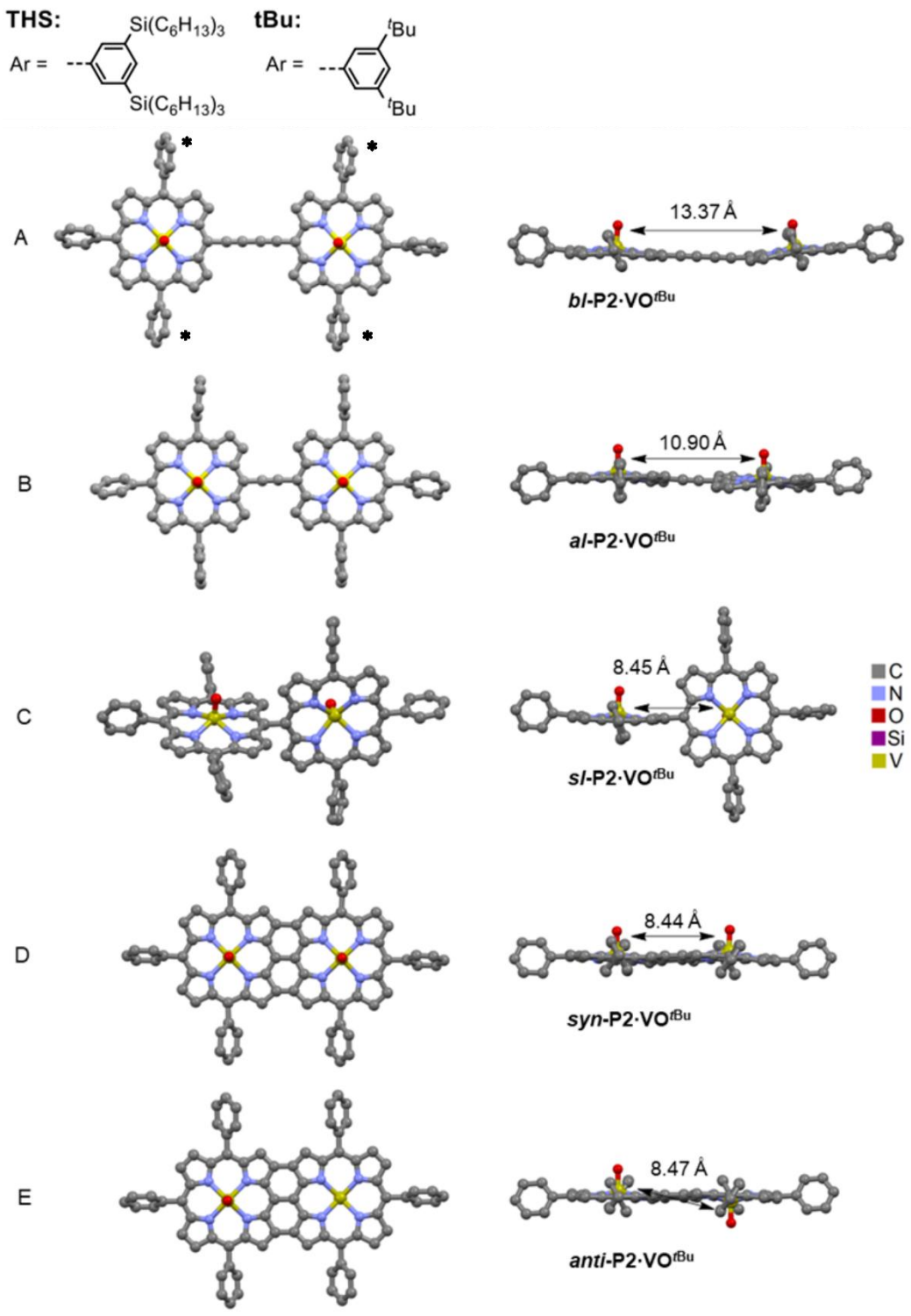

Figure 3.5 The structures of vanadyl porphyrins, including (A) butadiyne-linked vanadyl dimer, (B) acetylene-linked dimer, (C) singly linked dimer, (D) *syn*-triply fused, (E) *anti*-triply fused.

3.2 Magnetic properties

All samples were prepared as a 1 mM solution in d8-toluene. The side group has almost no influence on the CW spectrum. Hence, the same porphyrin molecule with either THS ($-Si(C_6H_{13})_3$) or tBu ($-C(CH_3)_3$) side group will have a similar CW-EPR spectrum, and thus only porphyrin molecules with THS ($-Si(C_6H_{13})_3$) side group were measured.

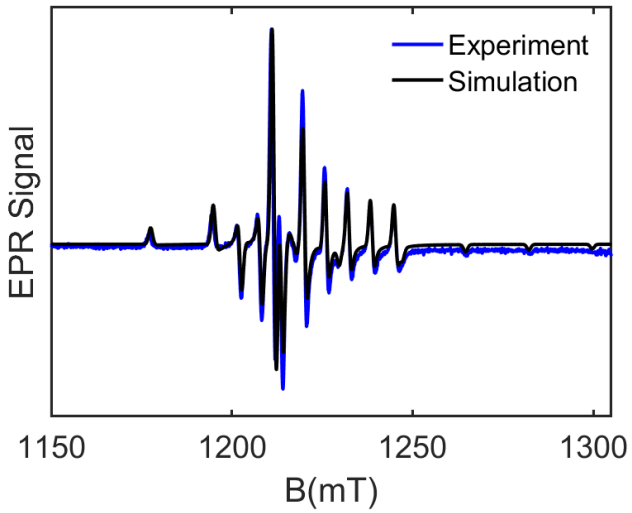

Figure 3.6 CW-EPR spectrum of vanadyl porphyrin monomer at Q-band. The blue line is the experiment result, the black line is the simulation result.

Table 3.1 EPR parameters by fitting the experimental CW-EPR spectrum of monomer.

parameters	**Simulation**
$\boldsymbol{g}_{\perp}$	1.9840(1)
$\boldsymbol{g}_{\parallel}$	1.9612(1)
$\boldsymbol{A}_{\perp}$ (MHz)	169.8(1)
$\boldsymbol{A}_{\parallel}$ (MHz)	477.1(1)
lw (mT)	1.06(3)

The CW-EPR spectrum of the vanadyl porphyrin monomer at Q-band frequency that is shown in Figure 3.6 reflects the interactions between the delocalised unpaired electron and the magnetic nuclei in the structure. Since the natural abundance of ^{51}V is 99.75%, it is safe to consider that all the V atoms here are ^{51}V. The spectrum displays the axial hyperfine coupling of the ^{51}V with I = 7/2. Because of the C_{4v} symmetry of the monomer's structure, we assume the g and hyperfine coupling tensors are collinear. In this case, the z-axis was chosen to point along the direction of the vanadyl structure, and the x and y axes span the porphyrin plane. The blue line is the experimental result, and the black line represents the simulation result. The spin Hamiltonian in this spin system is

$$\hat{H} = \mu_B B \boldsymbol{g} \hat{S} + \hat{S} \boldsymbol{A}^V \hat{I}^V. \quad (3.1)$$

As we can see from the results in Table 3.1, the g-factor shows little anisotropy. Both the parallel and perpendicular directions are defined relative to the applied magnetic field's direction. Furthermore, there is a small deviation from the g-factor of free electrons (2.0023), which means that the spin–orbit coupling is small.

From the spectrum, we can extract the hyperfine coupling of the vanadium nucleus, which is relatively large. Other magnetic nuclei, including nitrogen and hydrogen in the structure, have relatively small hyperfine couplings, smaller than the line width of the spectrum, and is therefore beyond the scope of CW-EPR, though it might be more clearly detected in more sophisticated techniques, such as HYSCORE or ENDOR. As we can see from the results in Table 3.1, the g-factor shows little anisotropy. Both the parallel and perpendicular directions are defined relative to the molecular axis. Furthermore, there is a small deviation from the g-factor of free electrons (2.0023), which means that the spin–orbit coupling is small. From the spectrum, we can extract the hyperfine coupling of the vanadium nucleus, which is relatively large. Figure 3.7 shows the spectra of the monomer obtained from both theory and experiment. The EPR-relevant parameters involved in these two

spectra are shown in Table 3.2. Theoretical results are consistent with the experimental results. The hyperfine couplings of H atoms in the monomer structure are all very small and all isotropic hyperfine couplings are smaller than 1 MHz. The isotropic hyperfine couplings of N atoms are between 8.1 to 8.5 MHz. They are not large enough to manifest in a CW spectrum.

For vanadyl porphyrins, the precision of energy is 1.0×10^{-9} au according to the input file settings. We used the functional B3LYP, and used CP(PPP) basis set for the V atom and EPR II for all other types of atoms. Such choices have been used to get good results, compared to experimental results, in calculating the EPR-relevant parameters in monomers previously [78].

Table 3.2 The comparison of the EPR-relevant parameters obtained from theory (DFT calculations) and experiment.

Parameters	**Experiment**	**Theory**
$\boldsymbol{g}_x$	1.9840(1)	1.9877
$\boldsymbol{g}_y$	1.9840(1)	1.9875
$\boldsymbol{g}_z$	1.9612(1)	1.9758
$\boldsymbol{A}_x$ (MHz)	169.8(1)	168.8
$\boldsymbol{A}_y$ (MHz)	169.8(1)	173.0
$\boldsymbol{A}_z$ (MHz)	477.1(1)	473.4

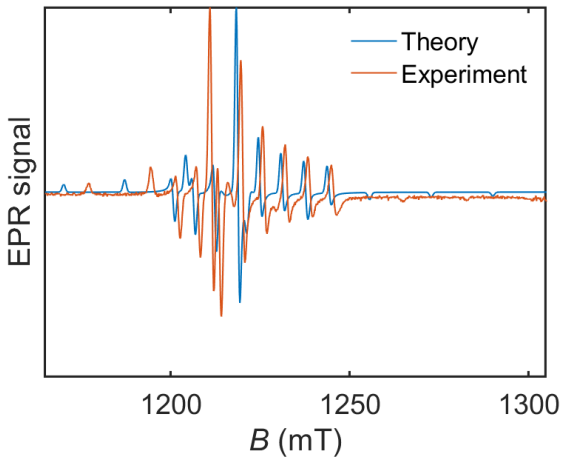

Figure 3.7 The comparison of the CW spectra of VO monomer from theory and experiment.

The dimeric structure has many parameters, which makes the spectrum complicated, and too many unknown parameters in the fitting process make fitting results unreliable because of overparameterization. We can, however, use the parameters we obtained from fitting the monomer structure to simplify the problem by fixing some parameters, such as the *g*-factor and hyperfine coupling of the vanadium nucleus. The *g*-factor is determined by both the orbital hosting the unpaired electron and the ligand field around this atom. Furthermore, in the case of two strongly coupled vanadyl moieties, the hyperfine coupling of the vanadium would become half that of the monomer; in the case of two weakly coupled vanadyl moieties, it would remain unchanged.

In the case of triply linked dimers, the exchange coupling is very strong: these systems with two unpaired electrons can be best described by ‘strong exchange’ [79]. The energy levels are split into two states, a singlet and a triplet. The singlet state is EPR-silent; the triplet state, however, is not and can be described by a quantum spin $S = 1$. These two states are separated by an energy gap J. The dipolar coupling in this strongly coupled

representation is described by a zero-field-splitting (ZFS) term *D*. Thus, the spin Hamiltonian in the triply linked spin system is

$$\hat{H} = \mu_B B \boldsymbol{g} \hat{S} + \sum_{i=1}^{2} \hat{S} \boldsymbol{A} \hat{I}^i + \hat{S} \boldsymbol{D} \hat{S}. \tag{3.2}$$

Unfortunately, the only thing we know about the dominant (tensor) terms in the spin Hamiltonian are their principle (eigen-) values. We need to determine the tensor frames and rotate them into the molecular frame to get the full tensor representation in one frame and perform the fits. Figure 3.8 shows the tensor frames for all the relevant tensors in this case, including Frame 1 for the ***g*** and ***A*** tensors of the first porphyrin plane, Frame 2 for the ***g*** and ***A*** tensors of the second porphyrin plane, and Frame D for the zero-field-splitting tensor.

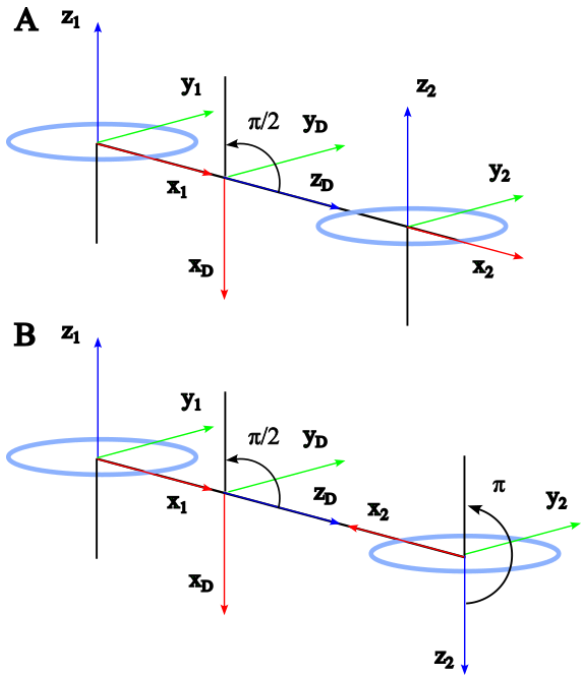

Figure 3.8 Schematic illustration of the *syn*-(A) and *anti*-(B) linked porphyrin dimers and the relative orientations of the different tensors. The subscripts 1, 2 and D represents the *g* tensors of the porphyrin units 1 and 2, and the dipolar or zero-field-splitting tensor, respectively. The blue rings represent the vanadyl porphyrin planes. The red, green, and blue axes stand for the *x*-axes, *y*-axes, and *z*-axes of these three tensors, respectively.

Here, Frame 1 was specified to be the same as the molecular frame, meaning that the rotation tensor for the $\boldsymbol{g}_1$ and $\boldsymbol{A}_1$ is $\boldsymbol{R}_1(0, 0, 0)$ using the *z*-*y*-*z* convention. The rotation matrix for the $\boldsymbol{g}_2$ and $\boldsymbol{A}_2$ is $\boldsymbol{R}_2(0, 0, 0)$ for the *syn*-dimer and $\boldsymbol{R}_2(0, -\pi, 0)$ for the *anti*-dimer. Since the zero-field splitting is induced by dipolar coupling here, it is safe to define the unique axis (z_D) along the triple-bond direction, giving the rotation matrix for $\boldsymbol{D}$, $\boldsymbol{R}_D(0, -\pi/2, 0)$. Therefore, the $\boldsymbol{g}_2$, $\boldsymbol{A}_2$, and $\boldsymbol{D}$ tensors in the molecular frame can be obtained by these rotation operations. Although Frame 2 is different for *syn*- and *anti*-dimer, $\boldsymbol{g}_2$ and $\boldsymbol{A}_2$ tensors in the molecular frame are the same for these two molecules after the rotation operations. Thus, as depicted in the spectra of these two dimers in Figure 3.10, *syn*- and *anti*- almost have identical spectra. The equations used to rotate the *g* tensor of porphyrin unit 2, the hyperfine coupling tensor of the V nuclear spin in porphyrin unit 2, and the zero-field-splitting tensor, from their respective tensor frames to the molecular frame are

$$\boldsymbol{g_M} = \boldsymbol{R_2 g_T R_2^T}, \tag{3.3}$$

$$\boldsymbol{A_M^V} = \boldsymbol{R_2 A_T^V R_2^T}, \tag{3.4}$$

$$\boldsymbol{D_M} = \boldsymbol{R_D D_T R_D^T}. \tag{3.5}$$

As we can see from the fits, in the triplet state, the hyperfine coupling of the triply linked dimer is half that of the monomer one. The exchange coupling *J* (809 MHz for *syn*-dimer and 899 MHz for *anti*-dimer) is much larger than the hyperfine coupling (477 MHz) and electron Zeeman anisotropy ($\Delta g \mu_B B$ = 420 MHz). Therefore, singlet–triplet mixing can be neglected, and a strongly coupled representation here is appropriate [77]. The spin Hamiltonian in the other weakly coupled dimeric spin systems is

$$\hat{H} = \mu_B \sum_{i=1}^{2} B \boldsymbol{g}^i \hat{S}^i + \sum_{i=1}^{2} \hat{S}^i \boldsymbol{A}^i \hat{I}^i + \hat{S}^1 \boldsymbol{J} \hat{S}^2, \tag{3.6}$$

where

$$\boldsymbol{J} = J + \boldsymbol{d} + \boldsymbol{D} = \begin{bmatrix} J & 0 & 0 \\ 0 & J & 0 \\ 0 & 0 & J \end{bmatrix} + \begin{bmatrix} 0 & d_z & -d_y \\ -d_z & 0 & d_x \\ d_y & -d_x & 0 \end{bmatrix} + \begin{bmatrix} D_{xx} & D_{xy} & D_{xz} \\ D_{yx} & D_{yy} & D_{yz} \\ D_{zx} & D_{zy} & D_{zz} \end{bmatrix} =$$

$$\begin{bmatrix} j_{11} & 0 & 0 \\ 0 & j_{22} & 0 \\ 0 & 0 & j_{33} \end{bmatrix} = \begin{bmatrix} J + D_{xx} & 0 & 0 \\ 0 & J + D_{yy} & 0 \\ 0 & 0 & J + D_{zz} \end{bmatrix}, \quad (3.7)$$

where $\boldsymbol{J}$ is the electron–electron interaction, J is the isotropic exchange coupling, $\boldsymbol{d}$ is the antisymmetric exchange coupling, and $\boldsymbol{D}$ is the traceless matrix containing dipolar and anisotropic exchange coupling.

Table 3.3 EPR parameters by fitting the experimental CW-EPR spectra of triply linked vanadyl porphyrins compared with monomers. *g*: *g*-factor; *A*: hyperfine coupling of vanadium; *J*: exchange coupling; *D*: zero-field splitting. If the zero-field splitting comes only from the dipole–dipole coupling, it is given by: $D = \frac{-3}{2}\frac{\mu_0 \cdot g_1 g_2 \mu_B^2}{4 \cdot \pi \cdot h \cdot r^3}$ [80]. Theoretical result: According to XRD results, r = 0.847 nm, so D = –128 MHz. Also, in such a case, where the dipolar coupling induces the zero-field splitting, the other zero-field-splitting parameter E = 0; lw: line width; (a) The *J* couplings in the *syn*- and *anti*-dimer structure were not obtained from the CW spectra fitting results but from the SQUID results.

Parameters	**monomer**	***Syn***	***Anti***
S	1/2	1	1
$g_\perp$	1.9840(1)	1.9871(2)	1.9874(2)
$g_\parallel$	1.9612(1)	1.9629(5)	1.9634(3)
$A_\perp$ (MHz)	169.8(1)	93.4(1)	85.3(1)
$A_\parallel$ (MHz)	477(1)	257.1(1)	261.6(1)
J (MHz)	–	809(30)[(a)]	899(60)[(a)]
D (MHz)	–	182(3)	186(6)
lw (mT)	1.06(3)	1.06	1.06

In the fitting process, we first fitted monomer's spectrum to obtain the *g* factor, hyperfine coupling and linewidth. Then we specified triply linked dimers to have the same *g* factor and linewidth as those of the monomer, because these spin Hamiltonian parameters do not change a lot. Since our triply linked dimers are in the strongly coupled regime, we can set the half of monomer's hyperfine couplings as good starting points to perform the fitting. Then the *J* coupling does not influence the spectra, since the singlet-triplet transition is negligible. Hence we do not need to define *J* coupling here. The zero-field-splitting here mainly comes from dipolar coupling between electrons, we can use the theoretical equation ($D = \frac{-3}{2}\frac{\mu_0 \cdot g_1 g_2 \mu_B^2}{4 \cdot \pi \cdot \mathrm{h} \cdot r^3}$) to get a good starting point. After getting all these variable parameters, we set a reasonable range for the *g* factor to further improve the simulation result. The inconsistency between the fitting and experimental results could come from several factors. One is the rhombic *g*-factor, since according to the chemical structure of triply linked dimers, g_x could have a little deviation from g_y. The other possibility could be due to the incomplete substitution process in the synthesis procedure, so there are some monomer impurities remaining in the dimer samples.

Since the *g* tensors of the two electron spins are either already aligned (*al*-linked and *bl*-linked dimers) or can be rotated by a certain angle to make them aligned (*sl*-linked dimer), the off-diagonal elements of the ***D*** matrix are zero. The dimension of the density matrix is $2^2(2I_1+1)(2I_2+1) = 256$, where I_1 and I_2 are the nuclear-spin quantum numbers of two ^{51}V nuclei in the dimers. Such a large density matrix means the fitting process can be time-consuming and complex. In order to simplify the question, we first assume the hyperfine couplings between S_1 and I_2 as well as between S_2 and I_1 are zero, since the distances between electron 1 and ^{51}V nucleus 2 and between electron 2 and ^{51}V nucleus 1 are very large. Furthermore, we assume the antisymmetric exchange coupling to be negligible, because of the small orbital contribution of vanadyl ions, which has been reported in other similar two-

qubit molecular systems [6,21]. Therefore, the electron–electron interaction can be reduced to four equations, with only three unknown parameters, j_{11}, j_{22}, and j_{33}. We can then obtain J and D_{xx}, D_{yy}, D_{zz} easily by using the equations, $J = (j_{11}+j_{22}+j_{33})/3$, $D_{xx} = j_{11}–(j_{11}+j_{22}+j_{33})/3$, $D_{yy} = j_{22}–(j_{11}+j_{22}+j_{33})/3$, $D_{zz} = j_{33}–(j_{11}+j_{22}+j_{33})/3$. All the tensors here are in their principal-axis frames, namely their tensor frames. We need to coordinate them to the same frame to fit the spectra correctly. The first thing is to specify the frames for these different tensors involved in the spin Hamiltonian.

In the singly linked dimer, the orientations of all the tensors are similarly out of alignment, as shown in Figure 3.9 (A). The rotation matrix for $\boldsymbol{g}_2$ and $\boldsymbol{A}_2$ is $\boldsymbol{R}_2(0, –\theta, 0)$, and the rotation matrix for $\boldsymbol{d}$ is $\boldsymbol{R}_d(0, –\pi/2, 0)$. The definition of the coordinate frame is not unique. For example, Figure 3.9 (B) shows another one. In this definition, the rotation matrix for $\boldsymbol{g}_2$ and $\boldsymbol{A}_2$ is $\boldsymbol{R}_2(0, –\theta, 0)$, and the rotation matrix for $\boldsymbol{d}$ is $\boldsymbol{R}_d(–\pi/2, –\pi/2, \pi/2)$. After rotation operations of these tensors, however, the full representation of all the tensors in the molecular frame is the same. In other words, the definitions of coordinate frames do not influence the final spin Hamiltonians and, therefore, the final fits.

When the exchange coupling J is much larger than other off-diagonal terms in the matrix of spin Hamiltonian, like hyperfine coupling, electron Zeeman anisotropy and zero-field-splitting, then it is better to use strong coupling to describe the spin system. If one of these terms is comparable or larger than exchange coupling J, the system is within the weak coupling regime.

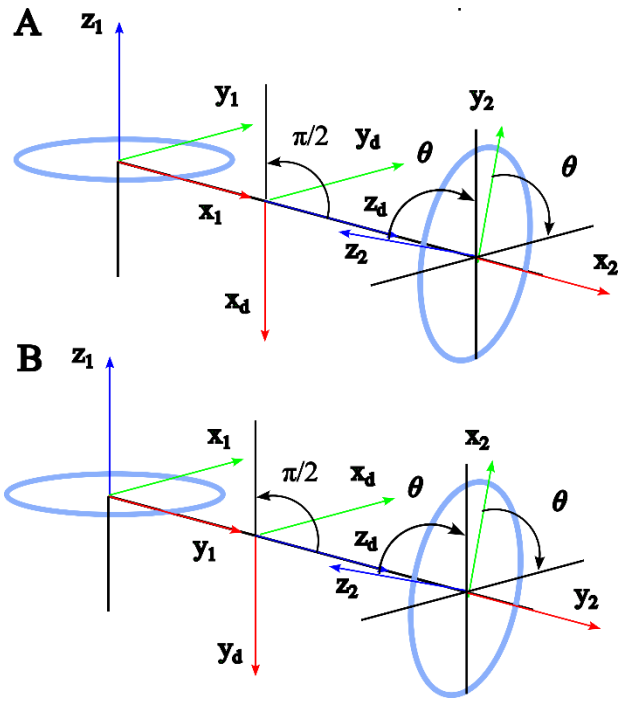

Figure 3.9 (A) Schematic illustration of the singly-linked porphyrin dimer and the relative orientations of the different tensors. (B) An alternative schematic illustration of the singly-linked porphyrin dimer and the relative orientations of the different tensors. The blue rings represent the vanadyl porphyrin planes. There is a twisting angle between the two planes.

Table 3.4 EPR parameters by fitting all the experimental CW-EPR spectra of *sl*-linked, *al*-linked, and *bl*-linked vanadyl porphyrins. $R_{v\text{-}v}$: the distance between two vanadium nuclei; *J*: the isotropic exchange coupling; D_{xx}, D_{yy}, D_{zz}: the combination of dipolar and anisotropic exchange couplings along the *x*, *y*, *z* directions; lw: the line width of the spectrum.

linker	$R_{v\text{-}v}$(nm)	*J*(MHz)	D_{xx}(MHz)	D_{yy}(MHz)	D_{zz}(MHz)	lw(mT)
singly-linked	0.845	269(5)	-86(5)	-102(5)	189(5)	1.06
acetylene-linked	1.09	14.67(1)	-13.07(1)	-13.07(1)	26.14(2)	2.8(1)
butadiyne-linked	1.337	10.74(4)	-9.97(1)	-9.97(1)	19.94(2)	1.06

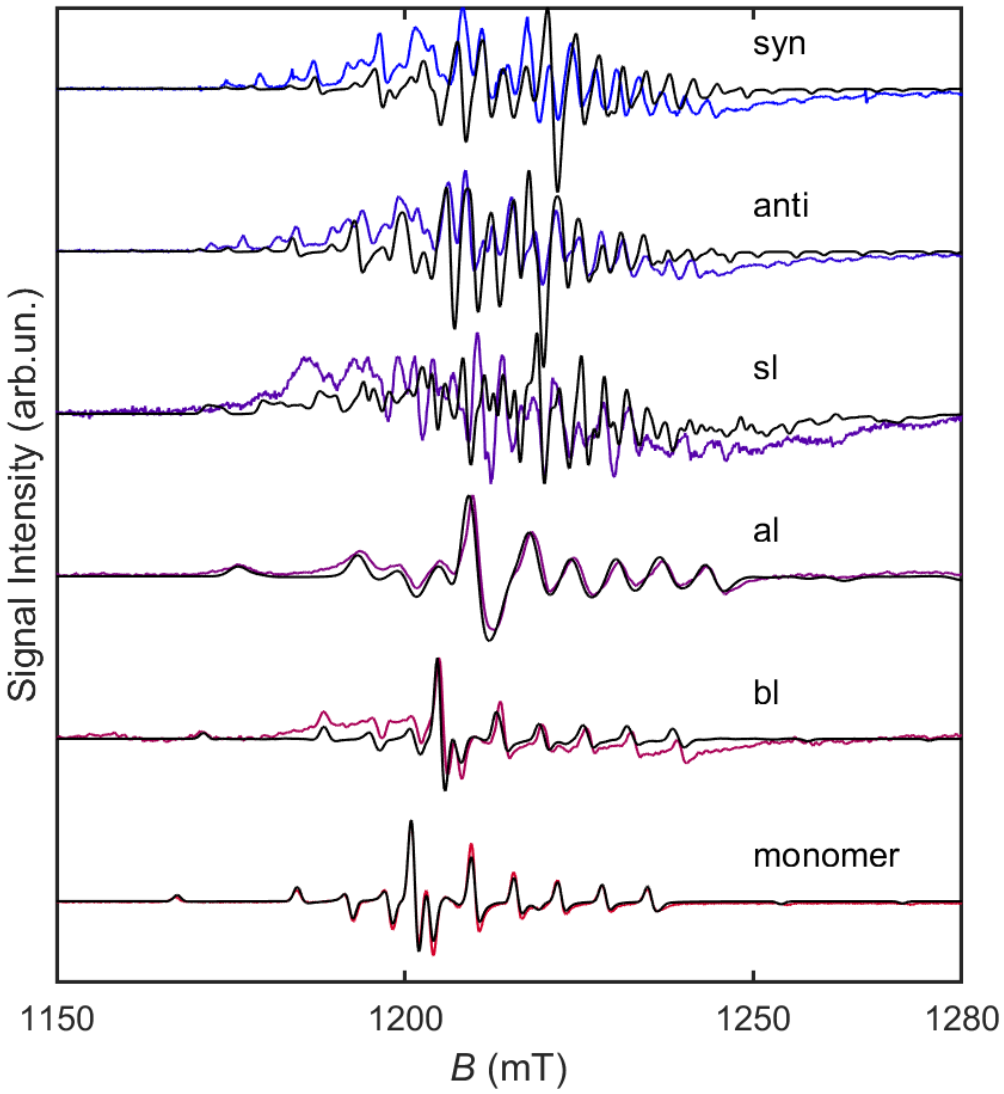

Figure 3.10 Q-band CW-EPR spectra and corresponding fitting results of all vanadyl porphyrins at 140 K. The materials are dissolved in d8-toluene at a concentration of 1 mM and are in a frozen solution state. All the fitting parameters are listed in main text.

From the fits, we can draw some conclusions. One is that the triply linked dimers, including the *syn*- and *anti*-dimers, are strongly coupled and are best described by an $S = 1$ spin system. The exchange couplings are 809 MHz and 899 MHz for *syn*- and *anti*-dimer, respectively. The positive value means that the triply linked dimers are antiferromagnetic.

On the other hand, in other weakly coupled dimers, including *sl*-linked, *al*-linked, and *bl*-linked dimers, it is better to define the spin system in this way: $s_1 = s_2 = 1/2$.

Moreover, the exchange coupling decreases exponentially as the distance between unpaired electron spins increases. This result is consistent with the fact that some electron spin densities reside in the vanadyl ion, and some electron spin densities extend into the linker. As the distance increases, the overlap of the spin densities decreases significantly. The *anti*- and *syn*-dimers have similar isotropic exchange coupling because the orientations of the two vanadyl ions within dimeric structures almost do not influence the overlap of two electron spin densities. The dipolar coupling decreases more slowly than the isotropic exchange coupling because the dipolar coupling strength is inversely proportional to the third power of the distance between electron spins. Another interesting point is the linewidth of the spectra. From isotropic exchange coupling strength decreases, the linewidth of the spectrum first increases and then decreases. When the electron–electron interactions are below a certain value, they are absorbed into the linewidth. In the triply linked dimeric structures, the *g*-factor deviates from the monomer's *g*-factor, which means that the ligand field felt by the unpaired electron in a monomer is different from one in triply linked dimers. In the monomer, the unpaired electron only feels the ligand field of one porphyrin plane, but in the triply linked dimers, each unpaired electron can feel the ligand field of not only the porphyrin plane where it resides but also the other, neighbouring porphyrin plane. In the other weakly coupled dimers, however, the *g*-factor remains stable compared with the monomer, because each unpaired electron does not respond to the other porphyrin plane's ligand field in these weakly coupled dimers. We also performed these DFT calculations using Orca, with the functional and basis set chosen according to the previous literature on similar magnetic molecules [78,81]. X-ray crystal data for these compounds were used for the calculations. Figure 3.11 depicts the spin-density distributions of four types of dimers.

Unlike the copper porphyrins, in which the magnetic orbital has a σ-interaction with the ligand [77], the magnetic orbital of vanadyl porphyrins has a π-interaction with the ligand. Here, in our case, the twisting angle of molecules other than tripled linked ones could have a distribution due to the structures, and therefore could lead to a distribution of *J* couplings. It has been shown in Ref. [21] that twisting angles have an influence on the *J* coupling.

Furthermore, Table 3.5 shows the values of *J* from calculations. The equation used to calculate the isotropic exchange coupling was [82]

$$J = \frac{E_{\mathrm{HS}} - E_{\mathrm{LS}}}{\langle \widehat{S^2} \rangle_{\mathrm{HS}} - \langle \widehat{S^2} \rangle_{\mathrm{LS}}}, \tag{3.8}$$

where HS and LS denote the high-spin and low-spin states, respectively. As the distance between the two electrons increases, the *J* coupling decreases, which is consistent with the experimental results. The results from calculations are larger than the experimental results for these molecules.

Table 3.5 Energy, expectation values of S^2 and singlet–triplet energy calculated for *anti*-, *sl*-, *al*-, and *bl*-linked dimers.

Linker	*E* (Hartree)	$\langle S^2 \rangle$	*E* (Hartree)	$\langle S^2 \rangle$	$\Delta E_{\mathrm{S\text{-}T}}$ (MHz)
***anti*-linked**	-5415.695267218	1.020287	-5415.695266959	2.020260	1707
***sl*-linked**	-5417.854599305	1.020311	-5417.854599215	2.020310	594
***al*-linked**	-5494.112302557	1.021812	-5494.112302498	2.021807	392
***bl*-linked**	-5570.377911475	1.023723	-5570.377911416	2.023718	384

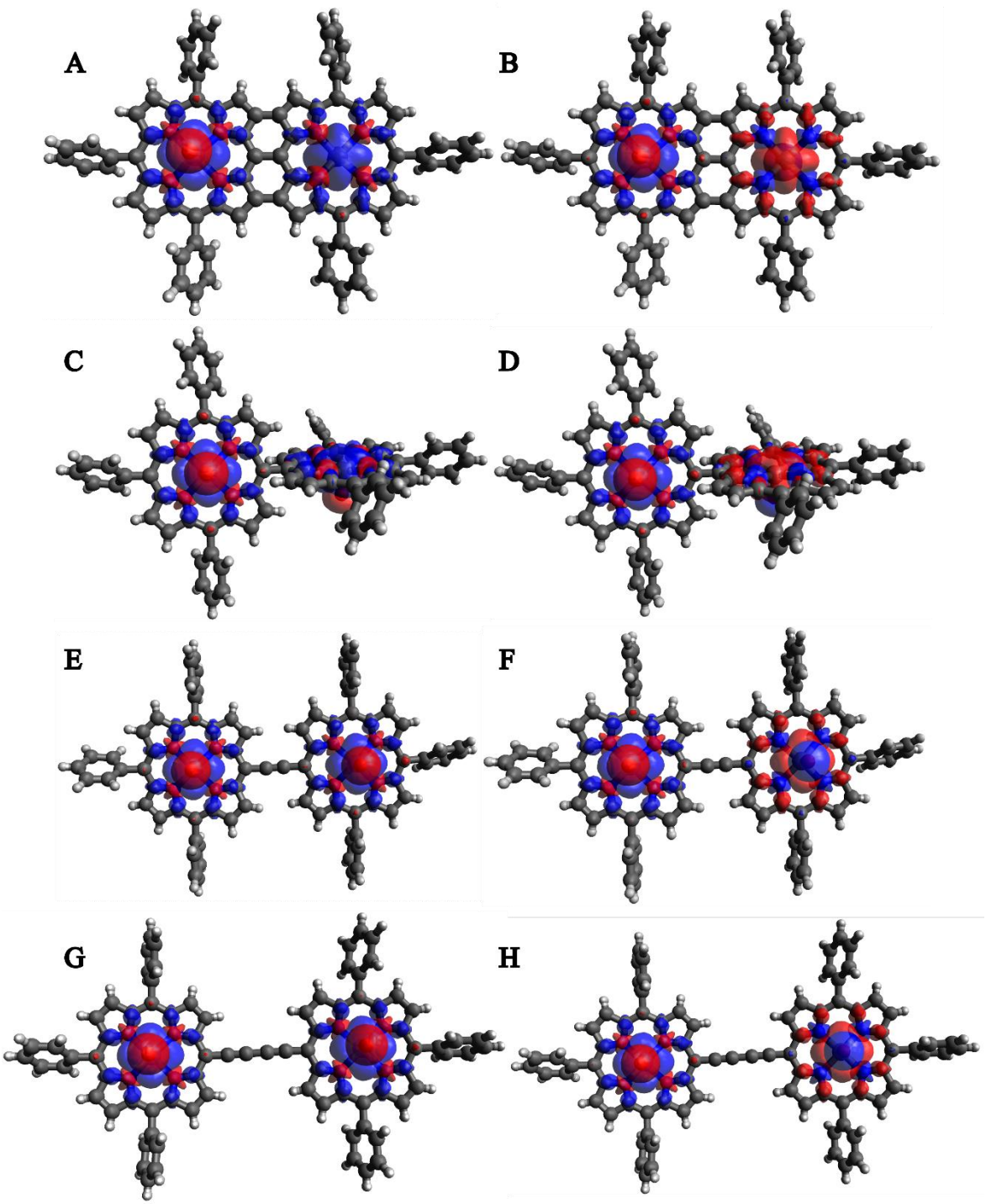

Figure 3.11 The spin density distributions of the *anti*-, *sl*-, *al*-, and *bl*-dimer in the triplet state (A, C, E, and G) and the singlet state (B, D, F, and H), respectively, with iso value 0.0002. Blue colour represents positive spin densities, and red colour represents negative spin densities.

3.3 Spin dynamics

3.3.1 Spin–spin relaxation time

The spin–spin relaxation time describes how long spins can maintain relative phase. Here, to investigate the relationship between molecular structure and coherence property, including different side groups and different connecting linkers. We investigated the coherence properties of nine molecules, shown in Table 3.6. The *syn*-dimer, *anti*-dimer, and *sl*-linked dimers have no or negligible modulations in the time traces of the Hahn-echo decay. A stretched-exponential model was used to fit the spin–spin relaxation times. For all other molecules, however, strong modulations are involved in time traces of the Hahn-echo decay. More than two strong and effective modulations are involved in the time traces, so it is inappropriate to use modulated exponential model to extract T_m. Therefore, T_m was extracted using local minima in the data. Firstly, a low-pass filter was used to filter high-frequency noises and find local minima. Secondly, we then extracted several data points centred on each local minimum within a fixed tolerance to decrease the influence of the signal noise and make the T_m results more reliable. Thirdly, we fit these extracted data points to a mono-exponential model. Figure 3.12 displays the details involved in this fit. The $\pi/2$ pulse is 24 ns and π pulse length is 48 ns. The B_0 is set at the magnetic field position where the EDFS spectrum has a largest peak.

Table 3.6 The modulation strength of the time traces of different molecules.

Side	**monomer**	***syn***	***anti***	***sl***	***al***	***bl***
THS	–	none	None	negligible	strong	strong
tBu	strong	–	–	negligible	strong	strong

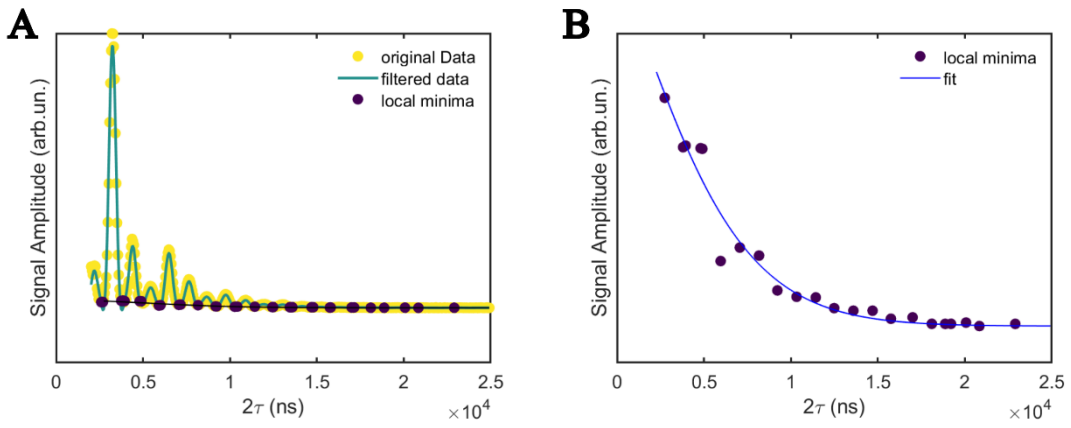

Figure 3.12 (A) Local-minima-extracting method and (B) a fit of local-minima data. In the left graph, yellow circles represent the original data, the green line represents the filtered data after filtering low frequency noise, and the dark purple circles represent local minima extracted from the filtered data. In the right graph, the dark purple circles represent the local minima data, the blue line is the fit.

For the Hahn echo without intense modulations, we used a stretched-exponential model to fit the data, including *syn*-, *anti*-, and *sl*-linked dimer. Figure 3.13 shows the Hahn-echo decay of the *anti*-dimer across the measurement's entire temperature range and its corresponding fit using a stretched-exponential model.

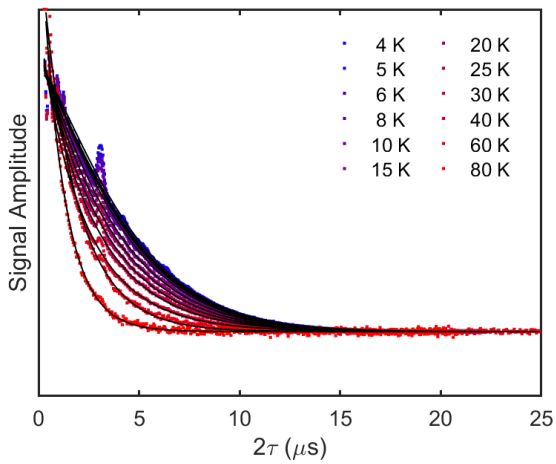

Figure 3.13 The Hahn-echo decay of the *anti*-dimer molecule at different temperatures and corresponding fits using a stretched-exponential model.

All the molecules measured for T_1 and T_m were prepared in 1 mM d8-toluene solutions. We can make valuable conclusions by comparing the T_m results of all these molecules. As we can see from Figure 3.14, the side group significantly affects the coherence time. In the *sl*-linked dimer, *al*-linked dimer, and *bl*-linked dimer, the molecules with a tBu group have larger coherence times than those with a THS group, within the measured temperature range. In the THS and tBu groups, the main magnetic nuclei are hydrogen nuclei, since the natural abundance of other possible magnetic nuclei like ^{13}C or ^{29}Si is low, 1.1% and 4.7%, respectively. Since the natural abundance of ^{1}H is 99.99%, we can consider all the isotopes of H to be ^{1}H in this case, without losing accuracy. Each tBu group has nine magnetic hydrogen nuclei, but the THS group has thirty-nine magnetic hydrogen nuclei. From the chemical structure of these two side groups, however, we know that the average distances between the hydrogen nuclei and vanadyl ion in the tBu group are less than those in the THS group, which means that each hydrogen nucleus in the tBu group more strongly influences decoherence than in the THS-group. We can conclude from Figure 3.14 that although the average distance between the magnetic hydrogen nucleus and the vanadyl atom is larger, the thirty-nine magnetic hydrogen nuclei in the THS group can collectively create larger magnetic noise than the nine magnetic hydrogen nuclei in the tBu group can, and this greater noise thus leads to faster decoherence. The molecules with a tBu group can have 1–2 μs larger T_m than those with a THS group.

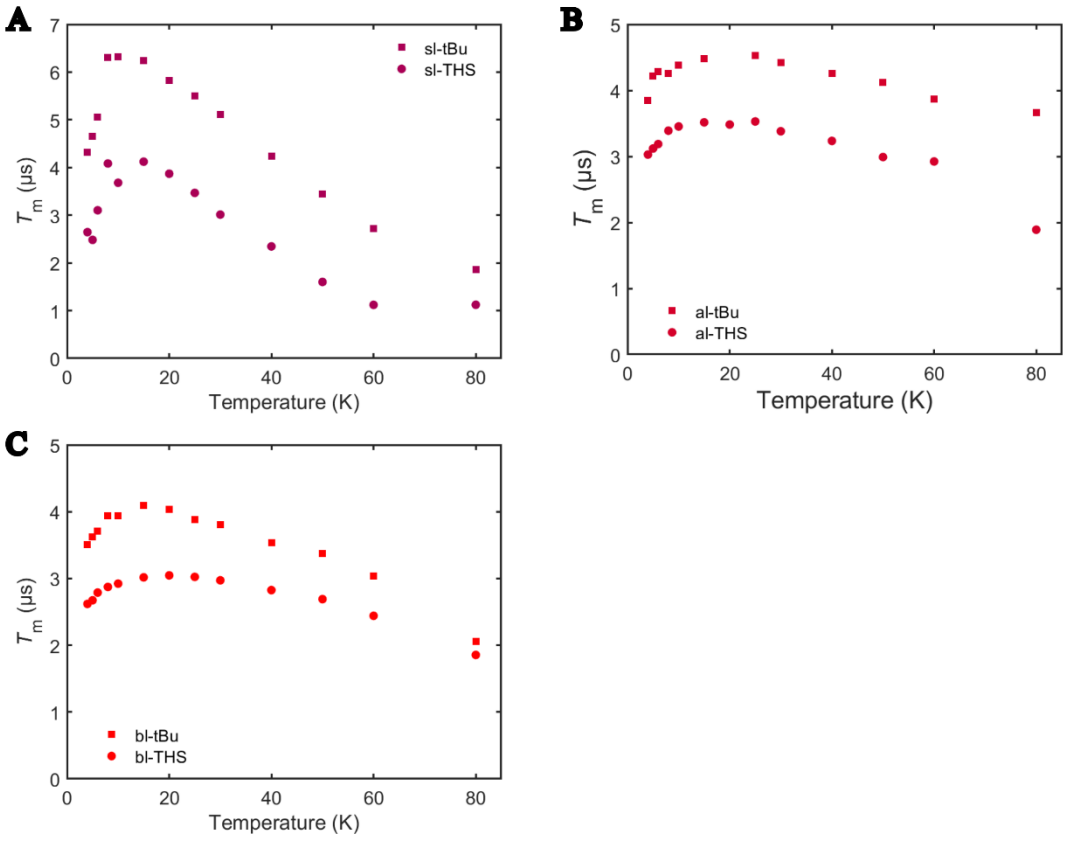

Figure 3.14 The comparison of T_m in molecules with different side groups, including tBu and THS-group in *sl*-linked dimer (A), *al*-linked dimer (B), and *bl*-linked dimer (C). The squares represent the results of molecules with THS side groups, the circles represent the results of molecules with tBu side groups.

In order to investigate how isotropic exchange coupling affects the relationship between coherence time and temperature, we used pulsed EPR to obtain the Hahn-echo decay at various temperatures, extracted coherence times, and compiled them into Figure 3.15 to analyse the results. As we can see from Figure 3.15 (A), compared with the monomer's, the coherence times of the dimers do not significantly decrease, which is consistent with reported vanadyl porphyrins [21]. Since coherence-time data from Hahn echoes with and without strong modulations are treated differently, it is better to compare results obtained from using the same treatment. The main reason is that in treating strongly

modulated Hahn-echo decay, even though we used local minima data points to extract the coherence, which might be the best method to treat such data, this method can incorporate some systematic deviation from the actual coherence time. As shown in Figure 3.15, the *al*-linked dimer has a larger coherence time than the *bl*-linked dimer, for both a tBu group and a THS group, within the considered temperature range.

Furthermore, the *anti*-linked dimer has a larger coherence time than the *sl*-linked dimer within the whole temperature range. Therefore, we can conclude that isotropic exchange coupling resists the decoherence because of the environment and enhances coherence time. Such a phenomenon has been reported in other systems, like exchange-coupled spins in two Ti atoms [83] and quantum dots coupled by a mediator [84]. At temperatures higher than 20 K, the coherence times of all the molecules show a decreasing trend because of the classical rotation of the methyl group of the molecule and the matrix (d8-toluene), which is consistent with the results reported in Cu- and Ti-based, bimetallic molecular spins [6] and open-shell graphenoids with pentagonal units [85]. In this temperature range, the thermal energy of the methyl group can lead to its classical rotation, therefore resulting in the inversion of the nuclear spin state of the three hydrogen nuclei in the methyl group and finally enhancing the decoherence because of spectral diffusion [86,87].

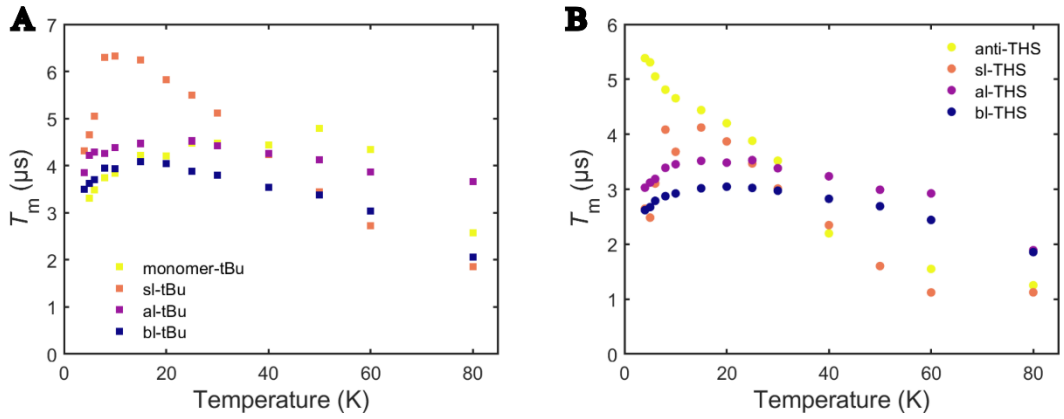

Figure 3.15 The comparison of T_m in molecules connected by different linkers with different side groups, tBu (A) and THS (B).

At low temperatures between 4 K and 25 K, the coherence times of all molecules, except for the *anti*-dimer, increase as the temperature increases. According to the literature, quantum-tunnelling rotation dominates at such a low temperature, and as the temperature increases, the frequency of quantum-tunnelling rotation decreases [88].

Figure 3.16 shows that the relative orientation of two vanadyl ions in the dimeric structure does not have a considerable influence on the dimer's coherence time. This result is reasonable, because such a structural difference does not influence the environment of the vanadyl ion or the exchange-coupling strength, as shown in the section on magnetic properties. The *anti*-dimer has a larger coherence time within the temperature range. It is consistent with the fact that the exchange coupling of the *anti*-dimer (899 MHz) is larger than that of the *syn*-dimer (809 MHz). Naturally, this structure is more immune to the magnetic fluctuations of the environment.

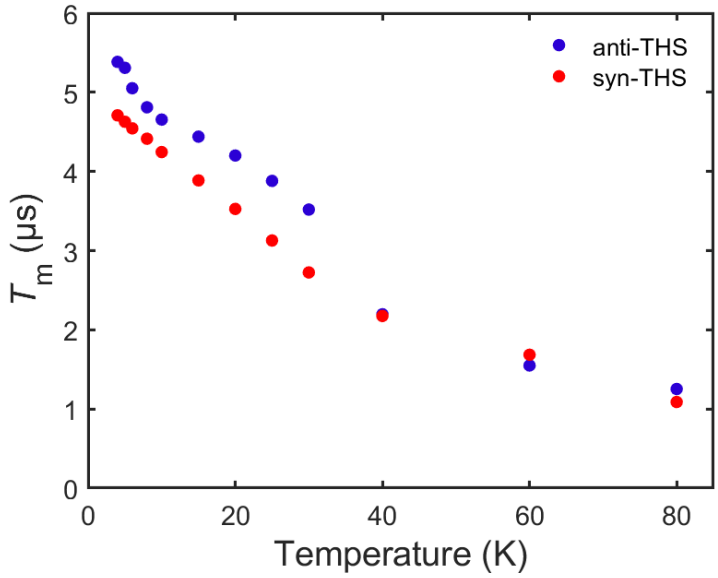

Figure 3.16 The comparison of coherence times of *anti*- and *syn*-THS molecules. The blue points represent the T_m results of *anti*-THS molecule, and red points represent the T_m results of *syn*-THS molecule.

3.3.2 Spin–lattice relaxation time

The spin–lattice relaxation time (T_1) is the time that the spin population needs to return to the thermal-equilibrium state from an excited state. First, in pulsed EPR, it also determines the optimal repetition time in a pulse sequence to obtain high signal-to-noise ratios. Second, it determines the upper limit of T_m according to $2T_1 \geqslant T_m$.[89] Third, in quantum-information processing, T_1 determines the spin's initialization speed[6]. Typically, T_1 is much larger than T_m at low temperatures, so T_1 would not become a factor that restricts T_m. The value of T_m, however, might approach that of T_1, near the theoretical limit at high temperatures. Thus, in this case, we need to find methods to improve T_1 and T_m simultaneously. Because of this constraint by T_1, it behoves us to investigate these molecules' T_1. The spin–lattice-relaxation time in our work was obtained using the Picket Fence pulse sequence because this pulse sequence suppresses the spectral diffusion in order to extract T_1 more accurately. We used

Q-band frequencies with the magnetic field fixed at the maximum peak of EDFS spectra to get high signal-to-noise ratios. Slight field dependence can be neglected. The equation of fit used to extract T_1 is

$$y = A_1 e^{-\frac{t}{T_1}} + A_2 e^{-\frac{t}{T_{fd}}} + y_0, \tag{3.11}$$

where the variable meanings have been detailed in the previous chapter.

As shown in Figure 3.17 and Figure 3.18, all T_1 values decrease monotonically as the temperature increases. Below 80 K, there are mainly two mechanisms involved in spin–lattice relaxation, the direct process and the Raman process. Reasonably, the equation of fit is

$$\frac{1}{T_1} = \mathrm{A}_{dir} T + \mathrm{A}_{\mathrm{Ram}} \left(\frac{T}{\theta_{\mathrm{D}}}\right)^9 \int_0^{\frac{\theta_{\mathrm{D}}}{T}} x^8 \frac{\mathrm{e}^x}{(\mathrm{e}^x - 1)^2} \mathrm{d}x. \tag{3.12}$$

As we can see from Figure 3.17 and Figure 3.18, in all these molecules, at low temperatures from 4 K to around 20 K, relaxation is dominated by the direct process. In contrast, at high temperatures, the Raman process dominates spin–lattice relaxation. All the fits are listed in Table 3.7.

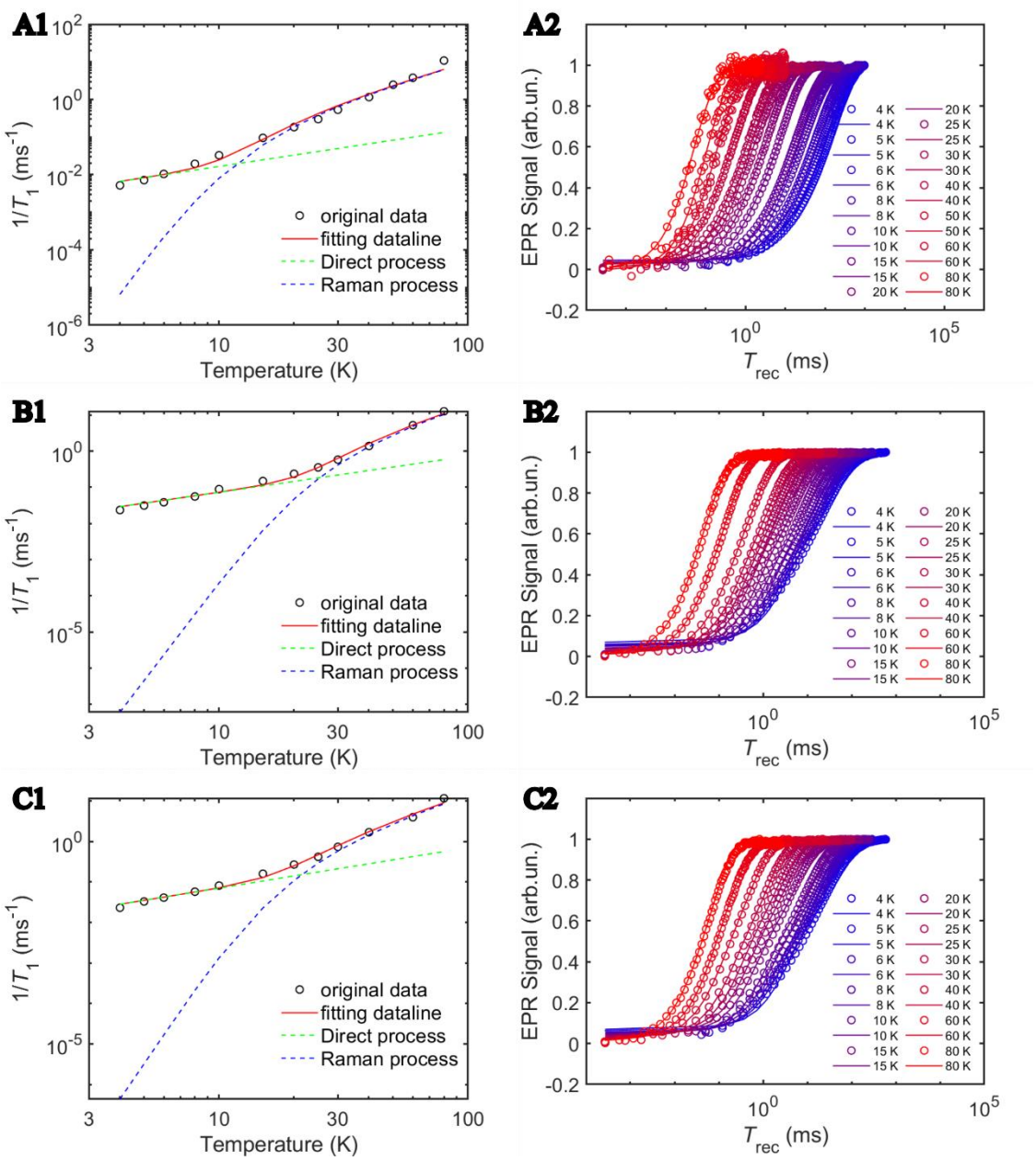

Figure 3.17 The spin–lattice-relaxation times (1) for monomer-THS (A), *syn*-THS (B), *anti*-THS (C), and the corresponding time traces of the spin–lattice-relaxation time measurements and their fitting lines (2). Direct and Raman processes are considered as the main spin–lattice-relaxation mechanisms.

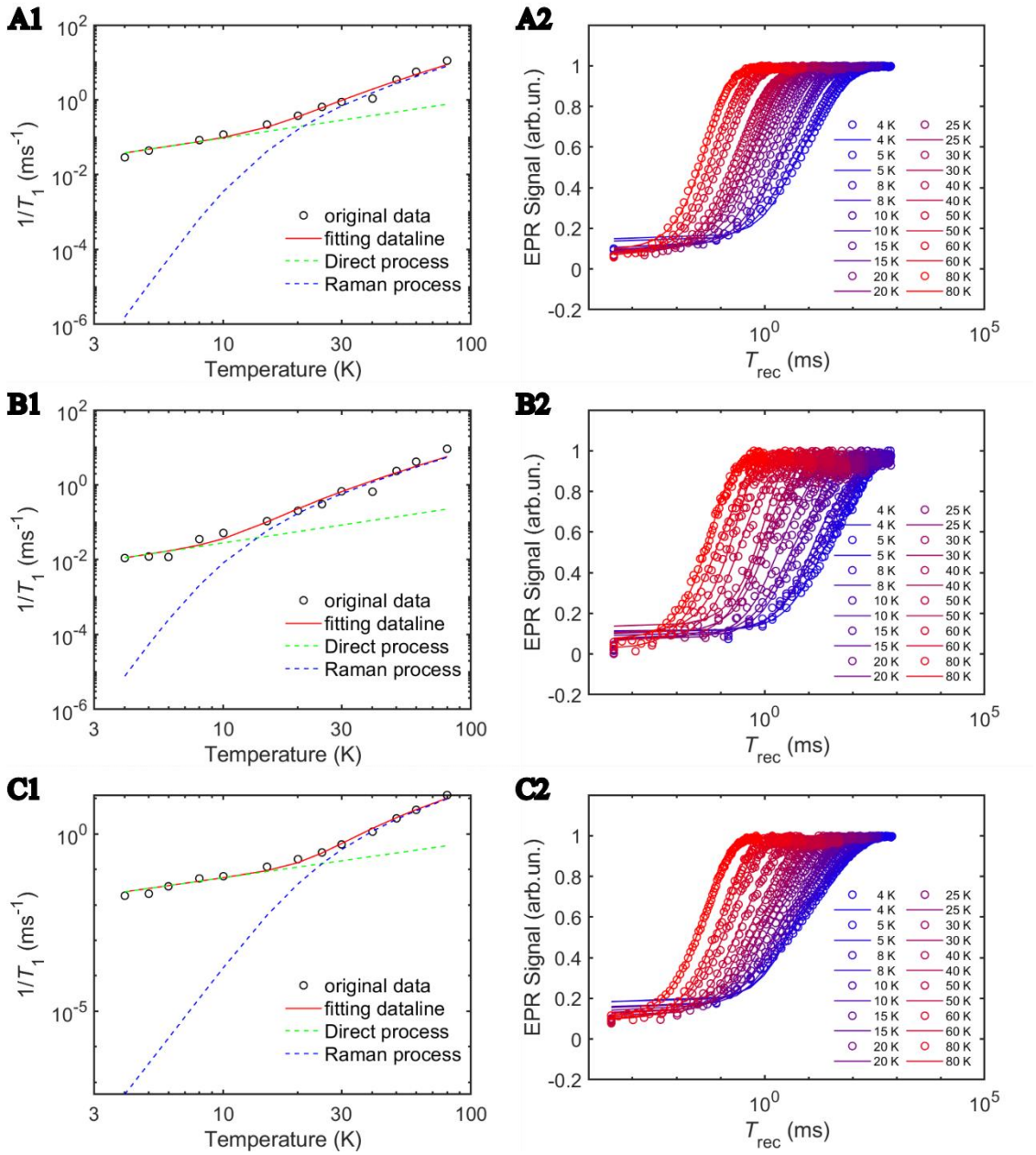

Figure 3.18 The spin–lattice-relaxation times (1) for *sl*-tBu (A), *al*-tBu (B), *bl*-tBu (C), and the corresponding time traces of the spin–lattice-relaxation time measurements and their fitting lines (2). Direct and Raman processes are considered as the main spin–lattice-relaxation mechanisms.

Table 3.7 All the relaxation fitting parameters for these molecules.

Molecule	monomer-THS	*syn*-THS	*anti*-THS	*sl*-tBu	*al*-tBu	*bl*-tBu
A_{lin} **(s^{-1})**	1.66	7.33	7.04	9.58	2.82	11.50
A_{Ram} **(s^{-1})**	3.87×10^4	3.71×10^5	1.38×10^5	8.50×10^4	3.14×10^4	2.05×10^5
θ_D **(K)**	73.4	159.0	114.5	94.01	70.44	145.1

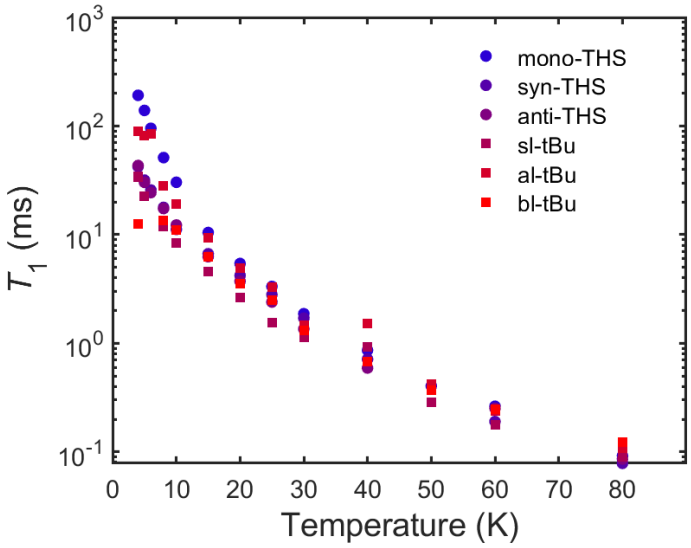

Figure 3.19 The spin–lattice-relaxation time for six molecules, respectively, in d8-toluene from 4 K to 80 K.

As we can see from Figure 3.19 of all these six molecules, different molecules do not show much difference in T_1 values across the whole temperature range. Therefore, based on the vanadyl porphyrin unit, tuning of the molecular structure does not have much influence on the T_1. However, it is not a limiting factor yet in our case since $T_m << T_1$.

3.3.3 Rabi oscillations

Measuring Rabi oscillations have two main reasons here. First, they can be used to identify the total spin quantum number of a spin system. Here, a standard sample (GNR with radical defects, which has a spin quantum number S = 1/2) was put into a smaller size tube and then into a large tube loading syn dimer solution. According to the Rabi frequency equation:

$$\omega(m_s, m_s + 1) = \frac{g\mu_B B_1}{\hbar}[S(S+1) - m_s(m_s+1)]^{1/2} . \quad (3.13)$$

This equation means that the Rabi frequencies depend on the magnetic component of microwaves B_1, the total quantum spin number S and the two magnetic spin quantum states between which the transition happens, m_s and m_s +1, respectively. In this case, we want to confirm that the spin system of the *anti*-dimer is S = 1 or S = 1/2. If the S = 1, $\omega(-1,0) = \omega(-1,0) = \sqrt{2}\frac{g\mu_B B_1}{\hbar}$. Otherwise, if S = 1/2, $\omega\left(-\frac{1}{2}, \frac{1}{2}\right) = \frac{g\mu_B B_1}{\hbar}$. Here the standard sample is the pristine GNR with defects that have S = 1/2. Here, the standard sample is put into a 1.6 mm outer diameter tube and then this tube is inserted into the other 3 mm outer diameter tube containing *anti*-dimer solution. So, with such an experimental design, the B_1 can be kept the same for the standard sample and *anti*-dimer. Furthermore, it prevents the possible reaction between the standard sample and the *anti*-dimer. Figure 3.20 shows the EDFS spectrum of standard sample and *anti*-dimer. The narrow and strong peak corresponds to the signal of the standard sample, the broad and weak peak corresponds to the signal of the *anti*-dimer.

Here the Rabi oscillation experiments were carried out without adjusting other experimental parameters but just changing the magnetic field from the peak of the standard sample to the peak of the *anti*-dimer compound. Figure 3.21 shows FFT results of Rabi oscillation. The Rabi frequency of the standard sample is 10.98 MHz, but that of the *anti*-dimer is 13.67 MHz. The ratio between these frequencies is 1.24, which is close to the theoretical result of $\sqrt{2}$. Therefore, it is confirmed that two electrons in the *anti*-dimer

molecule are so strongly coupled that it is appropriate to view this molecule as a spin system with a total quantum spin number $S = 1$.

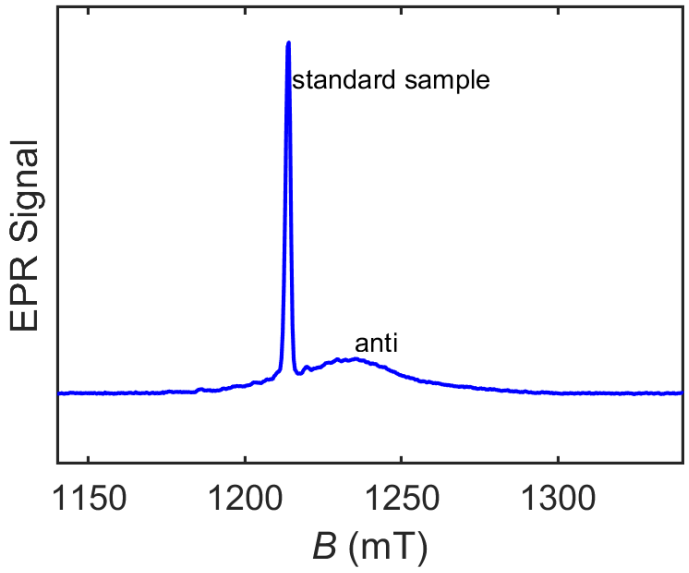

Figure 3.20 The EDFS spectrum of the standard sample and *anti*-dimer compound solution in d8-toluene at a concentration of 1mM with the pulsed-EPR experiment at 35 K using Q-band.

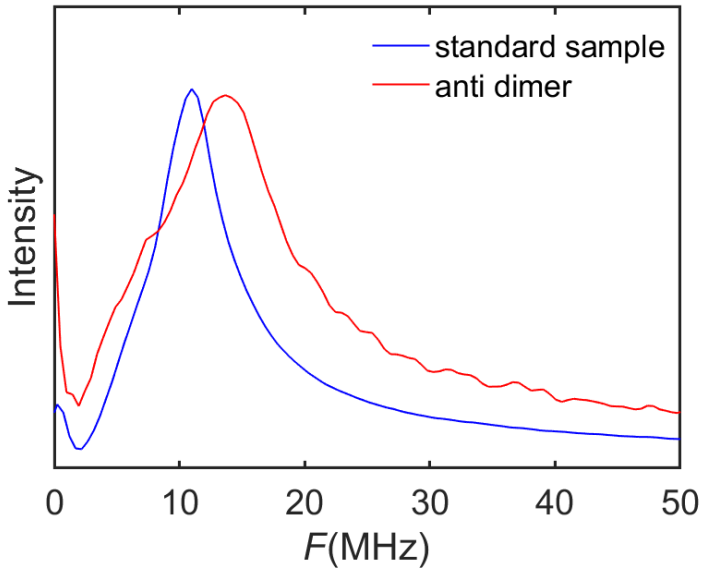

Figure 3.21 FFT results of the Rabi oscillations. The red line is the result of *anti*-dimer, and the blue line is the result of standard sample.

The other reason of performing Rabi oscillation experiments is to manipulate the spin onto any arbitrary state on the Bloch sphere. The Rabi oscillation is the basis of single-qubit and two-qubit quantum gate operations, which are the bedrock of quantum information processing at a large scale. Rabi oscillations were performed using different pulse powers to show that the peaks originate from the Rabi oscillations but not from hyperfine couplings or artefacts of the cavity.

Figure 3.22 shows all the Rabi oscillations results in these three dimer molecules. The B_1 is proportional to the square root of the power of the microwave. We could see from the final linear relationship between the Rabi frequencies and the relative intensity of the B_1, which means that such a signal comes from the nutation of the spin, not from artefacts. Thus, we could manipulate the spin in these molecules at a specific rate onto any arbitrary state on the Bloch sphere by using a pulse with different strengths or lengths.

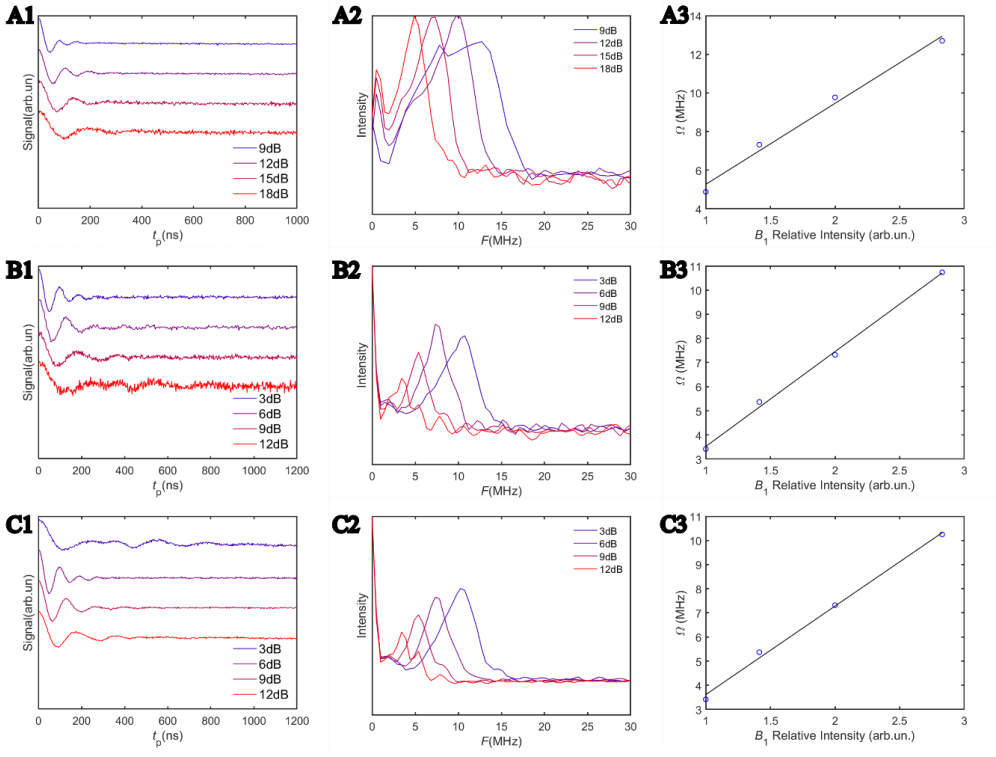

Figure 3.22 Time traces of Rabi oscillations (1), the corresponding FFT results (2), and the linear relationship between relative intensity of the pulse and the Rabi frequencies (3) in *sl*-dimer (A), *al*-dimer (B), and *bl*-dimer (C), in d8-toluene at 10 K.

3.3.4 Instantaneous diffusion

The coherence time of the unpaired spins in the porphyrin structures would influence the investigation of the structure and dynamics of the nanostructures surrounding the unpaired electrons. On the other hand, a long coherence time is an essential element that ensures a high fidelity of quantum gate operations using porphyrin-based blocks as qubits. Thus, it is crucial to investigate the decoherence mechanisms in these vanadyl porphyrins. As mentioned in the previous part, the coherence time T_m is mainly influenced by two factors. One is the molecular motions, and the other one is magnetic interactions. The molecular motions, such as classical methyl rotations and liberations, can be mainly eliminated at a relatively low temperature, which is molecular system dependent and typically lower than the temperature of liquid nitrogen. However, some quantum methyl rotations can still appear at such low temperatures in some molecular systems. The magnetic interaction can be intermolecular, intramolecular, and between molecules and matrix. Although the concentrations of all the molecules are low (1 mM) to supress the intermolecular interactions, it is still interesting to check for instantaneous diffusion contributing to the decoherence. Instantaneous diffusion is mainly determined by two factors: the concentration of the molecules and the refocusing angle (θ) in the Hahn echo pulse sequence. The refocusing angle is decreased gradually by decreasing the microwave power. The exact mathematical expression of the contribution of instantaneous diffusion is $\frac{1}{T_{ID}} = C\frac{\pi}{9\sqrt{3}}\frac{\mu_0 g_1 g_2 \beta_e^2}{\hbar} sin^2\frac{\theta}{2}$. We can use an extrapolating experiment by adjusting the refocusing angle θ to extract this term through using this equation:

$$\frac{1}{T_m'} = \frac{1}{T_m} + C\frac{\pi}{9\sqrt{3}}\frac{\mu_0 g_1 g_2 \beta_e^2}{\hbar}\sin^2\frac{\theta}{2}. \tag{3.14}$$

T_m' is the coherence time getting rid of instantaneous diffusion, the T_m is the coherence time obtained from the Hahn echo sequence with a refocusing angle θ, C is a parameter

determined by the concentration of the molecules. Since the term $C\frac{\pi}{9\sqrt{3}}\frac{\mu_0 g_1 g_2 \beta_e^2}{\hbar}$ is a constant and does not change during such an extrapolating experiment, by substituting $C\frac{\pi}{9\sqrt{3}}\frac{\mu_0 g_1 g_2 \beta_e^2}{\hbar}$ with a parameter *k*, the equation can be further reduced to,

$$\frac{1}{T_m'} = \frac{1}{T_m} + k\sin^2\frac{\theta}{2}. \tag{3.15}$$

The refocusing angle θ was adjusted by tuning the attenuation of the pulse power. The refocusing angle has such a relationship with the pulse power: $\theta = B_1 t_p$. The Hahn echo is optimised, when the attenuation is set at 6 dB. Thus, an attenuation of 6 dB corresponds to a 180° refocusing angle. Then, increasing by 1 dB, the pulse power decreases to 0.794 of the original value. The attenuation values used in this project are 6, 7, 8, 10 dB corresponding to refocusing angles 180°, 143°, 114°, and 72°, respectively.

The time traces of the Hahn echoes of different refocusing angles are shown in the left diagram of Figure 3.23. As we can see from this diagram, tuning the refocusing angle results in slightly stronger noise but does not lead to a large change in the time trace of the Hahn echo decay, which means that instantaneous diffusion is not very significant. The right diagram of Figure 3.23 shows the extrapolating fitting plot and T_m without the influence of instantaneous diffusion is 2.490 μs. T_m with a standard 180° refocusing pulse is 2.431 μs. Thus, the instantaneous diffusion affects T_m value by 2.4%, which justifies that the magnetic interactions between the electrons in different molecules are negligible.

Here, the instantaneous diffusion refers to a sudden change of the spin's resonance frequency [26]. To be specific, if spin A is coupled with another spin B through dipolar coupling, after a pulse, if the orientation of spin B is also changed, the resonance frequency of spin A can be changed.

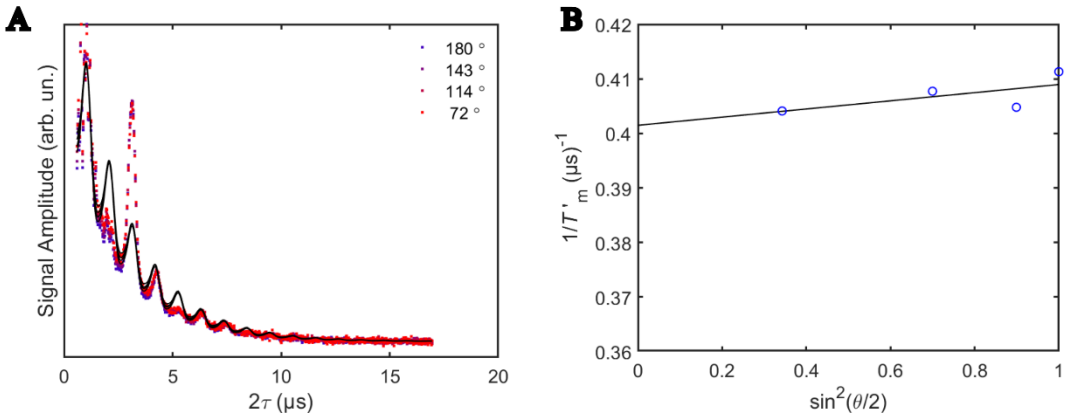

Figure 3.23 The left graph shows the time trace of Hahn echo for the bl-linked dimer with different refocusing angles at 60 K at Q-band. The right graph shows extrapolating fit used to estimate the T_m without the influence of instantaneous diffusion. When refocusing angle approaches 0, T_m is 2.490 μs.

3.4 Summary

In this chapter, we investigated the magnetic and quantum properties of a family of nine porphyrin molecules, a monomer and dimers with different linkers and different side groups. Concerning the magnetic property, several essential processes were used here to fit the CW-EPR spectra of the solutions of the compounds. First, establish the dominating spin Hamiltonian by deleting some negligible terms, which do not influence the spectra, such as hyperfine couplings to hydrogen and nitrogen nuclei. Second, specify appropriate tensor frames for all the tensors involved in the dominating spin Hamiltonian and set up the molecular frame according to the symmetry of the molecule. Third, rotate all the tensor frames into the molecular frame with the help of XRD data. Moreover, it is better to use a coupled representation in the case of a strongly coupled system. This treatment can be straightforwardly applied to vanadyl porphyrin trimer structures or other similar porphyrin dimers. In the triply-linked dimer, the isotropic exchange coupling is relatively large (899

MHz for *anti*-dimer and 809 MHz for *syn*-dimer) because of the delocalisation of unpaired electrons from the vanadyl ion into the linker and, therefore, a large wavefunction overlap between the two unpaired electrons. In *sl*-, *al*- and *bl*-linked dimers, the isotropic exchange coupling decreases exponentially, which are 269 MHz, 14.67 MHz, and 10.74 MHz respectively, since the overlap of the unpaired electrons decreases exponentially as the distance between the vanadyl ions increases. Rabi oscillations have been performed to manipulate the electron spin into any arbitrary state on the Bloch sphere. Furthermore, the Rabi oscillation investigation confirmed that compared with the hyperfine coupling and electron Zeeman anisotropy, the exchange coupling of electron spins in the triply-linked dimer is large, and, consequently, the two spins cannot be controlled separately, and it is more appropriate to use a coupled representation ($S = 1$) to describe the spin system.

In terms of quantum properties, we first investigated the relationship between the molecular structure and coherence time. The results show that the dimer structure does not lead to a decrease in the coherence time compared with the monomer one. Coherence times of the *al*-dimer are larger than the *bl*-dimer, independent of the investigated side groups. Furthermore, coherence times of the triply-linked is larger than that of the singly-linked dimer with a THS side group. It confirms that the large coupling strength could resist magnetic field fluctuations leading to an enhanced coherence time. The temperature dependence of coherence time shows that at relatively low temperatures (lower than around 25 K), the quantum tunnelling rotation of methyl groups dominates the coherence property. When the temperature is relatively high (larger than around 25 K), the classical rotation of methyl groups dominates the coherence property. The coherence times of these dimeric molecules are around 2–6 μs, which are slightly larger than that of other vanadium(IV)-based molecular spins with nuclear spin-free ligands in the nuclear spin active solvent d8-toluene (1–3 μs across the measurement temperature range)[71]. However, such a long

coherence time is still lower than a general goal of 100 μs, which is obtained from $\Omega_R T_m > 10^4$–10^5 . The Rabi frequency Ω_R is limited by the pulse power and length of the EPR instrument, which is generally at the order of tens of MHz. However, several techniques can be further performed to improve the coherence time towards a molecular-spin-based practical implementation of quantum information processing on this vanadyl porphyrin system, such as replacing the magnetic nuclei in the molecules with nonmagnetic nuclei or nuclei with smaller gyromagnetic ratio. Furthermore, thanks to the excellent tunability of porphyrin molecules, it is possible to adjust the solubility of these molecules in nuclear spin inactive solvents, such as CS_2, by using different side groups. It was reported that the coherence time of vanadium(IV)-based molecular spin with nuclear spin-free ligands in nuclear spin inactive solvent CS_2 was improved by two orders of magnitude (700 μs at 10 K) compared with the same complex measured in the nuclear spin active solvent d8-toluene[70]. In this project, the Rabi oscillations were performed to prove that it is possible to manipulate the electron spin onto any arbitrary state on the Bloch sphere, which could be further advanced by performing quantum gate operation. The result of the instantaneous diffusion extrapolation experiment shows that the intermolecular electron-electron interaction is small, around 2.4 %, which is expected for a low concentration of 1 mM.

Moreover, the spin–lattice relaxation time was investigated in this project. In all these molecules, the spin–lattice relaxation is mainly dominated by a direct process between 4 K and around 25 K, and is dominated by a Raman process above 25 K. All spin–lattice relaxation times of these molecules are similar within the temperature range of measurement, which means that the adjustment of the molecular structure based on vanadyl does not have a large influence on the spin–lattice relaxation time. Furthermore, the spin–lattice relaxation time is at least two orders of magnitude larger than the coherence time, so that here it is not the limiting factor for the coherence time.

3.5 Project Overview

This project was conducted in collaboration with Prof. Harry Anderson's Group in the Chemistry Department at the University of Oxford. The synthesis of the molecules was performed by Dr Iago Pozo. The EPR measurements of *syn*- and *anti*-dimer were performed by Dr Federico Lombardi, and the other molecules were measured by me. Treatment and analysis of the EPR results were completed by me with some help from Dr Michael Slota and Prof. Lapo Bogani.

4. Benzo-extended open-shell polycyclic aromatic hydrocarbons

4.1 Introduction

Recently, open-shell graphenoids have been used as the quantum unit for quantum technology and organic electronic devices [16,37]. The bottom-up synthesis method has made atomic-level control of molecular graphenoids structure possible. It is interesting to use defects in the honeycomb lattice of the graphene structure to introduce unpaired electrons in the molecule [8]. The cyclohepta[def]fluorene is a representative example of an open-shell polycyclic aromatic hydrocarbon containing a five-membered ring and a seven-membered ring in its structure. However, because of the molecule's instability, the investigation remains at the theoretical stage. Nevertheless, the advanced bottom-up synthesis method makes researching this molecule's derivatives possible. Figure 4.1 shows the chemical structure of the cyclohepta[def]fluorene, which embeds two unpaired electrons inside. Clar's aromatic π-sextet rule and Lieb's theorem are usually used to explain the magnetism of such a polycyclic aromatic hydrocarbon. Clar's aromatic π-sextet rule means that the resonance structure with the largest number of disjoint and aromatic π-sextets is the most stable and contributes most to the ground state for polycyclic aromatic hydrocarbons [90,91]. Namely, the Clar structure is the resonance structure with the largest number of disjoint and aromatic π-sextets, with the least number of localized double bonds [90]. The graph on the left is based on Clar's π-sextet rule, which means there are two sextets and two unpaired electrons in this structure. The two sextets here stabilise this open-shell graphenoid. The graph on the right conforms with Lieb's theorem. Lieb's theorem means that the total spin of the ground state is $(|N_A\text{-}N_B|)/2$ for a bipartite lattice, where N_A and N_B are the number

of atoms in two different lattices [92,93]. In this bipartite lattice, the lattice can be divided into two sublattices, corresponding to the red and blue circles in Figure 4.1. Then, the total spin of the ground state of this molecule is $S = (N_A\text{-}N_B)/2 = 1$, which is a triplet state. After a benzannulation chemical reaction, three cyclohepta[def]fluorene derivatives were synthesised by Wu, shown in Figure 4.2. All these molecules have two unpaired electrons. The six-membered rings with purple colour are the newly added sextets with the molecules' extension, which is why these molecules become stable, and synthesis becomes possible. Clar's rule and Lieb's theorem are presented in Figure 4.2 to show the magnetism of this family of molecules.

In this chapter, we first investigated the magnetic properties of these molecules and the spin interactions within these molecules. Then, temperature dependence of the coherence time was explored. Finally, Rabi oscillation experiments were used to manipulate the electron spins within these molecules, which show their potential applications in quantum information processing.

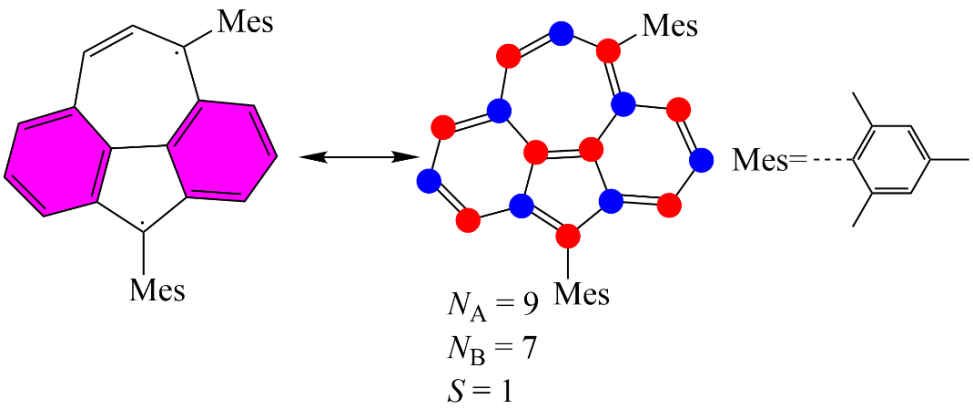

Figure 4.1 The chemical structure of cyclohepta[def]fluorene. The purple rings are the sextet structures. The red and blue circles represent different sublattices, including A and B.

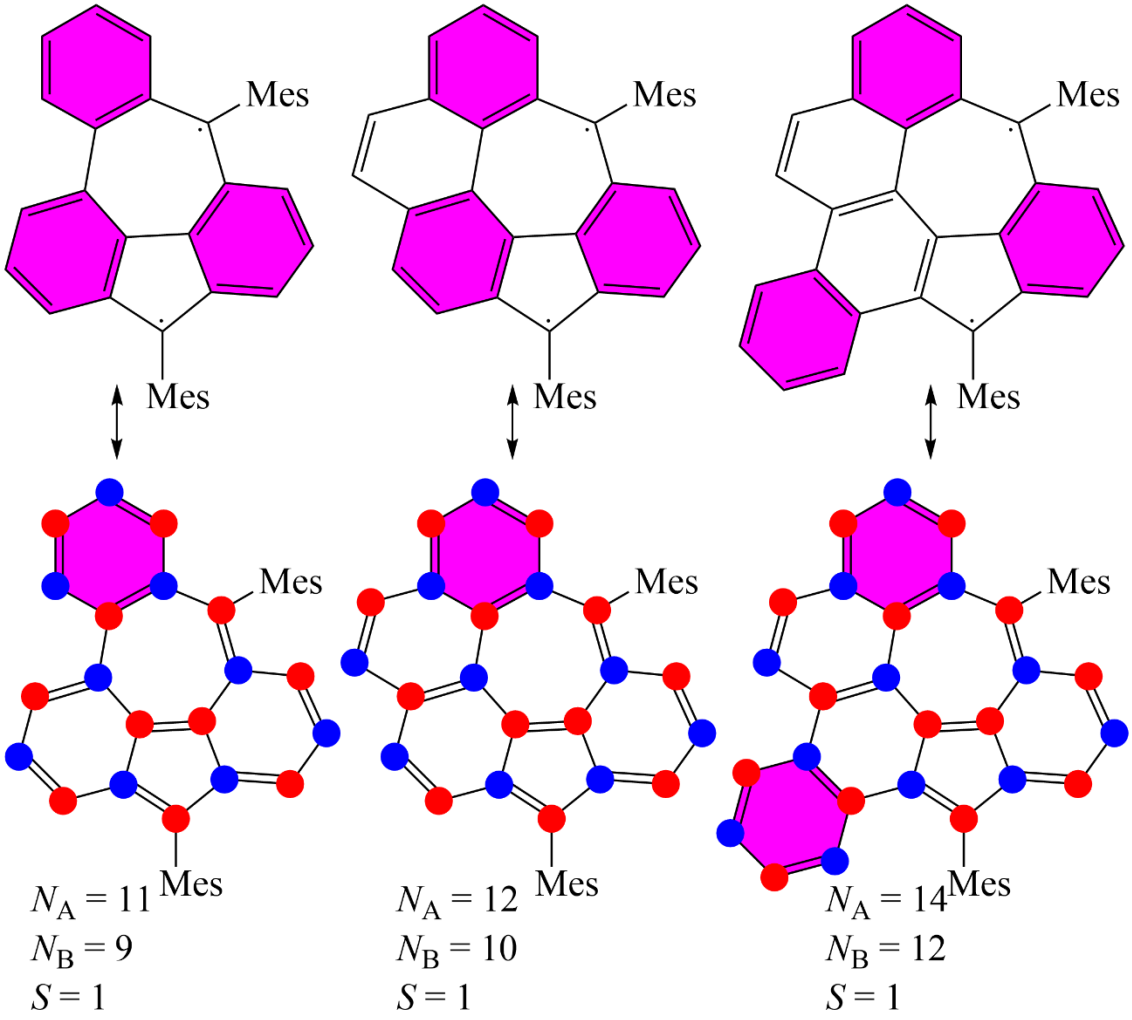

Figure 4.2 Chemical structures of a family of benzo-extended cyclohepta[def]fluorene derivatives corresponding to the labels 1, 2, and 3. Mes represents the mesitylene group.

4.2 Magnetic properties

Figure 4.3 displays CW-EPR spectra using X-band and corresponding simulations of these molecules in d8-toluene solution at room temperature.

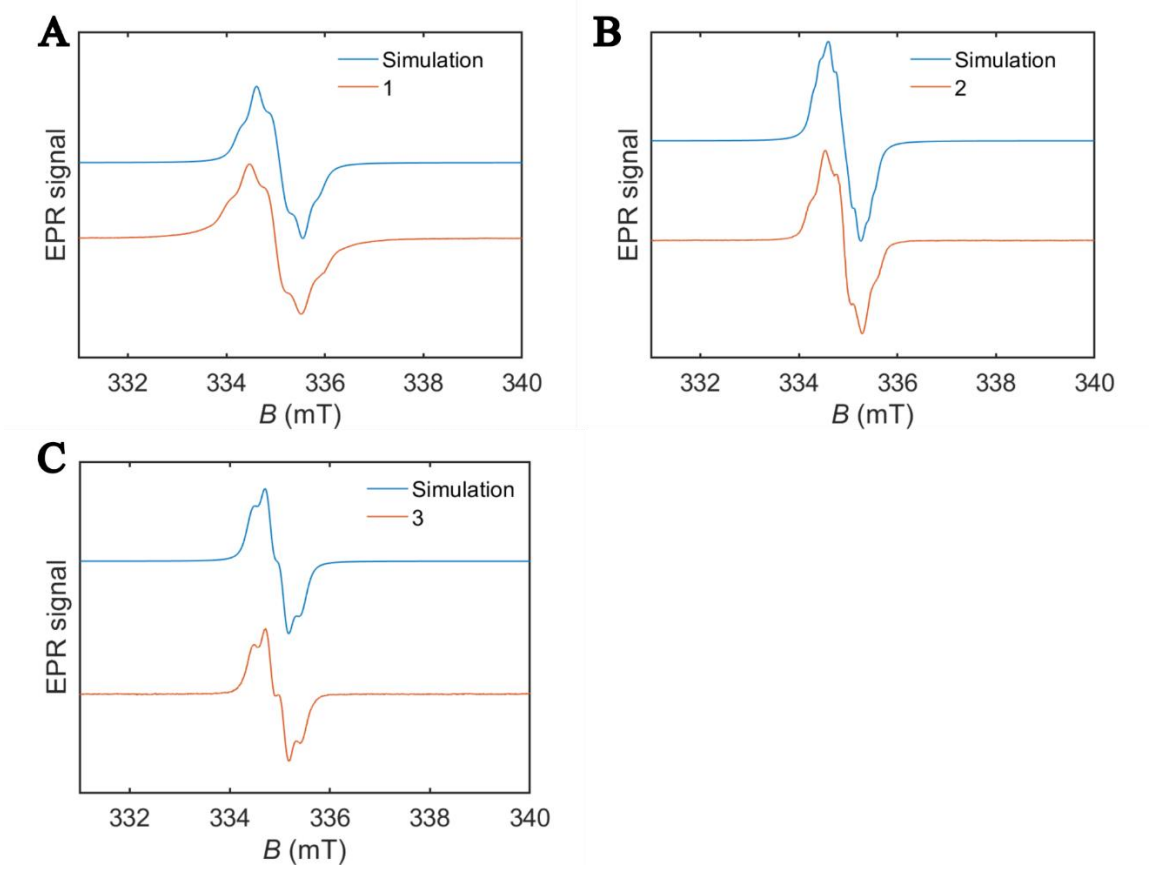

Figure 4.3 CW-EPR spectra of 1 (A), 2 (B), and 3 (C) molecules in d8-toluene solution, and their corresponding simulations at room temperature. The blue lines are the simulations and red lines are the experiment results.

In order to fit CW-EPR spectra of these molecules, we first need to establish the complete spin Hamiltonian of the spin system and then reduce it to the dominant terms according to the CW-EPR spectra. The spin Hamiltonian in this case is as follows,

$$\hat{H} = \mu_B \sum_{i=1}^{2} B\boldsymbol{g}_i\hat{S}_i + \sum_{i=1}^{n} \hat{S}_1\boldsymbol{A}\hat{I}^i + \sum_{i=1}^{n} \hat{S}_2\boldsymbol{A}\hat{I}^i + J\hat{S}_1\hat{S}_2 + \hat{S}_1\boldsymbol{D}\hat{S}_2. \quad (4.1)$$

Figure 4.4 shows all the CW spectra of these molecules in powder and solution states. First, these powder spectra clearly show that these molecules have open-shell electronic structure as predicted using Lieb's theorem and Clar's rule in the previous section. Here, we can see from the powder spectra that there is only one peak with no splittings, which has also been in similar open-shell graphenoids [39].

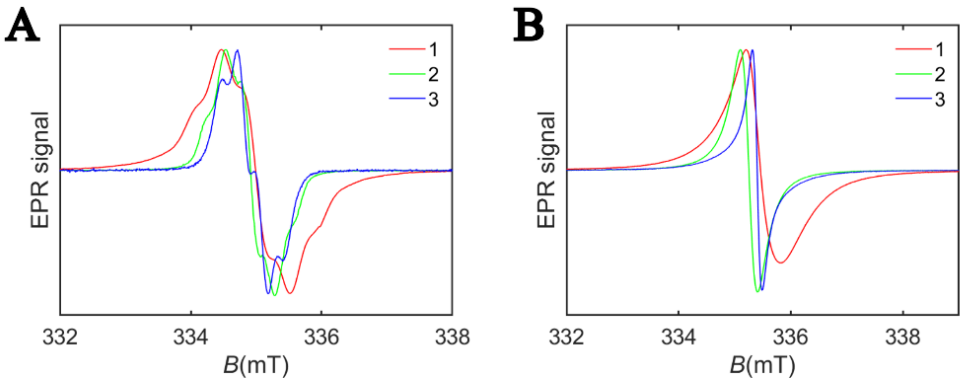

Figure 4.4 The comparison of the CW-EPR d8-toluene solution spectra (A) and powder spectra (B) of these three molecules.

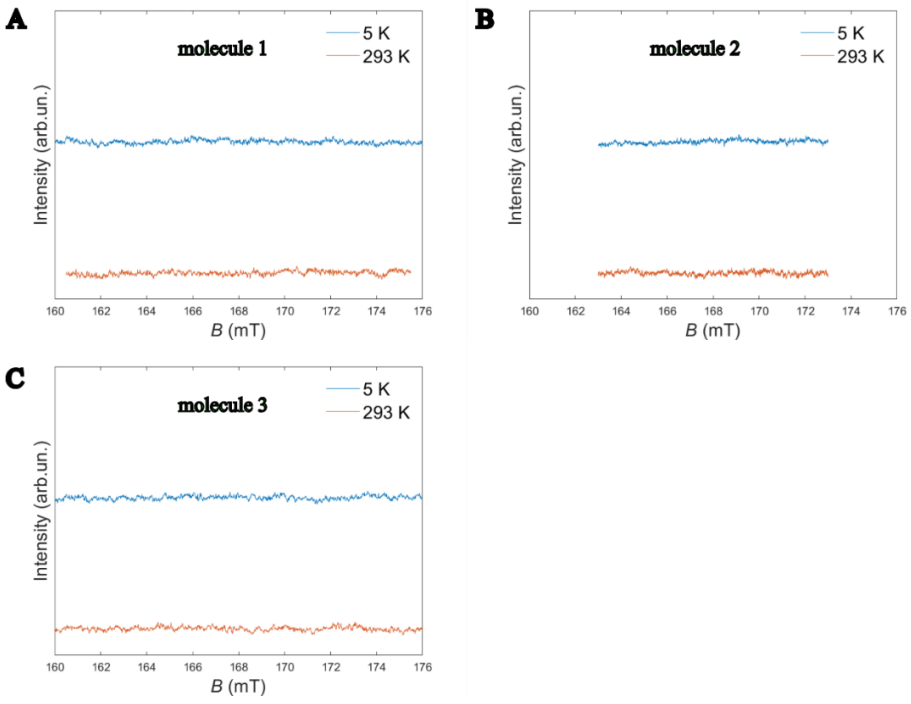

Figure 4.5 Half-field transitions of molecule 1 (A), 2 (B), and 3 (C) in powder states at 5 K and 293 K.

Furthermore, from the solution spectra, we can see more peaks originating from the hyperfine couplings of the hydrogen nuclei in these molecules. Moreover, Figure 4.5 shows that no significant half-field transitions around 167.5 mT at 4 K and 293 K were found in any of these three molecules. In some other molecules containing two coupled electron spins, such as spin labelled copper complexes, it is possible to use the intensity of the half-field transition to measure the distance between two electrons[94]. Because the ratio between integrated intensity of half-field transition and main transition is inverse to the sixth power of inter-spin distance[95]. Here, we know that the two electrons here are so close to each other that the point dipole approximation is inaccurate here, and the dipolar coupling between the two electrons is negligible. Also, the *J* coupling is very strong compared with hyperfine couplings, and hence the coupled representation is better here. Therefore, the dominating part of spin Hamiltonian is

$$\widehat{H} = \mu_B B \boldsymbol{g} \hat{S} + \sum_{i=1}^{n} \hat{S} \boldsymbol{A} \hat{I}^i. \tag{4.2}$$

The energy levels are split into two states: a singlet and a triplet. The singlet state is EPR silent; however, the triplet state is active and is described with a quantum spin $S = 1$. The linewidth used here stems from isotropic convolutional broadenings of a Gaussian and a Lorentzian line shape. These are used to fit the spectra phenomenologically without considering the specific physical origins. Linewidth term is caused by the previous negligible spin Hamiltonian terms, such as the dipolar coupling between the unpaired electrons and the environment's effect, such as the magnetic nuclei in the d8-toluene solvent. From both the powder and solution spectra, another interesting point is that as the size of the molecule increases, the linewidth increases because of the increasing number of magnetic hydrogen nuclei at the periphery of the molecule.

Table 4.1 EPR parameters from fitting all the CW-EPR d8-toluene solution EPR spectra at room temperature for comparison.

Parameters	**1**	**2**	**3**
S	1	1	1
g	2.0026	2.0026	2.0027
A_1 (MHz)	8.32	7.17	8.25
A_2 (MHz)	10.93	6.91	7.71
A_3 (MHz)	9.53	7.44	5.89
A_4 (MHz)	12.25	7.96	–
lw_{Gauss}(mT)	0.23	0.25	0.19
lw_{Lor} (mT)	0.24	0.05	0.10

As we can see from the fitting results shown in Table 4.1, the *g*-factor is close to the free electron's value, which is 2.0023. We attribute this observation to the negligible spin–orbital coupling in this type of molecules. Such a result is also consistent with other reported graphenoids recently [39,85]. Furthermore, the fitting result of the hyperfine coupling is isotropic at room temperature because of the fast tumbling of the molecule in the solvent. The hyperfine couplings come from the hyperfine couplings

For PAHs, the precision of energy is 1.0×10^{-8} au according to the input file settings. The functional is B3LYP/G, and the basis set is EPR II. These choices work well in calculating the EPR-relevant parameters for systems of organic radicals [17]. Figure 4.6 shows the chemical structures of these investigated molecules and the spin-density distributions of the two unpaired electrons. The unpaired electrons mainly concentrate on the positions where the mesitylene group connects to the conjugation backbone of the

structure and spread across the whole conjugation backbone. Most hydrogen nuclei attaching to the conjugation backbone have stronger hyperfine couplings than those in the mesitylene group, mainly because of the larger isotropic hyperfine coupling. The calculated *g* factor is consistent with the fitting result of the CW solution spectra, both of which are close to the free electron value. All the H nuclei in the molecular structure have hyperfine couplings with unpaired electrons, but only some of them show in the CW spectra. The calculated hyperfine couplings and linewidths are shown in Table 4.2. Figure 4.7 shows the comparison of the CW spectra of molecules 1, 2, and 3 obtained from theory and experiment. The values of these calculated hyperfine couplings are similar to the fitting results, which confirms that the previous fitting results are reasonable. The resolved hyperfine couplings by fitting corresponds to some of the largest hyperfine couplings calculation results, which are shown in bold texts in Table 4.7.

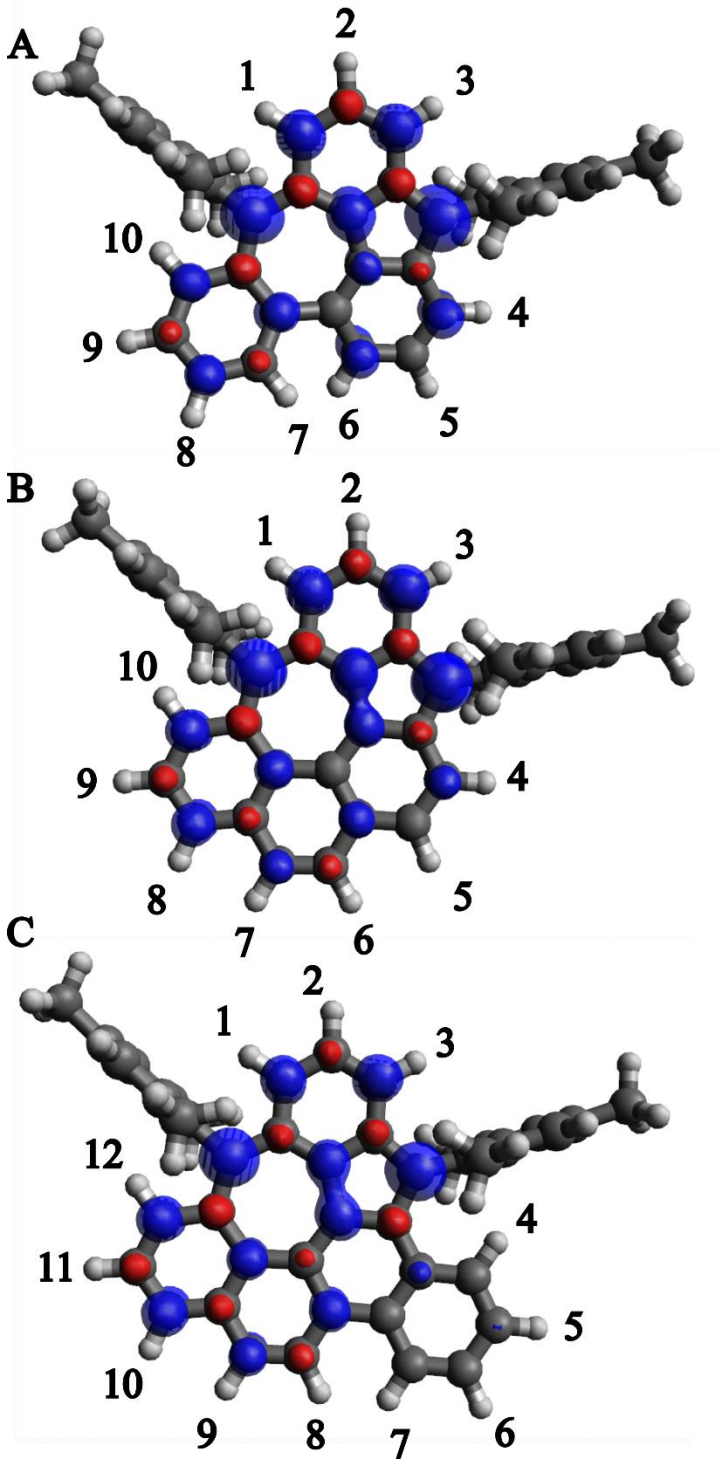

Figure 4.6 The calculated spin density distributions of molecules 1 (A), 2 (B), and 3 (C) in the triplet state with an iso value of 0.005. The functional is B3LYP/G, and the basis set is EPR-II. Blue colour represents positive spin densities, and red colour represents negative spin densities. The labels are used to label the hydrogen atoms in the π-conjugated structures.

Table 4.2 Calculated EPR results of molecules 1, 2, and 3. A negative isotropic hyperfine coupling means that electron spin is in a spin-down state on that atom, however, a positive isotropic hyperfine coupling means that electron spin is in a spin-up state on that atom.

Parameters	**1**	**2**	**3**
g	2.0025	2.0025	2.0025
A_1 (MHz)	**-10.7283**	**-9.6945**	**-8.7538**
A_2 (MHz)	3.0697	-3.0115	2.2965
A_3 (MHz)	**-10.3762**	**-10.0434**	**-9.3008**
A_4 (MHz)	**-6.2051**	-4.2681	1.1211
A_5 (MHz)	0.0827	1.2554	-1.6713
A_6 (MHz)	**-6.2664**	2.3373	0.9159
A_7 (MHz)	1.9813	-4.1434	-1.4095
A_8 (MHz)	-5.1363	**-7.2534**	2.7087
A_9 (MHz)	1.7964	2.6395	-5.3527
A_{10} (MHz)	-5.0760	**-7.1600**	**-8.2088**
A_{11} (MHz)	–	–	3.0636
A_{12} (MHz)	–	–	-8.0709
lw_{Gauss} (mT)	0.001	0.261	0.159
lw_{Lor} (mT)	0.215	0	0

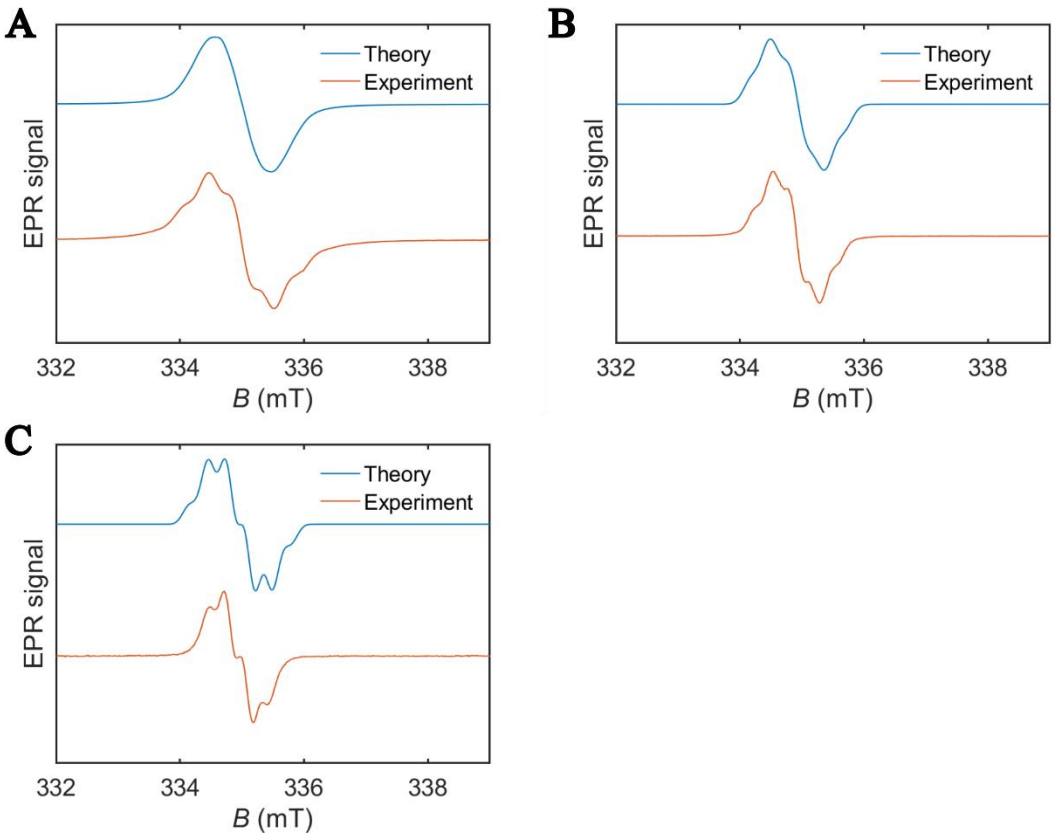

Figure 4.7 The comparison of the CW spectra of molecules 1 (A), 2 (B), and 3 (C) obtained from theory (DFT calculations) and experiment, respectively.

In order to characterise the exchange coupling in these molecules, variable temperature CW-EPR measurements were carried out, and the results are shown in Figure 4.8. The fitting equation used here is the Bleany-Bowers equation[96], which is expressed as follows:

$$\chi T = \frac{k}{3+\exp(-J/k_B T)}, \tag{4.3}$$

where the χ is the magnetic susceptibility, T is the temperature, k is a constant determined from the fit, J is the exchange coupling, and k_B is the Boltzmann constant. Furthermore, the integrated EPR signal is proportional to the magnetic susceptibility, when important instrumental parameters are fixed during the measurement, namely the resonator-filling factor, the Q factor, and the microwave power[17]. Herein, we used the integrated powder

CW spectra signal to extract the exchange coupling in these molecules. The fitting results show that *J* is 493 GHz, 210 GHz, and 199 GHz, respectively. These results prove that the overlap of the unpaired-electron-spin density decreases because of the extension of the conjugation backbone structure of the cyclohepta[def]fluorene. In all these molecules, the singlet state is the ground state, and triplet state is the excited state. The singlet–triplet energy gap here is around two orders of magnitude smaller than that of other graphenoids. For example the singlet–triplet energy gap in the graphenoids with two five-membered ring defects in the molecule is 11646 GHz [85]. Such a result shows that this non-alternant ring-cyclohepta[def]fluorene can create a biradical with a low singlet–triplet energy gap. However, in an alternant π-conjugation system, such a low singlet–triplet energy gap demands a giant size molecule, which is more challenging to synthesize[97]. So such a non-alternant is more promising for applications, such as metal-free magnets and spintronics[98].

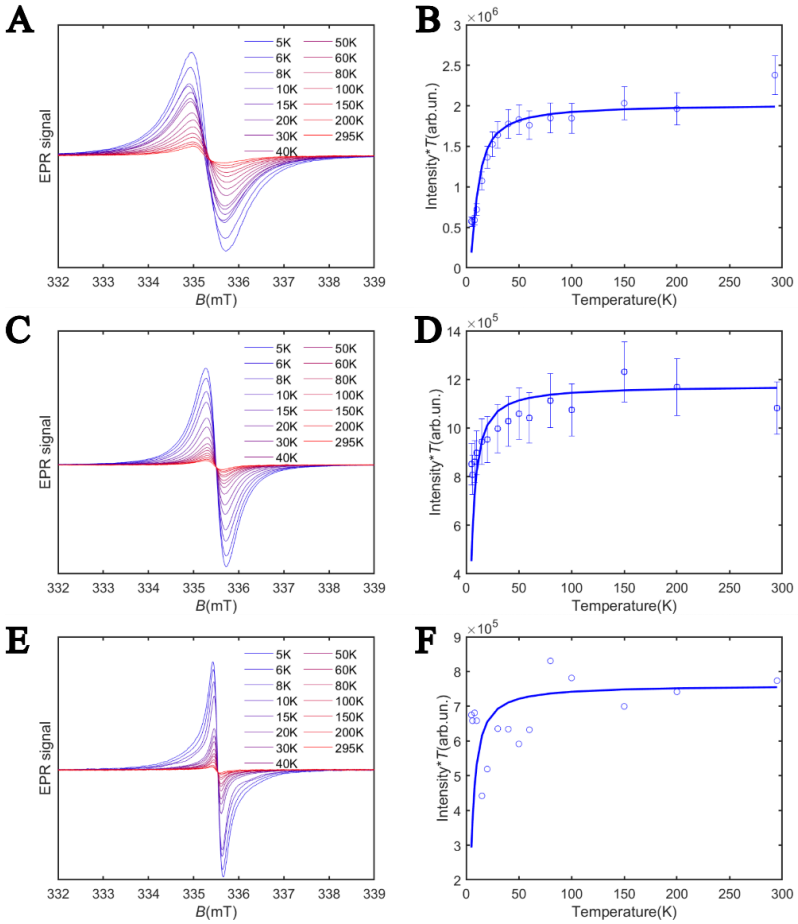

Figure 4.8 CW powder spectra at various temperatures of molecules 1 (A), 2 (C), and 3 (E), and their respective integrated signal intensity multiplied by the temperature at various temperatures with the fits using the Bleaney–Bowers equation (B, D, F), respectively.

4.3 Coherence properties

We analysed the coherence properties of the molecules in order to determine if they are suitable as organic radicals for quantum information processing. Here a nonlinear delay inversion recovery pulse sequence is used to extract T_1, and a Hahn echo pulse sequence is used to obtain T_m. Figure 4.9 shows fitting lines of the inversion recovery and Hahn echo time traces at 80 K at X-band for these three molecules. In molecule 1, the Hahn echo time trace is relatively noisy, and we used the stretched-exponential model without modulations

to fit the data. However, in molecules 2 and 3, the modulations from magnetic nuclei are relatively strong, and we used a modulated stretched-exponential model to fit the data. Modulation frequencies for molecules 2 and 3 both are around 1.1 MHz as shown in Figure 4.9. The magnetic nuclei in this solution are ^{1}H nuclei in the molecule's periphery, the ^{2}H nuclei in the solvent (d8-toluene), and ^{13}C nuclei in the molecule and in the solvent. As mentioned in Chapter 2, the modulation in the 2-pulse ESEEM has such a formula:

$$V_{2\mathrm{p}}(\tau) = 1 - \frac{k}{4}[2 - 2\cos(\omega_{12}\tau) - 2\cos(\omega_{34}\tau) + \cos(\omega_{-}\tau) + \cos(\omega_{+}\tau)]. \qquad (4.3)$$

Each coupled magnetic nuclear spin has four modulation frequencies. ω_{12} and ω_{34} are the nuclear frequencies with the coupled unpaired electron in an up or down state. ω_{-} and ω_{+} are the difference and sum of these nuclear frequencies, respectively. Typically, ω_{12} and ω_{34} are close to the Larmor frequency of the nucleus, ω_{-} is the tiniest, and ω_{+} is the largest one and is close to twice the Larmor frequency of the nucleus. The Larmor frequencies of ^{1}H, ^{2}H, and ^{13}C at X-band are 14.48 MHz, 2.22 MHz, and 3.64 MHz, respectively. In our case, the pulse delay is relatively large (312 ns), and the corresponding upper limit of frequency in the FFT results is 1.6 MHz, as shown in Figure 4.10. According to the literature investigating the magnetic properties of zigzag shape graphenoid in different matrixes, the modulation of rare ^{13}C nuclei from the molecule and from the matrix is relatively weak [17]. Furthermore, the results in this literature show that the magnetic nuclei in the matrix have stronger modulation effects than the magnetic nuclei in the molecule [17]. In this case, this 1.1 MHz modulation is possible because of the difference of nuclear frequencies (ω_{-}) of ^{2}H in the matrix.

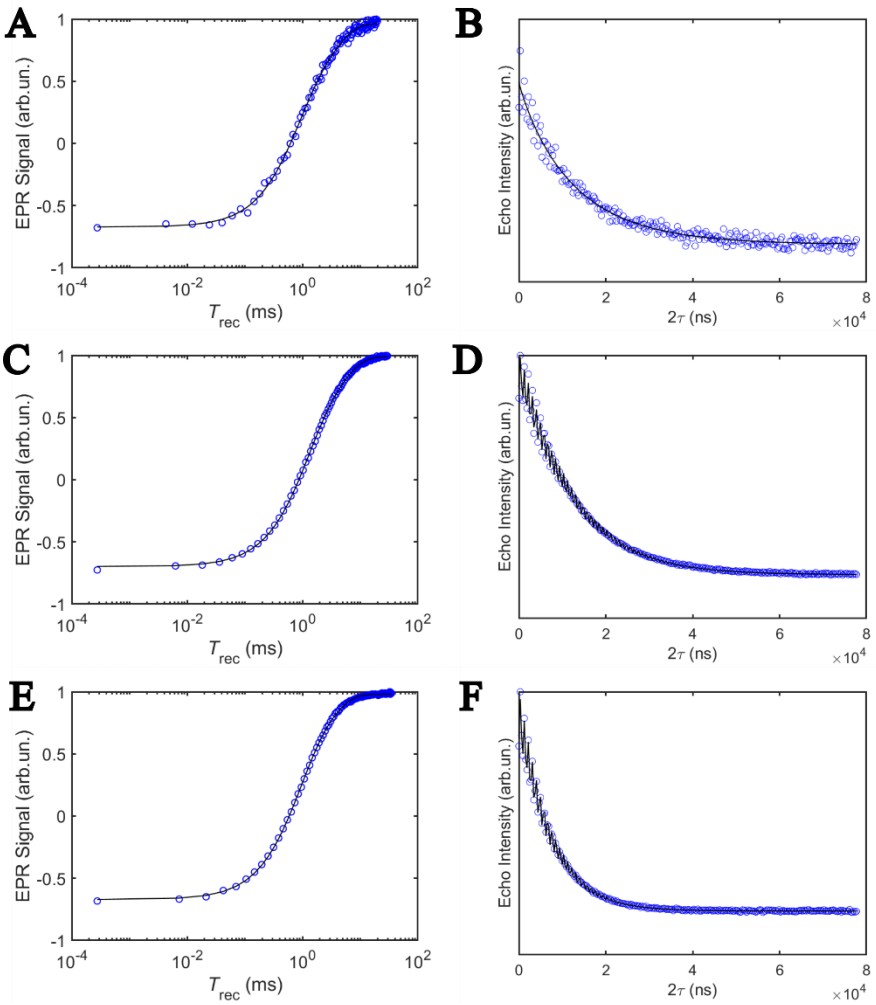

Figure 4.9 The inversion recovery and Hahn echo time traces of molecules 1 (A and B), 2 (C and D), and 3 (E and F) at 80 K at X-band, respectively.

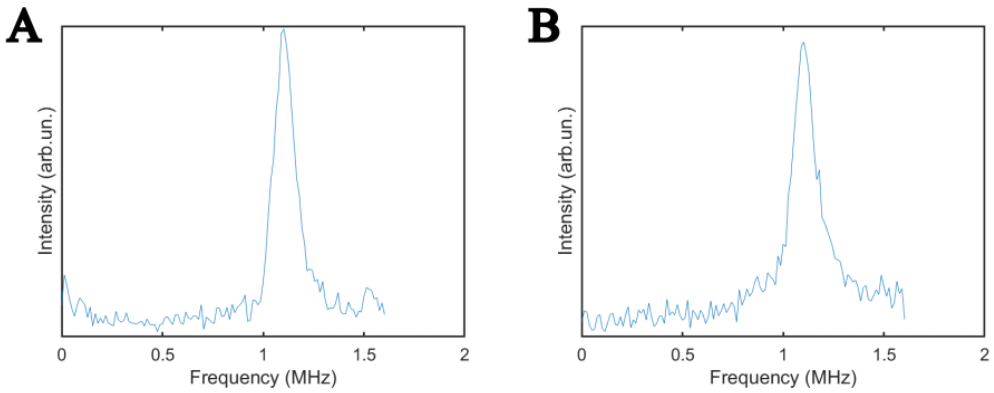

Figure 4.10 The fast Fourier transform results of the Hahn echo time traces of molecules 2 and 3.

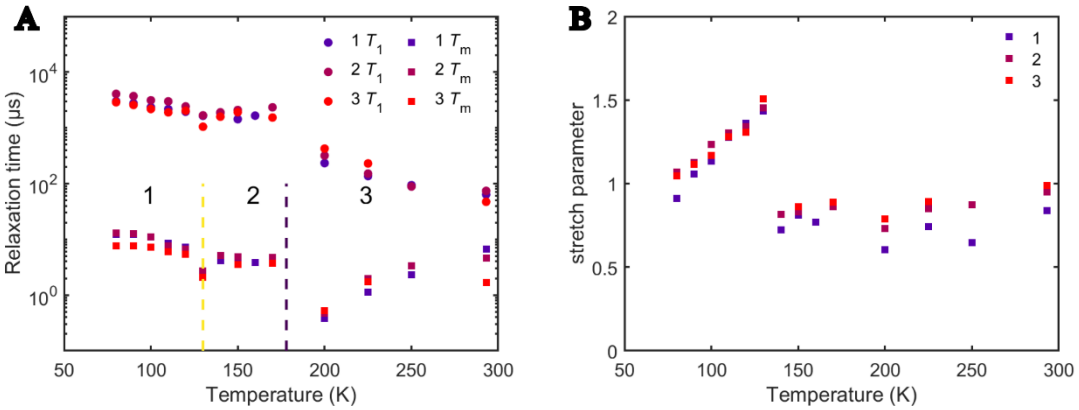

Figure 4.11 (A) The relaxation time T_1 (circle symbol) and T_m (square symbol) of molecules 1, 2, and 3, respectively, at different temperatures. (B) The stretch parameter was extracted from Hahn echo time traces of molecules 1, 2, and 3.

Figure 4.11 (A) shows the temperature dependence of T_1 and T_m from 80 K to room temperature. The temperature range can be divided into three regions as shown in Figure 4.11. In the first and second regions, the coherence time is subject to the intramolecular motions. In the first region, namely from 80 K to 130 K, the coherence time of three molecules has a decreasing trend and reach a minimum value at 130 K. This is common because of the increasing magnetic noise felt by the unpaired electron, such as the accelerated rotation of the methyl group of d8-toluene and the molecule itself. In the second

region, specifically, from 130 K to 178 K (the melting point of the d8-toluene), the coherence time increases. Such a trend with a minimum at the temperature of 130 K is still because of intramolecular methyl group rotations facilitated by the softening of the matrix. The hyperfine couplings of different protons in the methyl group are usually different, and the rotation of the methyl group leads to the interchange of the position of these protons and thus to magnetic fluctuations around unpaired electrons. The hyperfine coupling difference between proton *i* and proton *j* is given by:

$$\Delta A = \sqrt{(A_i^x - A_j^x)^2 + (A_i^y - A_j^y)^2 + (A_i^z - A_j^z)^2}. \quad (4.4)$$

According to DFT results, average hyperfine coupling difference is $\overline{\Delta A}$ = 1.2 ± 0.6 MHz. The rotation rate of methyl group τ_R has an exponential relationship with the temperature

$$\tau_R = \tau_{R,0} e^{E_a/k_B T}. \quad (4.5)$$

Here $\tau_{R,0}$ is a pre-exponential factor, which defines the rotation rate at infinite high temperature, E_a is the energy barrier, and T is the temperature. At 130 K, $\overline{\Delta A}$ is similar to the rotation rate of methyl groups. Therefore, the decoherence effect originating from methyl group rotations is at the maximum, and the coherence time is at its minimum. Hence, we find ${\tau_R}^{-1} = 2\pi\overline{\Delta A}$. If we further assume $\tau_{R,0} \sim 10^{-12}$ s[17], we obtain the energy barrier E_a 31477 GHz (3.0 kcal/mol), which is similar to results in literature[99,100]. However, the rotation rate increases when the temperature increases, and eventually becomes larger than $\overline{\Delta A}$. Therefore, this decoherence effect becomes less effective and coherence time increases as the temperature increases, as shown in Figure 4.11 (A). Similar results have been reported in nitroxides and open-shell graphenoids with two five-membered-ring defects[57,85].

In the third region, that is from 178 K to 293 K, the coherence time increases as the temperature increases. The melting point of solvent-d8-toluene is 178 K. Therefore, at this high-temperature range, the sample is in the tumbling limited regime. At the first temperature (200 K) above the melting point, the tumbling rate ($1/\tau_C$) reaches a value similar

or larger than the spin precession rate (ω_S). As the temperature increases, the tumbling rate becomes much larger than the spin precession rate, the decoherence effect becomes less effective. Hence, the coherence time increases again. The temperature-dependence of the stretch parameter is shown in Figure 4.11 (B). The stretch parameters are close to 1 in the temperature range of measurement.

The spin-lattice relaxation time decreases monotonically across the measurement temperature range because of increased phone modes. From 80 K to 178 K (the melting temperature of the solvent), the dominating relaxation mechanism is Raman process. When the temperature is above the melting point of d8-toluene, the dominating relaxation mechanism is molecular tumbling including spin-rotation (sr) interaction, electron–nuclear dipolar (end) interaction and spin diffusion (sd)[101,102]. The spin–lattice-relaxation rate follows the following relationship[101]

$$\frac{1}{T_1} = \frac{1}{T_1^{\mathrm{sr}}} + \frac{1}{T_1^{\mathrm{end}}} + \frac{1}{T_1^{\mathrm{sd}}}\,. \tag{4.6}$$

The spin-rotation term means the molecule's rotation directly leads to the relaxation of the electron spin through the modulation of the *g*-anisotropy. The electron–nuclear dipolar term is the relaxation process because of the interaction between the magnetic nuclei in the molecule and the unpaired electron through the modulation of anisotropic hyperfine coupling. The spin-diffusion term refers to the interaction between the unpaired electron and the magnetic nuclei in the solvent (^{2}H) that leads to relaxation.

Figure 4.12 shows the Rabi oscillation results of molecule 1. The black line denotes the Rabi frequency, and the green line denotes the Larmor frequency of the ^{1}H nuclei. The Rabi frequencies have a linear relationship with the power of the microwave pulse. Therefore, the frequency of the significant peak is not an artefact, and we can initialise the spin to any arbitrary state by using a microwave pulse. However, an additional small peak appears at 14.9 MHz, which is the Larmor frequency of ^{1}H in the molecule's periphery. This

result further shows the strong influence of the hyperfine coupling of the ^{1}H nuclei in this structure.

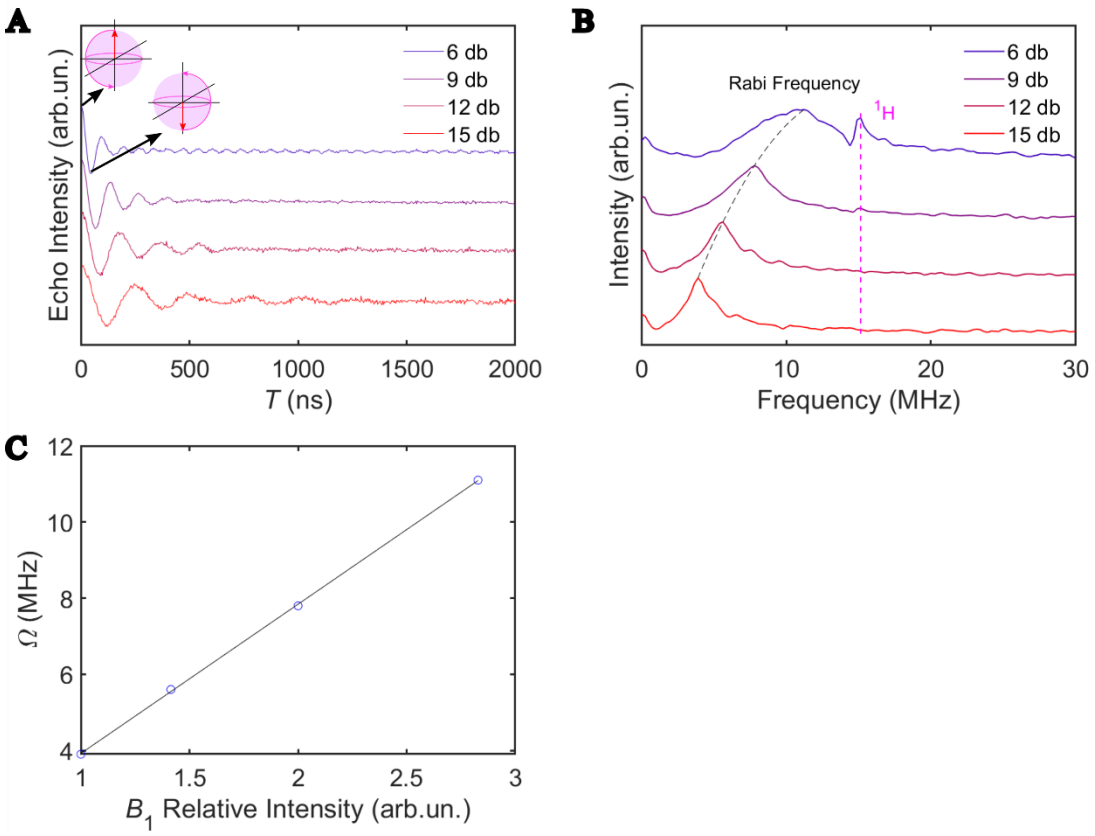

Figure 4.12 Rabi oscillations of molecule 1 in a d8-toluene solution at 80 K with different power attenuations (A), Fast Fourier transformation results of Rabi oscillations (B), and the linear relationship between Rabi frequency and the relative strength of the microwave pulse (C).

4.4 Summary

In this project, we investigated the magnetic and coherence properties of a family of benzo-extended cyclohepta[def]fluorene, which has a five-membered ring and a seven-membered ring, with two unpaired electrons. The CW-EPR spectra of powders confirm the open-shell character of these molecules as predicted in Clar's rule and Lieb's theorem. Furthermore, variable temperature EPR spectra of powders were performed to investigate the relationship

between molecular structure and isotropic exchange coupling by fitting the Bleaney–Bowers equation. χT shows an increasing trend as the temperature increases in all these molecules, which indicates the existence of a singlet ground state, which is EPR silent, and an additional thermally excited paramagnetic state, which is a triplet state here. The singlet–triplet energy gaps are 493 GHz, 210 GHz, and 199 GHz for molecules 1, 2, and 3, respectively. This result shows the unpaired electrons in these molecules are strongly coupled, since the *J* coupling is much larger than the energy of the microwave at X-band (9.7 GHz). Thus, there is no significant mixture between the singlet and triplet states. Furthermore, it is better to use the coupled representation to describe these spin systems. Additionally, as the size of the molecule increases, especially the conjugation backbone of the molecule, spin densities of both unpaired electrons further spread to the added benzene rings, and the overlap between the unpaired electrons decreases, leading to a smaller *J* coupling. In our case, the singlet–triplet energy gap is much smaller than the two five-membered rings graphenoids, which are at the order of magnitude of 10000 GHz[85]. Such a low singlet–triplet energy gap gives us new insights into creating new organic molecules with a high spin ground state.

Then, CW spectra in the d8-toluene solution samples were measured to investigate the spin interactions within the spin system further, since in the CW powder spectra, some splittings are suppressed by the strong intermolecular dipolar couplings. In the CW solution spectra, more splittings appear because of hyperfine couplings of ^{1}H nuclei at the periphery of the molecules. The *g*-factor is relatively close to the value of the free electron (2.0023), as we can see from the fit results, since the spin–orbit coupling is very weak in these molecules. According to DFT calculations, some hyperfine couplings of the ^{1}H nuclei are relatively large, at the order of magnitude of several MHz. Some are relatively small, less than 1 MHz. However, we are not sure about the hyperfine couplings of ^{1}H nuclei that can show splittings in the CW solution spectra, are unresolved, and are incorporated into the

linewidth of the spectra. Therefore, to perform the fits, we fit the spectra with one ^{1}H nucleus first and then sequentially added ^{1}H nuclei until all splittings in the spectrum could be fit well. We found that eight ^{1}H nuclei fit spectra best for all three molecules. The fit hyperfine couplings are on the order of several MHz. There is no zero-field splitting in solution spectra at 4 K and room temperature. It means that these two unpaired electrons are so delocalised in the conjugation backbone and their wave functions have a large overlap that a point dipole approximation is invalid in this case. The spin interactions in these molecules were figured out thoroughly.

Finally, we investigated the coherence properties of these molecules. A defect in graphenoids with a five-membered ring and a seven-membered ring is a brand-new strategy to generate unpaired electrons in polycyclic aromatic hydrocarbons. It can be used as a qubit for quantum information processing. In order to achieve molecular-based quantum information science, we need to satisfy five criteria, such as a long coherence time much longer than the gate operation time [103,104]. Hence, we investigated the coherence time and spin–lattice-relaxation time here. The coherence times of three molecules at temperatures ranging from 80 K to 293 K were measured. From 80 K to 178 K, the coherence time is dictated by molecular motions, especially the methyl group rotations in the molecules and in the solvent. At 80 K, the rotation rate is smaller than hyperfine coupling difference of the ^{1}H nuclei in the methyl group of the molecules, and as temperature increases, the rotation rate gradually exceeds the hyperfine coupling difference. When at 130 K, the rotation rate is similar to the hyperfine coupling difference, the decoherence because of the rotations of methyl groups is at its maximum and therefore coherence time has a minimum value at 130 K. When temperature is above the melting temperature of the solvent (178 K), coherence time in dependent on the molecular tumbling. At the first temperature (200 K) above the melting point, the tumbling rate ($1/\tau_C$) is at least similar to the spin precession rate

(ω_S). When the temperature increases, the tumbling rate becomes larger than spin-precession rate (ω_S). Thus, the decoherence resulting from molecular tumbling becomes less effective and coherence time increases. The coherence time reaches 10 to 12 microseconds at 80 K and 2 to 6 microseconds at room temperature, which is sizable. However, such a value is still below 100 microseconds, a typical value that enables a qubit to complete 10^4–10^5 quantum operations before the qubit loses coherence [2]. The spin–lattice-relaxation time was investigated. From 80 K to 178 K, the dominating relaxation mechanism is the Raman process. From 178 K to room temperature, tumbling process dominates the spin–lattice relaxation. Across the whole measurement temperature range, the spin–lattice-relaxation time is significantly larger than the coherence time. Therefore, it is not an effective decoherence channel that constrains the coherence time in our project. In order to initialise a molecular-based electron-spin qubit to an arbitrary state, Rabi oscillations were performed. As the microwave power increases, the Rabi frequencies increase linearly, which confirms that the prominent peak is not a cavity defect. However, there is an additional small peak in the FFT results of the Rabi oscillations, which is fixed at 14.9 MHz. Such a peak stems from hyperfine coupling with the ^{1}H nuclei, which further confirms the significance of ^{1}H's effect on the edges of the molecule.

4.5 Project Overview

We carried out this project in collaboration with Prof Xinliang Feng's group at Technische Universitat Dresden. The molecules were synthesised by Fupeng Wu under the supervision of Dr Ji Ma. The measurement of the magnetic properties and of the Rabi oscillations were done by Zhijie Huang. The relaxation times were measured by Dr Federico Lombardi. The DFT calculations were performed by Zhijie Huang. All the analyses were performed by Zhijie Huang.

5. Helical open-shell polycyclic aromatic hydrocarbons

5.1 Introduction

Helical open-shell polycyclic aromatic hydrocarbons are a new type of interesting organic molecule with fascinating magnetic and electronic properties [36,105]. They have promising organic electronic and organic magnetic applications [105]. The intrinsic high reactivity makes them challenging to synthesise and isolate. However, thanks to the advancement of the synthesis method, a new type of open-shell, polycyclic aromatic hydrocarbon (PAH) with two five-membered rings has been synthesised [85]. This makes the investigation of their magnetic and quantum properties possible. Compared with the graphenoids reported in Chapter 4, each containing a five-membered ring and a seven-membered ring, polycyclic aromatic hydrocarbons with two five-membered rings are a new type of graphenoid, and the relationship between their structures and properties is waiting to be investigated. This project investigates spin interactions within these molecules, and the relationship between the molecular structure and relaxation properties within this family of molecules.

Figure 5.1 shows the chemical structures of three molecules. According to Clar's rule, there are two unpaired electrons in all these three molecules' most stable resonance structures. These electrons reside in the C atoms of the five-membered rings that connect to the mesitylene group. In this chapter, the spin interactions within these molecules were explored by analysing these molecules' CW-EPR powder and solution spectra. Furthermore, the ORCA quantum-chemistry software was used to investigate the spin-density distribution and EPR-relevant parameters to understand the experimental results. Finally, the quantum property of these molecules was investigated to assess their potential as molecular qubits for quantum-information processing.

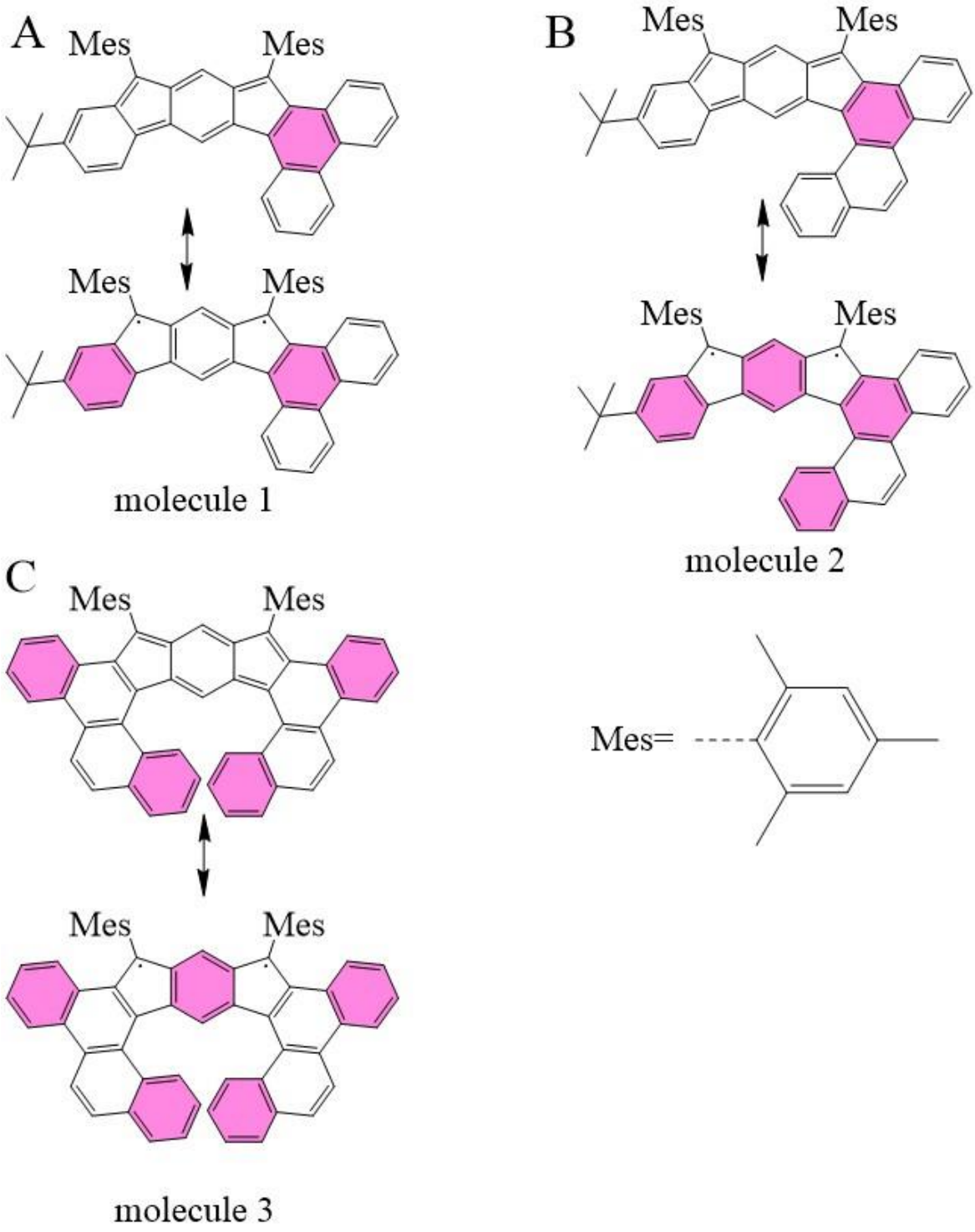

Figure 5.1 The chemical structures of molecules 1 (A), 2 (B), and 3 (C). Mes represents the mesitylene group. The pink rings represent sextet structures. Defects with two disjoint five-membered rings are introduced in these three molecules.

5.2 Magnetic properties

We first measured CW solution spectra to determine the spin interactions within these molecules. The CW d8-toluene solution spectra of molecules 1 and 3 are shown in Figure 5.2. As discussed in Chapter 4, the spin Hamiltonian can be reduced to such a formula:

$$\widehat{H} = \mu_B B \boldsymbol{g} \hat{S} + \sum_{i=1}^{n} \hat{S} \boldsymbol{A} \hat{I}^i \tag{5.1}$$

Since molecule 2 in Figure 5.1 already has been reported in other literature [85], only the CW spectra of the other two molecules were measured.

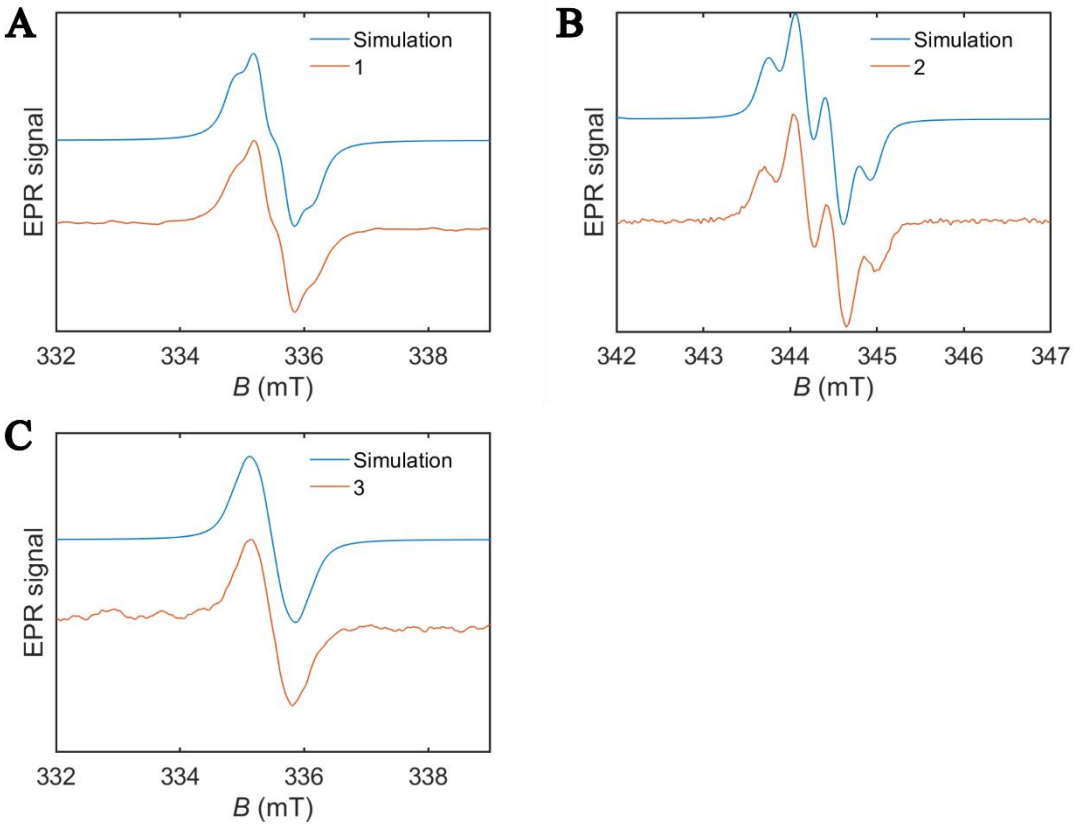

Figure 5.2 CW solution spectra of 1 (A), 2 (B), and 3 (C), and their corresponding simulations at room temperature.

As we can see from the CW solution spectra shown in Figure 5.2, there are some transitions because of hyperfine couplings with H nuclei in the spectrum of molecule 1. However, in the spectrum of molecule 3, such transitions are not visible. Furthermore, as shown in Figure 5.3, we can see that molecule 1 has stronger hyperfine couplings and a broader spectrum. This can be explained by the smaller molecular size, which leads to more concentrated unpaired electrons within the conjugation backbone of the molecules. Therefore, more unpaired electrons have a larger possibility to locate at H nuclei at the periphery of the molecule, and these nuclei have larger isotropic hyperfine couplings.

The fit results are shown in Table 5.1. The fit considers the g factor, isotropic hyperfine couplings of H nuclei and linewidth. For liquid solutions in fast-motional regime, molecular tumbling leads to averaging the anisotropy of g-factor and hyperfine couplings. The spectra were used Easyspin function garlic to perform the fitting. The isotropic g-factor is 2.0023, which is consistent with other literature[17] because of the weak spin–orbit coupling in open-shell polycyclic aromatic hydrocarbons. The isotropic hyperfine couplings from H nuclei are tiny, almost all of them are smaller than 10 MHz in molecules 1 and 3. The hyperfine couplings from other remaining H nuclei in these molecules are not distinguished in the CW solution spectra and only contribute to the broadening of the linewidth.

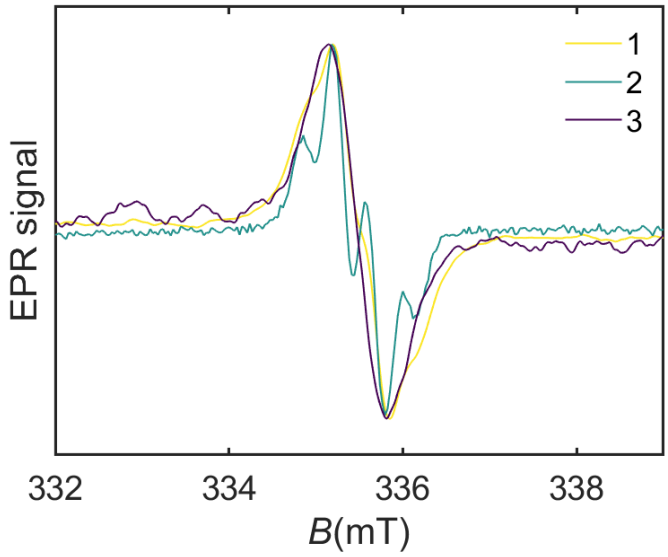

Figure 5.3 The comparison of the CW d8-toluene solution spectra of molecules 1 and 3 at room temperature at X-band.

Table 5.1 EPR parameters from fitting the CW d8-toluene solution spectra at room temperature.

Parameters	**1**	**2**	**3**
S	1	1	1
g	2.0022	2.0066	2.0023
A_1 (MHz)	10.37	10.03	–
A_2 (MHz)	8.97	9.84	–
A_3 (MHz)	8.13	9.89	–
lw_{Gauss} (mT)	0.18	0.23	0.37
lw_{Lor} (mT)	0.25	0.11	0.43

To confirm our analysis, ORCA quantum-chemistry software was used to calculate spin-density distributions and EPR-relevant parameters. Figure 5.4 shows spin-density distributions in these three molecules. Unpaired electrons have the largest distribution at the junction of the five-membered ring and the mesitylene group, and are spread across the whole conjugation backbone of the molecule. As shown in Figure 5.5, the theoretical results of molecules 1 and 3 are consistent with the experimental results, except that the theoretical results do not show the transitions shown in the shoulders. Table 5.2 shows the calculated isotropic hyperfine couplings of the H nuclei at the periphery of the π-conjugated structure. These calculated results are consistent with the values obtained from fitting the experimental results. Furthermore, we can conclude that the isotropic hyperfine couplings below around 3.5 MHz cannot be resolved and can be incorporated in the linewidth of the spectra. The resolved hyperfine couplings by fitting corresponds to some of the largest hyperfine couplings calculation results, which are shown in bold texts in Table 5.2.

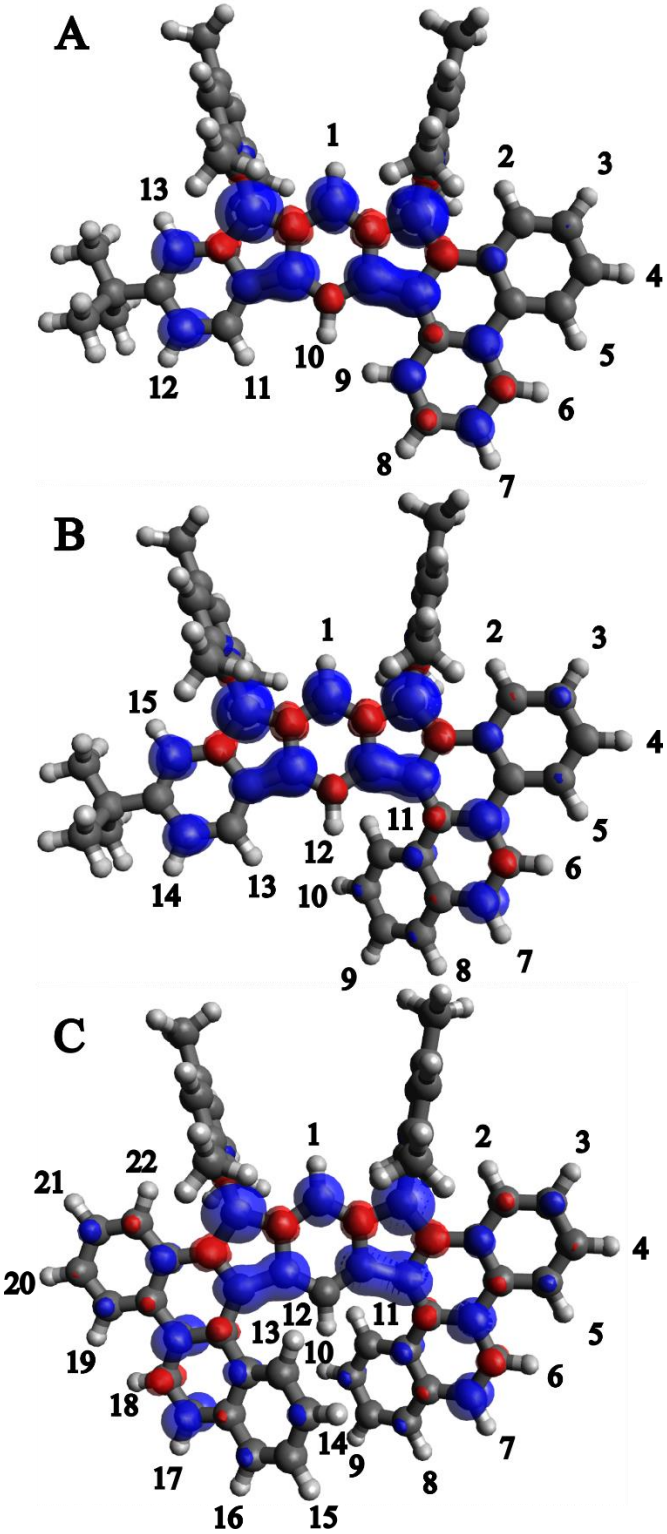

Figure 5.4 The calculated spin densities of molecules 1 (A), 2 (B), and 3 (C) in the triplet state with an iso value of 0.002. The functional is B3LYP/G, and the basis set is EPR-II. The red colour represents negative spin densities, and the blue colour represents positive spin densities.

Table 5.2 EPR calculation results of molecules 1, 2, and 3, showing the *g*-factor and isotropic hyperfine couplings. The positive isotropic values mean that the electron and nuclear spins are parallel. Similarly, negative isotropic values mean the electron and nuclear are antiparallel.

Parameters	**1**	**2**	**3**
g	2.0025	2.0025	2.0025
A_1 (MHz)	**-10.1396**	**-10.1402**	-8.7508
A_2 (MHz)	0.4280	0.6474	0.9173
A_3 (MHz)	-0.6725	-0.7683	-1.2655
A_4 (MHz)	0.1722	0.3630	0.6741
A_5 (MHz)	-0.4826	-0.7961	-1.0024
A_6 (MHz)	1.1922	1.3914	-1.5501
A_7 (MHz)	-2.8529	**-3.5415**	-3.9141
A_8 (MHz)	0.9559	-0.7683	-0.8972
A_9 (MHz)	-2.3271	0.4258	0.5114
A_{10} (MHz)	1.5571	-0.8163	-0.9337
A_{11} (MHz)	-0.3982	0.3630	0.6022
A_{12} (MHz)	**-4.7263**	1.7111	0.4818
A_{13} (MHz)	**-4.3719**	-0.3013	0.6035
A_{14} (MHz)	–	-0.4012	-0.9327
A_{15} (MHz)	–	**-4.7009**	0.5111
A_{16} (MHz)	–	–	-0.8978
A_{17} (MHz)	–	–	-3.9066
A_{18} (MHz)	–	–	1.5484
A_{19} (MHz)	–	–	-0.9983
A_{20} (MHz)	–	–	0.6703
A_{21} (MHz)	–	–	-1.2627
A_{22} (MHz)	–	–	0.9144
lw_{Gauss} (mT)	0.16	–	0.08
lw_{Lor} (mT)	0.31	–	0.34

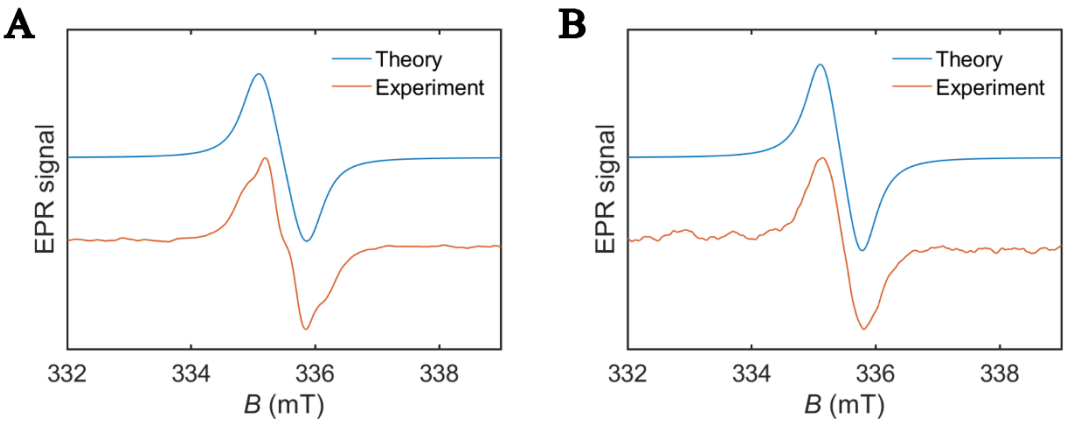

Figure 5.5 The comparison of the CW spectra of molecules 1 (A) and 3 (B) obtained from theory and experiment, respectively.

5.3 Coherence properties

The coherence properties of these open-shell PAHs are very important for us to explore their applications in quantum information processing. A long coherence time is one of the requirements to achieve molecular spin qubit[106]. The relevant theory can be found in the monograph[107]. To explore the unknown coherence properties of these molecules, an echo detected field-swept (EDFS) EPR spectrum was first measured. Therefore, we can know that the echo peak position is around 346.8 mT at X-band frequency, and keep the magnetic field fixed at this value to get high signal-to-noise ratio time traces of Hahn echo and inversion recovery. Figure 5.6 shows the EDFS spectrum, time traces of Hahn echo and inversion recovery with their corresponding fitting lines, and fast Fourier transformation results of the Hahn echo decay of molecule 1 in d8-toluene solution at 10 K at X-band frequency. The Hahn echo decay shows some modulations from the environment. There are two peaks in the fast Fourier transformation results at 7.41 MHz and 14.73 MHz. The 14.73 MHz corresponds to the Larmor frequency of the ^{1}H nucleus at X band. The 7.41 MHz could be the sum peak of the ^{13}C nucleus ($2\nu^{13}$C).

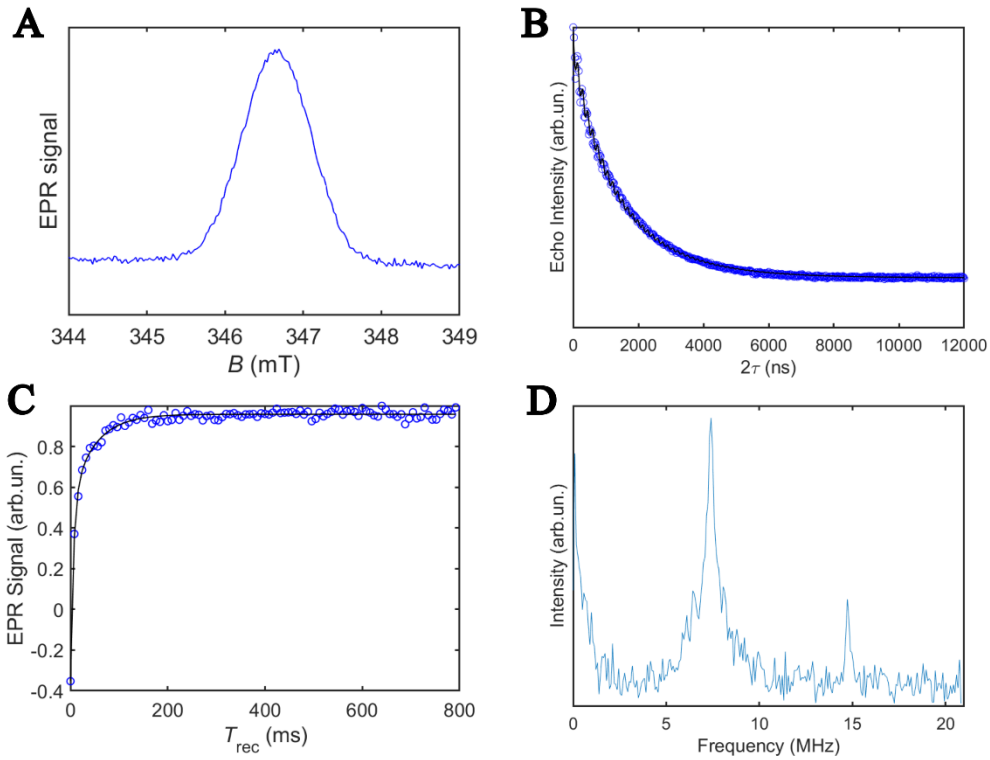

Figure 5.6 The EDFS spectrum (A), the time trace of Hahn echo (B), the time trace of inversion recovery (C), and fast Fourier transformation results of a Hahn echo decay (D) of molecule 1 in d8-toluene solution at 10 K at X-band.

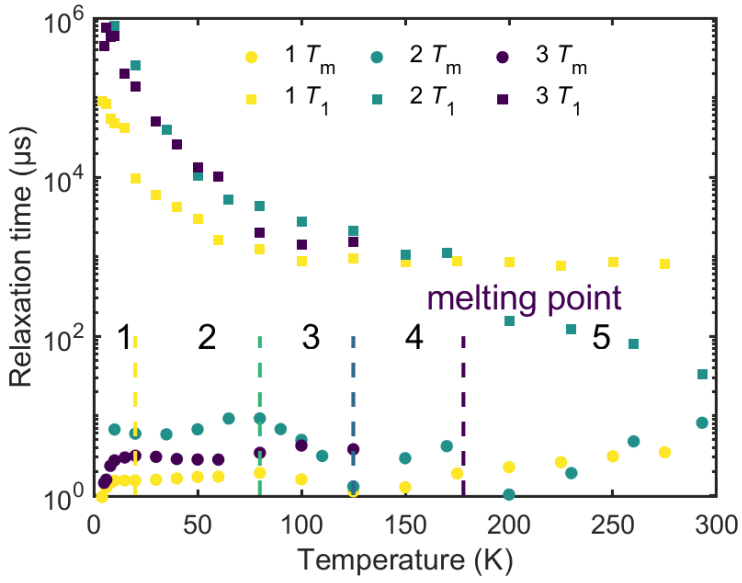

Figure 5.7 The temperature dependence of T_1 and T_m of these three molecules. The trend of coherence time vs. temperature can be divided into five regions.

Figure 5.7 shows the temperature dependence of T_1 and T_m of molecules 1 and 3. The spin–lattice-relaxation time depends on the temperature significantly and shows a decreasing trend as the temperature increases. The spin–lattice relaxation mechanisms will be discussed in depth later in Figure 5.8. The coherence time corresponds to the time at which the signal reduces to the 1/e of its initial magnitude. In terms of the theoretical work on the coherence time, recent research has successfully used the molecular structure to predict the coherence time at low temperatures based on a nuclear-spin-driven decoherence channel in nitroxide radicals [108]. In our project, the temperature dependence of coherence time was divided into 5 regions according to the different mechanisms. For the first region, namely, from 4 K to 20 K, the coherence time gradually increases with a peak at 20 K. We attribute this to the quantum rotation of the methyl group in the molecule and in the solvent. The quantum rotation of the methyl group can invert the nuclear spin state and therefore enhance the spin diffusion rate. The frequency of such a rotation is temperature dependent, which has been reported in a Mn(II)-doped hybrid perovskite [63,109] and other materials [86,88,110].The tunnel frequency decreases as the temperature increases [63], so the quantum rotation effect becomes less effective in leading to decoherence as the temperature increases. In the second region, that is from 20 K to 80 K, the coherence time becomes stable and independent of temperature. The reason is that in this temperature range, the decoherence is dictated by nuclear spin flip-flops and is not sensitive to the temperature [100]. In the third region, specifically, from 80 K to 120 K, the coherence time decreases and reaches a minimum in 120 K. In the fourth region, namely, from 120 K to 178 K (the melting point of d8-toluene), the coherence time increases again. This is because in the temperature range, from 80 K to 178 K, the rotation rate of the methyl group follows [57,100,111]:

$$\tau_R^{-1} = \tau_{R,0}^{-1} e^{-E_a/k_B T}. \quad (5.1)$$

Where τ_R^{-1} is the pre-exponential factor, representing the rotation rate at infinitely high temperature, E_a is the energy barrier height. When the rotation frequency approaches the hyperfine coupling difference of the ^{1}H nuclei in the methyl group, the rotation rate maximises decoherence. The hyperfine coupling difference can be obtained from DFT calculations and has such a formula:

$$\Delta A = \sqrt{(A_i^x - A_j^x)^2 + (A_i^y - A_j^y)^2 + (A_i^z - A_j^z)^2}. \quad (5.2)$$

The *i* and *j* are the indexes of the ^{1}H nuclei of in the methyl group. We got the average hyperfine coupling difference ($\overline{\Delta A}$) from DFT results for all methyl groups in the molecule, which is 1.3 ± 0.65 MHz. Since at 125 K, the coherence time has a minimum value. Therefore, we have $\tau_R^{-1} = 2\pi\overline{\Delta A}$ at 125 K. Assuming that $\tau_{R,0}$ is 10^{-12} s [17], we got the energy barrier is 2.9 kcal/mol, which is comparable with the result reported in previous literature [57]. Therefore, the third region is a slow-motion region and the fourth region is a fast-motion region. In the fifth region, that is from 178 K to room temperature, the coherence time is determined by the tumbling correlation time of the molecule. According to the increasing trend of the coherence time in this tumbling region, the tumbling rate τ_C is similar to the spin-precession rate ω_S at 200 K and then becomes larger than the spin-precession rate as the temperature increases. Therefore, the decoherence effect becomes smaller, and the coherence time shows an increasing trend. The coherence time displays a relatively large value of 3 μs at room temperature, although it is still below the general goal of 100 μs [2]. In summary, within the temperature range of measurement, methyl groups have a large influence on the coherence time, which is consistent with the results of nitroxyl radicals [112]. The spin–lattice-relaxation time is at least two orders of magnitude larger than the coherence time. Thus, the spin–lattice-relaxation time is not the main limitation of the coherence time here.

Figure 5.8 shows a fit to the temperature dependence of the spin–lattice-relaxation time, and an analysis of the involved mechanisms. In both 1 and 3, the direct process dominates the spin–lattice relaxation at the temperature range between 4 K and around 30 K. From 30 K to 178 K (the melting point of d8-toluene), the effect of the Raman process gradually exceeds the direct process and dominates the spin–lattice relaxation. Finally, above the melting temperature of d8-toluene, the spin–lattice-relaxation process is dictated by tumbling of the molecules. The fitting formula is as follows:

$$\frac{1}{T_1} = A_{\mathrm{Dir}} T + A_{\mathrm{Ram}} \left(\frac{T}{\theta_{\mathrm{D}}}\right)^9 \int_0^{\frac{\theta_{\mathrm{D}}}{T}} x^8 \frac{\mathrm{e}^x}{(\mathrm{e}^x - 1)^2} \mathrm{d}x. \tag{5.3}$$

The parameters involved in this equation can be found in chapter 2. All the spin–lattice-relaxation fitting parameters for molecules 1 and 3 are displayed in table 5.3.

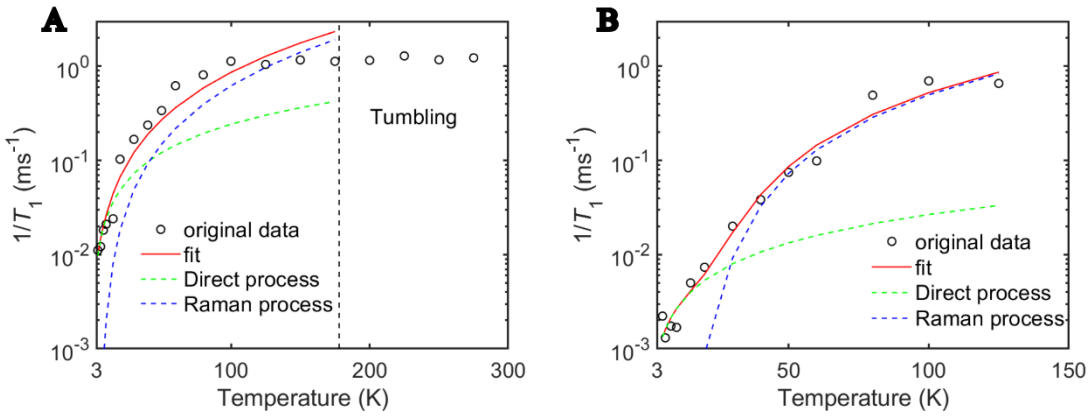

Figure 5.8 Analysis of different spin–lattice-relaxation mechanisms across the whole temperature range of measurement of molecule 1 (A) and 3 (B) in d8-toluene solution at X-band frequency. The vertical black dashed line of 178 K corresponds to the melting temperature of the d8-toluene.

Table 5.3 All the spin–lattice-relaxation fitting parameters for molecules 1 and 3.

molecule	1	3
A_{lin}**(s^{-1})**	2.4	0.3
A_{Ram}**(s^{-1})**	9.19×10^4	1.31×10^4
θ_D**(K)**	45.6	176.0

5.4 Summary

In this project, we explored the magnetic and quantum properties of open-shell graphenoids with two five-membered rings. The CW spectra of these molecules confirm the open-shell character as predicted by Lieb's theorem and Clar's rule. To analyse the spin interactions within the molecule, we used the Easyspin garlic function to fit the d8-toluene solution spectra. The fit results show that the *g*-factor is 2.0025, close to the free electron's, in molecules 1 and 3, since the spin–orbit coupling is small in graphenoids. Furthermore, we showed that in molecule 1, additional transitions appear because of hyperfine couplings with hydrogen nuclei located at the periphery of the molecule. However, in molecule 3, no such significant transitions appear, and all hyperfine couplings with hydrogen nuclei are incorporated into the linewidth. DFT calculations confirmed our experimental results, such as the *g*-factor and hyperfine couplings. Furthermore, the DFT calculation results were used to get the CW spectra directly, which is consistent with the experimental CW spectra. The spin density has the largest value at the junctions of the five-membered ring and the mesitylene groups. The spin density spreads across the whole conjugation structure from these two junctions. Since a larger molecular size leads to a smaller spin density at the

hydrogen nuclei at the periphery of the molecule, the isotropic hyperfine couplings with these hydrogen nuclei becomes smaller. Thus, the larger molecule has a narrower solution spectrum.

To explore their applications in quantum information processing, we investigated coherence properties of these molecules. The spin–lattice relaxation time was measured from 4 K to room temperature. The dominating spin–lattice relaxation mechanisms from low temperature to high temperature are the direct process, Raman process and molecular tumbling in this order. The coherence time was also measured, and corresponding mechanisms were analysed thoroughly. Across the whole temperature range, the spin–lattice relaxation time is at least two orders of magnitude larger than coherence time, therefore, the spin–lattice relaxation time is not the main limitation of coherence time in our project. At low temperatures, from 4 to 20 K, the quantum rotation of the methyl group of the molecule and that of solvent dominates the decoherence, and the coherence time shows an increasing trend. From 20 K to 80 K, the nuclear spin flip-flop dictates the coherence time, and remains constant. From 80 to 178 K, the classical rotation of the methyl group dominates the decoherence process, and its effect is determined by the relative strength between the hyperfine coupling difference of the hydrogen nuclei in the methyl group and the rotation frequency defined by the Arrhenius equation. So, the coherence time reaches a minimum when the rotation frequency approaches the hyperfine coupling difference at 120 K. At high temperatures, from 178 K to room temperature, the coherence time is determined by the tumbling process of the molecule. At the first temperature above the melting point (200 K), the tumbling rate is similar to or larger than the spin-precession rate. Above 200 K, the tumbling rate becomes larger than the spin-precession rate; therefore, the decoherence channel is suppressed, and the coherence time increases.

5.5 Project Overview

We conducted this project in cooperation with Prof Xinliang Feng's group at Technische Universität Dresden. Dr Ji Ma synthesised the molecules. The measurement of magnetic and quantum properties of molecule 1 and 3was performed by Zhijie Huang. The results of molecule 2 were obtained from Lombardi's thesis for comparison. DFT calculations were performed by Zhijie Huang. All analyses were carried out by Zhijie Huang.

6. Conclusions and perspectives

In this thesis, we used electron paramagnetic resonance (EPR) spectroscopy to investigate the magnetic and coherence properties of vanadyl porphyrin dimers and graphenoids.

In vanadyl porphyrin dimers, according to the strength of exchange coupling, we used uncoupled and coupled spin basis to describe the spin systems of these molecules, respectively. The triply linked dimers, including *anti*-dimer and *syn*-dimer, have very large isotropic exchange couplings, which are 899 MHz and 809, respectively. The isotropic exchange couplings are larger than the hyperfine coupling (477 MHz) and anisotropic Zeeman energy ($\Delta g\mu_B B$ = 420 MHz), and therefore there is no strong mixing between singlet and triplet states. Furthermore, in the strong exchange region, the dipolar coupling is manifested as a zero-field-splitting (ZFS) and the hyperfine coupling is halved compared with the monomer. The noncoincidence effects play an important role in the CW spectra. Since all the principal values are given in their own tensor frames, we need to set tensor frames for all these tensors and align them into the same molecular frame. Hence, for each molecule, we established tensor frames according to their molecular structures and used rotation matrices to align them. For other dimers, they are in the weak exchange coupling region because of smaller exchange couplings and are best described by uncoupled spin basis. As the distance between the two unpaired electrons increases, the isotropic exchange coupling decreases exponentially. The spin density distributions and other EPR-relevant parameters were calculated using ORCA. The majority of unpaired electron density distributes on the vanadyl ion and less distributes on the porphyrin ligand. The calculated hyperfine coupling of ^{51}V is consistent with the fitting results. The hyperfine couplings of N nuclei are small, and their isotropic hyperfine couplings are around 8.2 MHz. The hyperfine couplings of H nuclei are much smaller, and their isotropic exchange hyperfine couplings

are smaller than 1 MHz. Both of them do not manifest themselves in the CW spectra and only contribute to the linewidth. The calculated isotropic exchange coupling has a decreasing trend as the bridges of the dimers increase, which is consistent with experiment results. However, the calculating results tend to overestimate the isotropic exchange coupling in these vanadyl dimers. A Rabi oscillation experiment was done to confirm the total spin in the triply linked dimers, because the Rabi oscillation frequencies at the strongest peak of the standard sample (S = 1/2) and the dimer are different, and have a ratio of 1.24, approaching the theoretical value 1.42.

We studied the spin–lattice-relaxation mechanisms of these molecules and found that at low temperatures (from 4 K to 20 K), the direct process dominates the relaxation process and at relatively high temperatures (from 20 K to 80 K), the Raman process becomes the dominating relaxation mechanism. The coherence properties of vanadyl porphyrin dimers were also investigated, and we found that the side group and exchange coupling have a strong impact on them. The delocalised electrons in the dimeric structure can preserve coherence. The same vanadyl dimer structure with the tBu group shows a larger coherence time in all these dimers. Although the average distance between the H atom in tBu (-$C(CH_3)_3$) side group and the unpaired electron is smaller than that in THS (-$Si(C_6H_{13})_3$) side group according to their structures, the much more H atoms in the latter side group lead to much stronger decoherence and therefore lower coherence time. Furthermore, we found that the coherence time increases as the isotropic exchange coupling increases. The reason can be that the isotropic exchange coupling can suppress the magnetic noise, which has been reported in other systems, such as exchange-coupled spins in two Ti atoms [83]. The decoherence from instantaneous diffusion was about 2.4 % by extrapolating experiment, which indicates that intermolecular dipolar coupling is negligible. Rabi oscillations were

done to manipulate the spin states, which indicates they are promising to perform one- and two-qubit gate operations.

Defects in graphenoids can generate unpaired electrons in the structure, and therefore make graphenoids become paramagnetic molecules. The defect can be any non-six-membered rings, deviating from the normal unit of graphene, like five-membered rings or seven-membered rings. Through analysing the spin-density distributions, we found that the unpaired electron densities mainly distribute around the defects, and gradually extend to the other parts of π-conjugation structure, and with little on the side groups because of the negligible conjugation through the carbon–carbon single bond. In the graphenoids with neighbouring five- and seven-membered rings, we found that the exchange coupling between the two unpaired electrons is very large, at the order of hundreds of GHz. However, such a value is much smaller than that of graphenoid with two disjoint five-membered rings, which is at the order of tens of thousands of GHz. As more benzene rings are added to the conjugation structure, the isotropic exchange coupling of this series of graphenoids decreases. The reason is that more electron densities distribute to the additional benzene rings, and therefore the overlap of the two electrons' wavefunction becomes smaller. The dipolar coupling between the two spins is negligible, since we do not find any half-field transitions and additional energy transitions in CW spectra of powders. In the solution CW spectra, we found more energy transitions, which are because of the hyperfine couplings of H nuclei at the periphery of the molecules or from the side groups. These transitions are negligible in CW spectra of powders, because the intermolecular dipolar coupling is too strong in powders. The hyperfine couplings of these H nuclei were fitted, which are at the order of several MHz. Such a result is consistent with the DFT calculations. Many small hyperfine couplings, smaller than 1 MHz, only contribute to the line widths of spectra.

Furthermore, coherence properties were analysed. From 4 K to room temperature, the temperature dependence of coherence time can be divided into several regions according to the dominating decoherence mechanism. For example, in two disjoint five-membered rings, there are five different regions. The main decoherence mechanisms are quantum rotation of methyl groups in the molecules and solvent, flip-flop of nuclear spins, classical rotation of these methyl groups, and tumbling of molecules, respectively. The coherence properties can be understood from the molecular motions and nuclear magnetic noise. The coherence time of graphenoids with neighbouring five- and seven- membered rings can reach 10 μs, which is quite large. The spin–lattice relaxation time is also investigated. From 4 K to room temperature, the relaxation mechanisms are direct process, Raman process, and tumbling, respectively. The spin–lattice relaxation time is at least one order of magnitude larger than the coherence tome across the measurement of temperature range, so it is not a limiting factor of coherence time in our graphenoids.

Additional data

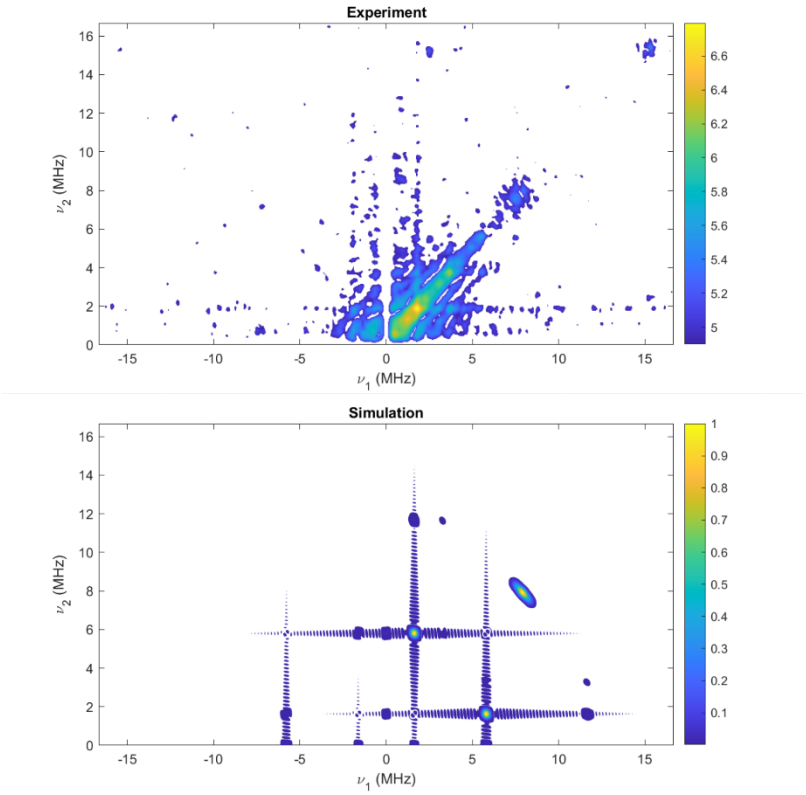

Figure A.0.1 HYSCORE experimental and simulation results of *syn*-dimer in d8-toluene at 20 K.

Since some hyperfine couplings are unresolved in CW-EPR, such as from ^{14}N, an HYSCORE experiment was done. Figure A.1 shows the experimental and simulation results of *syn*-dimer in d8-toluene at 20 K. According to the experimental results, we can know there are two hyperfine couplings, which are ^{14}N and ^{2}H. A_{iso} and T of ^{14}N are –4.15 MHz and –0.15 MHz, respectively. A_{iso} and T of ^{2}H are small and lower than 0.5 MHz. There are more peaks in the diagonal lines because of the incomplete interchange of nuclear spin coherence during the π-pulse.

Acknowledgements

First, I would like to thank my supervisor Dr Michael Slota for accepting me into the Nanospin Group to do all these exciting projects. He is a knowledgeable scientist exploring several fields, including nano-molecule synthesis, quantum transport, ab initio modelling, EPR and so on. He gave me a lot of help when I came across problems along the way in research. I am incredibly grateful for his support and for creating a warm environment in our group.

Moreover, I would like to thank Dr Ji Ma and Fupeng Wu from Technische Universität Dresden for providing me with the advanced graphenoids molecules and Iago from Oxford Chemistry for the novel porphyrins.

Also, I would like to thank Dr Will Myers, who gave me training on how to operate the EPR instrument and solved the problems of the instrument when it went wrong.

I acknowledge the important assistance from Ming-Yee for giving me comments and suggestions to improve my thesis.

I am grateful to all my group members: Dr Federico Lombardi for teaching me about the operation of CW EPR and some discussions about the molecules, Fanmiao Kong for insightful discussions about DFT modelling and recent EPR-relevant literature, Xuelin Yao for fruitful discussions about the synthesis and properties of graphenoids and GNRs, Alex, Dimitris, Alessandro, Hewen, Chen, Yongxiang, Karen and Matthew for beneficial scientific sharing and discussions and lively working bond in this group.

Finally, I would like to thank my parents and brother for their support and understanding during this period.

List of Figures

Figure 1.1 Schematic illustration of the Bloch sphere and a general pure quantum state (A) and the mixed quantum state of a decoherent ensemble (B). When the individual spins are in alignment, the spin state of the system is in a pure state and can be represented by a point on the surface of the Bloch sphere. However, if the individual spins are not in alignment, it is in a mixed state and can be represented by a point inside the Bloch sphere. 10

Figure 1.2 Schematic of four typical periphery structures of PAHs, including bay region, L-region, K-region, and cove-region. Figure adapted from Ref. [8]. 13

Figure 1.3 Chemical structure of the hexa-peri-benzocoronene (p-HBC) [8]. 13

Figure 1.4 Schematic diagram of the organisation of alkyl-substituted PAHs. First, monomers stack into columns through π-interaction. Then, columns group into a super-molecular organisation through nanophase separation. Figure adapted from Ref. [10]. 14

Figure 1.5 Chemical structure of the pentacene..... 15

Figure 1.6 Heptacene, Octacene, nonacene, decacene, and undecacene synthesised using on-surface methods. Figure adapted from Ref. [34]. 15

Figure 1.7 (a) The energy gap versus the number of benzene rings in a series of acenes with the fit results, blue line: exponential model, red line: inverse model. (b) The inversed number of rings versus the energy gap in a series of acenes with the fit results. Figure adapted from Ref. [34]. 16

Figure 1.8 Chemical structures of phenalene 1 and three aza derivatives 2–4. 2, 3, and 4 (4a and 4b) have a doped N atom at different positions of the structure. 4a and 4b are two resonance structures of the same molecule. Figure adapted from Ref. [38]. 18

Figure 1.9 One typical employed APEX method of PAHs. A hexaphenylbenzene molecule is used to synthesise a hexabenzocoronene (HBC) through the cyclo-dehydrogenation reaction. Figure adapted from Ref. [8]. 18

Figure 1.10 Quantum units in carbon-based materials with different strategies, including coulomb charging in nanotubes, endohedral inclusion in C_{60} molecules, edge functionalization of GNRs, and defects in graphenoids. Figure adapted from Ref. [39]. ...20

Figure 1.11 The chemical structures of a porphyrin and a related metalloporphyrin. The α-, β-, and meso-carbon are shown in the left schematic of porphine structure. M represents a metal ion incorporated in the right schematic of metalloporphyrin structure. Figure adapted from Ref. [20]. 21

Figure 1.12 Azopyridine functionalised Ni-porphyrin with light-induced magnetic-switching properties. The left one is the low-spin diamagnetic structure and the right one is the high-spin paramagnetic structure. Under blue-green radiation (500 nm), the low-spin state transforms to a high-spin state. However, under violet-blue radiation (435 nm), the high-spin state transforms to a low-spin state. Figure adapted from Ref. [45]. 21

Figure 1.13 Chemical structures of the copper(II)-based molecules. 1, 2, 3, 4, and 5 are the bridges used in porphyrin-based Cu–Cu dimers. 6 and 7 are the bridges used in porphyrin-based Cu–nitroxide. 8 is a nitroxide–nitroxide molecule. Figure adapted from Ref. [46]. .22

Figure 1.14 Chemical structures of a porphyrin ladder, a porphyrin nanoring, and a porphyrin nanotube. Two strands of porphyrins are connected by 4,4'-bipyridine molecules in the Zn-porphyrin ladder. Six Zn-porphyrin molecules are linked by butadiynes and a hexapyridyl ligand. The nanotube is composed of twelve Zn-porphyrin molecules, and every porphyrin molecule is π conjugated to three neighbouring porphyrin molecules. Figure adapted from Ref. [48-50]. 24

Figure 1.15 Chemical structure of the porphyrin ring, the scanning tunnelling microscopy (STM) images of the single-layer rings and triple-layer rings, and the influence of the stacking process on the shape and mechanical properties of the macromolecular aggregates. Figure adapted from Ref. [51]. 25

Figure 1.16 The schematic diagrams of the double- and triple-stranded complexes and their respective energy transfer times. The energy transfer time of double-stranded complexes is 1.25 ps. However, that of the triple-stranded complexes is much shorter, 0.65 ps. Figure adapted from Ref. [52]. 25

Figure 1.17 A: Chemical structure of a hexameric porphyrin with a guest of tripyridyl arene (TP) B: Chemical structure of a hexameric porphyrin with a guest of dipyridyl-substituted free base porphyrin (DPFb). Figure adapted from Ref. [53]. 27

Figure 1.18 The porphyrin dimer structures with different linkers on the left and the fused porphyrin dimer structure on the right. The linkers are shown at the bottom. Figure adapted from Ref. [54]. 27

Figure 1.19 Chemical structures of the heterometallated porphyrin dyads (D1, D2, and D3) with different spacers (S1, S2, and S3). Figure adapted from Ref. [55]. 28

Figure 1.20 a: XRD structure of these three molecules containing Cu(II) and Ti(III) with different separation distances. The *g* tensor frames of unpaired electron spins of Cu and Ti atoms are shown in the graph, respectively. b: The CW-EPR spectra of these three molecules using X-band in solution state at 77 K, respectively. Figure adapted from Ref. [6]. 30

Figure 1.21 (a) Nutation experiments of unpaired electron spins for these molecules, (2a: Cu-only complex, 2b: Ti-only complex). (b) Pulse sequences used to extract $<S_x>$, $<S_y>$, and $<S_z>$ and the Bloch representation of these pulse sequences. (c) Density matrices for ideal density matrices (black outline) and the measured density matrices (colour filling),

respectively. (d) The fidelity graphs of the monomers and dyads for these molecules. Figure adapted from Ref. [6].....31

Figure 2.1 (A) Diagram of energy levels of a spin-1/2 system in a magnetic field at X-band (9.5 GHz). The red line represents the transition frequency. (B) The corresponding derivative-like absorption spectrum. 32

Figure 2.2 Schematic diagram of a CW-EPR spectrometer. The function of each individual part of CW-EPR spectrometer is described in the main text. Figure adapted from Ref. [26]. 33

Figure 2.3 The amplitude of CW-EPR signal dependence on the microwave power. When the microwave power is small, the signal amplitude is proportional to the square root of the microwave power. However, when the microwave power is above a certain threshold, the signal decreases as the microwave power increases. Figure adapted from Ref. [26].....35

Figure 2.4 Schematic diagram of a pulsed EPR spectrometer. The function of each individual part of the pulsed EPR is shown in the main text. Figure adapted from Ref. [17].....37

Figure 2.5 The pulse sequence of Hahn echo and its corresponding illustration in the Bloch sphere. The π/2-pulse rotate a spin from +*z* direction to the *xy*-plane, and the π-pulse invert a spin's orientation in the xy plane. 39

Figure 2.6 Advanced pulse sequences for dynamical decoupling, including Hahn echo, CP, CPMG, XY4, XY8, XY16, and a pulse sequence (Picket fence recovery) for measuring T_1 [60]. 43

Figure 2.7 Time traces of T_m at 100 K by using different dynamical pulse sequences, including Hahn Echo, CPMG2, CPMG4, CPMG10, and CPMG20. As the number of π-pulses increases, the coherence time increases significantly. Figure adapted from Ref. [60]. 44

Figure 2.8 The pulse sequence of inversion recovery and its corresponding Bloch sphere illustration. The first π-pulse inverts a spin from spin-up state to spin-down state, the π/2-pulse rotates a spin from *z* direction into the *xy*-plane, and the second π-pulse inverts the spin's orientation in the *xy*-plane. 45

Figure 2.9 The pulse sequence of the Picket Fence and its corresponding illustration in the Bloch sphere. The original a series of π-pulses demagnetize the spin system, a π/2-pulse rotates a spin from *z* direction into *xy* plane, and a π-pulse inverts a spin's orientation in the *xy*-plane. 47

Figure 2.10 The schematic illustration of the spin–lattice-relaxation processes, including direct process (A), Orbach process (B), and Raman process (C). 49

Figure 2.11 The pulse sequence of the Rabi oscillations experiment and its corresponding Bloch sphere illustration. The first variable pulse rotates a spin in the Bloch sphere, and the specific position relies on the length and power of the microwave. The *z*-component then is detected using a Hahn-echo pulse sequence. 51

Figure 2.12 The pulse sequence of two-pulse ESEEM and its corresponding illustration in the Bloch sphere. The two-pulse ESEEM pulse sequence is the same as the Hahn echo. . 52

Figure 2.13 (A) Density matrix for an $S = ½$, $I = ½$ spin system. P represents polarization, NC represents nuclear coherence, EC_a represents allowed electron transitions, and EC_f represents forbidden electron transitions. (B) The corresponding energy-level diagram of this four-level system. The solid red lines represent nuclear coherence, the solid blue lines represent allowed electron coherence, and the dashed blue lines represent forbidden electron coherence. 54

Figure 2.14 The pulse sequence of three-pulse ESEEM. The first π/2-pulse generates electron coherence, the second π/2-pulse converts electron coherence into nuclear

coherence, and the final π/2-pulse converts nuclear coherence back into electron coherence. 55

Figure 2.15 The pulse sequence of HYSCORE. The first π/2-pulse generates electron coherence, the second π/2-pulse converts electron coherence into nuclear coherence, the third π-pulse mixes different nuclear coherence, and the final π/2-pulse converts nuclear coherence back into electron coherence. 56

Figure 2.16 Schematic diagram of the HYSCORE spectrum corresponding to a spin system with $S = 1/2$ and $I = 1/2$. This spectrum is the Fourier transformation result of the time-trace signal. The horizontal axis ν_1 corresponds to the Fourier transformation result of t_1 and the vertical axis ν_2 corresponds to the Fourier transformation result of t_2. The nontrivial peaks are the cross peaks from which we could extract hyperfine couplings. 58

Figure 3.1 Chemical structures of Oxovanadium(IV) and Vanadium(IV) complexes, and their corresponding coherence time and spin–lattice-relaxation times, respectively. Both the spin–lattice- and spin–spin-relaxation times of Oxovanadium(IV) are larger than that of vanadium(IV). Figure adapted from Ref. [72]. 62

Figure 3.2 Spin diffusion barrier model for $(Ph_4P)_2[VO(C_8S_8)_2]$ and $(Ph_4P)_2[V(C_8S_8)_3]$ in (a) 1:1 Dimethylformamide: Toluene and (b) 1:1 Dimethylformamide-d7:Toluene-d8, respectively. The purple colour represents the region, where the nuclear spins contribute to the decoherence of the unpaired electron spin. The blue colour represents the spin-diffusion-barrier region, where the nuclear spins almost do not contribute to the decoherence. The yellow colour represents the region where the nuclear-spin-free ligands replacing the solvent molecules. The green colour represents the region where the unpaired electron distributes. Figure adapted from Ref. [73]. 64

Figure 3.3 The left schematic shows the side view and top view of the chemical structure of the vanadyl–porphyrin monomer. The right schematic shows the electronic configuration of VO^{2+} ion. The unpaired electron resides in the d_{xy} orbital. 66

Figure 3.4 Electronic structure of vanadyl porphyrin monomer. The blue colour represents positive spin densities, and the red colour represents negative spin densities. The majority of unpaired electron-spin density resides on the vanadyl ion, and a little resides on the porphyrin ligand. 66

Figure 3.5 The structures of vanadyl porphyrins, including (A) butadiyne-linked vanadyl dimer, (B) acetylene-linked dimer, (C) singly linked dimer, (D) *syn*-triply fused, (E) *anti*-triply fused. 68

Figure 3.6 CW-EPR spectrum of vanadyl porphyrin monomer at Q-band. The blue line is the experiment result, the black line is the simulation result. 69

Figure 3.7 The comparison of the CW spectra of VO monomer from theory and experiment. 72

Figure 3.8 Schematic illustration of the *syn*-(A) and *anti*-(B) linked porphyrin dimers and the relative orientations of the different tensors. The subscripts 1, 2 and D represents the *g* tensors of the porphyrin units 1 and 2, and the dipolar or zero-field-splitting tensor, respectively. The blue rings represent the vanadyl porphyrin planes. The red, green, and blue axes stand for the *x*-axes, *y*-axes, and *z*-axes of these three tensors, respectively. 73

Figure 3.9 (A) Schematic illustration of the singly-linked porphyrin dimer and the relative orientations of the different tensors. (B) An alternative schematic illustration of the singly-linked porphyrin dimer and the relative orientations of the different tensors. The blue rings represent the vanadyl porphyrin planes. There is a twisting angle between the two planes. 78

Figure 3.10 Q-band CW-EPR spectra and corresponding fitting results of all vanadyl porphyrins at 140 K. The materials are dissolved in d8-toluene at a concentration of 1 mM and are in a frozen solution state. All the fitting parameters are listed in main text. 79
Figure 3.11 The spin density distributions of the *anti*-, *sl*-, *al*-, and *bl*-dimer in the triplet state (A, C, E, and G) and the singlet state (B, D, F, and H), respectively, with iso value 0.0002. Blue colour represents positive spin densities, and red colour represents negative spin densities. 82
Figure 3.12 (A) Local-minima-extracting method and (B) a fit of local-minima data. In the left graph, yellow circles represent the original data, the green line represents the filtered data after filtering low frequency noise, and the dark purple circles represent local minima extracted from the filtered data. In the right graph, the dark purple circles represent the local minima data, the blue line is the fit. 84
Figure 3.13 The Hahn-echo decay of the *anti*-dimer molecule at different temperatures and corresponding fits using a stretched-exponential model. 84
Figure 3.14 The comparison of T_m in molecules with different side groups, including tBu and THS-group in *sl*-linked dimer (A), *al*-linked dimer (B), and *bl*-linked dimer (C). The squares represent the results of molecules with THS side groups, the circles represent the results of molecules with tBu side groups. 86
Figure 3.15 The comparison of T_m in molecules connected by different linkers with different side groups, tBu (A) and THS (B). 88
Figure 3.16 The comparison of coherence times of *anti*- and *syn*-THS molecules. The blue points represent the T_m results of *anti*-THS molecule, and red points represent the T_m results of *syn*-THS molecule. 89
Figure 3.17 The spin–lattice-relaxation times (1) for monomer-THS (A), *syn*-THS (B), *anti*-THS (C), and the corresponding time traces of the spin–lattice-relaxation time

measurements and their fitting lines (2). Direct and Raman processes are considered as the main spin–lattice-relaxation mechanisms. 91

Figure 3.18 The spin–lattice-relaxation times (1) for *sl*-tBu (A), *al*-tBu (B), *bl*-tBu (C), and the corresponding time traces of the spin–lattice-relaxation time measurements and their fitting lines (2). Direct and Raman processes are considered as the main spin–lattice-relaxation mechanisms. 92

Figure 3.19 The spin–lattice-relaxation time for six molecules, respectively, in d8-toluene from 4 K to 80 K. 93

Figure 3.20 The EDFS spectrum of the standard sample and *anti*-dimer compound solution in d8-toluene at a concentration of 1mM with the pulsed-EPR experiment at 35 K using Q-band. 95

Figure 3.21 FFT results of the Rabi oscillations. The red line is the result of *anti*-dimer, and the blue line is the result of standard sample. 95

Figure 3.22 Time traces of Rabi oscillations (1), the corresponding FFT results (2), and the linear relationship between relative intensity of the pulse and the Rabi frequencies (3) in *sl*-dimer (A), *al*-dimer (B), and *bl*-dimer (C), in d8-toluene at 10 K. 96

Figure 3.23 The left graph shows the time trace of Hahn echo for the bl-linked dimer with different refocusing angles at 60 K at Q-band. The right graph shows extrapolating fit used to estimate the T_m without the influence of instantaneous diffusion. When refocusing angle approaches 0, T_m is 2.490 µs. 99

Figure 4.1 The chemical structure of cyclohepta[def]fluorene. The purple rings are the sextet structures. The red and blue circles represent different sublattices, including A and B... 104

Figure 4.2 Chemical structures of a family of benzo-extended cyclohepta[def]fluorene derivatives corresponding to the labels 1, 2, and 3. Mes represents the mesitylene group. 105

Figure 4.3 CW-EPR spectra of 1 (A), 2 (B), and 3 (C) molecules in d8-toluene solution, and their corresponding simulations at room temperature. The blue lines are the simulations and red lines are the experiment results. 106
Figure 4.4 The comparison of the CW-EPR d8-toluene solution spectra (A) and powder spectra (B) of these three molecules. 107
Figure 4.5 Half-field transitions of molecule 1 (A), 2 (B), and 3 (C) in powder states at 5 K and 293 K. 107
Figure 4.6 The calculated spin density distributions of molecules 1 (A), 2 (B), and 3 (C) in the triplet state with an iso value of 0.005. The functional is B3LYP/G, and the basis set is EPR-II. Blue colour represents positive spin densities, and red colour represents negative spin densities. 111
Figure 4.7 The comparison of the CW spectra of molecules 1 (A), 2 (B), and 3 (C) obtained from theory (DFT calculations) and experiment, respectively. 113
Figure 4.8 CW powder spectra at various temperatures of molecules 1 (A), 2 (C), and 3 (E), and their respective integrated signal intensity multiplied by the temperature at various temperatures with the fits using the Bleaney–Bowers equation (B, D, F), respectively. ..115
Figure 4.9 The inversion recovery and Hahn echo time traces of molecules 1 (A and B), 2 (C and D), and 3 (E and F) at 80 K at X-band, respectively. 117
Figure 4.10 The fast Fourier transform results of the Hahn echo time traces of molecules 2 and 3. 118
Figure 4.11 (A) The relaxation time T_1 (circle symbol) and T_m (square symbol) of molecules 1, 2, and 3, respectively, at different temperatures. (B) The stretch parameter was extracted from Hahn echo time traces of molecules 1, 2, and 3. 118
Figure 4.12 Rabi oscillations of molecule 1 in a d8-toluene solution at 80 K with different power attenuations (A), Fast Fourier transformation results of Rabi oscillations (B), and the

linear relationship between Rabi frequency and the relative strength of the microwave pulse (C). 121

Figure 5.1 The chemical structures of molecules 1 (A), 2 (B), and 3 (C). Mes represents the mesitylene group. The pink rings represent sextet structures. Defects with two disjoint five-membered rings are introduced in these three molecules. 127

Figure 5.2 CW solution spectra of 1 (A), 2 (B), and 3 (C), and their corresponding simulations at room temperature. 128

Figure 5.3 The comparison of the CW d8-toluene solution spectra of molecules 1 and 3 at room temperature at X-band. 130

Figure 5.4 The calculated spin density of molecules 1 (A), 2 (B), and 3 (C) in the triplet state with an iso value of 0.002. The functional is B3LYP/G, and the basis set is EPR-II. The red colour represents negative spin densities, and the blue colour represents positive spin densities. 132

Figure 5.5 The comparison of the CW spectra of molecules 1 (A) and 3 (B) obtained from theory and experiment, respectively. 134

Figure 5.6 The EDFS spectrum (A), the time trace of Hahn echo (B), the time trace of inversion recovery (C), and fast Fourier transformation results of a Hahn echo decay (D) of molecule 1 in d8-toluene solution at 10 K at X-band. 135

Figure 5.7 The temperature dependence of T_1 and T_m of these three molecules. The trend of coherence time vs. temperature can be divided into five regions. 135

Figure 5.8 Analysis of different spin–lattice-relaxation mechanisms across the whole temperature range of measurement of molecule 1 (A) and 3 (B) in d8-toluene solution at X-band frequency. The vertical black dashed line of 178 K corresponds to the melting temperature of the d8-toluene. 138

Figure A.0.1 HYSCORE experimental and simulation results of *syn*-dimer in d8-toluene at 20 K. 146

List of Abbreviations

al: acetylene linked

anti: triply linked with the opposite direction

APEX: annulative π-extension

bl: butadiyne linked

CW: continuous wave

DFT: density functional theory

EPR: electron paramagnetic resonance

HOMO: highest occupied molecular orbital

LUMO: lowest unoccupied molecular orbital

Mes: mesitylene group

mM: millimole per liter

p-HBC: hexa-peri-benzocoronene

PAH: polycyclic aromatic hydrocarbon

sl: singly linked

STM: scanning tunnelling microscopy

STS: scanning tunnelling spectroscopy

syn: triply linked with the same direction

tBu: tert-butyl group

THS: trihexylsilyl group

Publications

1. Wu, F., Ma, J., Lombardi, F., Fu, Y., Liu, F., **Huang, Z.**, Liu, R., Komber, H., Alexandropoulos, D.I., Dmitrieva, E. and Lohr, T.G., 2022. Benzo‐Extended Cyclohepta [def] fluorene Derivatives with Very Low‐Lying Triplet States. Angewandte Chemie, 134(23), p.e202202170.
2. Pozo, I., **Huang, Z.**, Lombardi, F., Alexandropoulos, D., Kong, F., Slota, M., Deng, J.R., Stawski, W., Horton, P., Coles, S. and Myers, W., 2023. Enhanced Coherence by Coupling Spins through a Delocalized π-System: Vanadyl Porphyrin Dimers.

References

[1] Ladd, T. D. *et al.* Quantum computers. *Nature* **464**, 45-53 (2010).

[2] Atzori, M. & Sessoli, R. The Second Quantum Revolution: Role and Challenges of Molecular Chemistry. *J Am Chem Soc* **141**, 11339-11352, doi:10.1021/jacs.9b00984 (2019).

[3] Kane, B. E. A silicon-based nuclear spin quantum computer. *Nature* **393**, 133-137 (1998).

[4] Pla, J. J. *et al.* A single-atom electron spin qubit in silicon. *Nature* **489**, 541-545 (2012).

[5] Graham, M. J., Zadrozny, J. M., Fataftah, M. S. & Freedman, D. E. Forging solid-state qubit design principles in a molecular furnace. *Chemistry of Materials* **29**, 1885-1897 (2017).

[6] von Kugelgen, S. *et al.* Spectral Addressability in a Modular Two Qubit System. *J Am Chem Soc* **143**, 8069-8077, doi:10.1021/jacs.1c02417 (2021).

[7] Wang, X.-Y., Narita, A. & Müllen, K. Precision synthesis versus bulk-scale fabrication of graphenes. *Nature Reviews Chemistry* **2**, 0100, doi:10.1038/s41570-017-0100 (2017).

[8] Yao, X. *Engineering peripheral structure in polycyclic aromatic hydrocarbons and graphene nanoribbons*, Johannes Gutenberg-Universität Mainz, (2019).

[9] Novoselov, K. S. *et al.* Electric field effect in atomically thin carbon films. *Science* **306**, 666-669 (2004).

[10] Wu, J., Pisula, W. & Müllen, K. Graphenes as potential material for electronics. *Chemical reviews* **107**, 718-747 (2007).

[11] Kosynkin, D. V. *et al.* Longitudinal unzipping of carbon nanotubes to form graphene nanoribbons. *Nature* **458**, 872-876 (2009).

[12] Narita, A., Wang, X.-Y., Feng, X. & Müllen, K. New advances in nanographene chemistry. *Chemical Society Reviews* **44**, 6616-6643 (2015).

[13] Wang, X.-Y., Yao, X. & Müllen, K. Polycyclic aromatic hydrocarbons in the graphene era. *Science China Chemistry* **62**, 1099-1144 (2019).

[14] Liu, J. & Feng, X. Synthetic tailoring of graphene nanostructures with zigzag-edged topologies: progress and perspectives. *Angewandte Chemie International Edition* **59**, 23386-23401 (2020).

[15] Ma, J. *Controlled Synthesis of Curved Nanographenes with Tunable Aromaticity*, Technische Universität Dresden, (2019).

[16] von Kugelgen, S. & Freedman, D. E. A chemical path to quantum information. *Science* **366**, 1070-1071 (2019).

[17] Lombardi, F. *Topological effects on the quantum properties of magnetic nanographene molecules*, University of Oxford, (2021).

[18] Son, Y.-W., Cohen, M. L. & Louie, S. G. Energy gaps in graphene nanoribbons. *Physical review letters* **97**, 216803 (2006).

[19] Borah, K. D. & Bhuyan, J. Magnesium porphyrins with relevance to chlorophylls. *Dalton Transactions* **46**, 6497-6509 (2017).

[20] Cremers, J. *Electronic communication in heterometallated porphyrin oligomers*. (Springer Nature, 2020).

[21] Ranieri, D. *et al.* An exchange coupled meso–meso linked vanadyl porphyrin dimer for quantum information processing. *Chemical Science* **14**, 61-69, doi:10.1039/d2sc04969d (2023).

[22] Griffiths, D. J. & Schroeter, D. F. *Introduction to quantum mechanics*. (Cambridge university press, 2018).

[23] Moise, G. *Exploiting EPR to elucidate fine and hyperfine interactions in complex chemical and biological systems*, University of Oxford, (2020).

[24] Slota, M. *Manipulating the coupling between electronic and spin degrees of freedom in molecules*, University of Oxford, (2017).

[25] Hayward, M. Quantum computing and shor's algorithm. *Sydney: Macquarie University Mathematics Department* (2008).

[26] Goldfarb, D. & Stoll, S. *EPR spectroscopy: fundamentals and methods*. (John Wiley & Sons, 2018).

[27] Schweiger, A. & Jeschke, G. *Principles of pulse electron paramagnetic resonance*. (Oxford University Press on Demand, 2001).

[28] Crocker, E. C. Application of the octet theory to single-ring aromatic compounds. *Journal of the American Chemical Society* **44**, 1618-1630 (1922).

[29] Pauling, L. & Wheland, G. W. The Nature of the Chemical Bond. V. The Quantum-Mechanical Calculation of the Resonance Energy of Benzene and Naphthalene and the Hydrocarbon Free Radicals. *The Journal of Chemical Physics* **1**, 362-374, doi:10.1063/1.1749304 (1933).

[30] von E. Doering, W. & Detert, F. L. Cycloheptatrienylium oxide. *Journal of the American Chemical Society* **73**, 876-877 (1951).

[31] Stabel, A., Herwig, P., Müllen, K. & Rabe, J. P. Diodelike Current–Voltage Curves for a Single Molecule–Tunneling Spectroscopy with Submolecular Resolution of an Alkylated,peri-Condensed Hexabenzocoronene. *Angewandte Chemie International Edition in English* **34**, 1609-1611, doi:10.1002/anie.199516091 (1995).

[32] Kastler, M., Schmidt, J., Pisula, W., Sebastiani, D. & Müllen, K. From armchair to zigzag peripheries in nanographenes. *Journal of the American Chemical Society* **128**, 9526-9534 (2006).

[33] Herwig, P. T. & Müllen, K. A Soluble Pentacene Precursor: Synthesis, Solid-State Conversion into Pentacene and Application in a Field-Effect Transistor. *Advanced Materials* **11**, 480-483, doi:10.1002/(sici)1521-4095(199904)11:6<480::Aid-adma480>3.0.Co;2-u (1999).

[34] Zuzak, R. *et al.* Higher Acenes by On-Surface Dehydrogenation: From Heptacene to Undecacene. *Angew Chem Int Ed Engl* **57**, 10500-10505, doi:10.1002/anie.201802040 (2018).

[35] Stępień, M., Gońka, E., Żyła, M. & Sprutta, N. Heterocyclic Nanographenes and Other Polycyclic Heteroaromatic Compounds: Synthetic Routes, Properties, and Applications. *Chemical reviews* **117**, 3479-3716 (2016).

[36] Zeng, Z. *et al.* Pro-aromatic and anti-aromatic π-conjugated molecules: an irresistible wish to be diradicals. *Chemical Society Reviews* **44**, 6578-6596, doi:10.1039/c5cs00051c (2015).

[37] Wu, F. *et al.* Benzo-Extended Cyclohepta [def] fluorene Derivatives with Very Low-Lying Triplet States. *Angewandte Chemie* **134**, doi:10.1002/ange.202202170 (2022).

[38] Stepien, M., Gonka, E., Zyla, M. & Sprutta, N. Heterocyclic Nanographenes and Other Polycyclic Heteroaromatic Compounds: Synthetic Routes, Properties, and Applications. *Chem Rev* **117**, 3479-3716, doi:10.1021/acs.chemrev.6b00076 (2017).

[39] Lombardi, F. *et al.* Quantum units from the topological engineering of molecular graphenoids. *Science* **366**, 1107-1110 (2019).

[40] Cubaynes, T. *et al.* Highly coherent spin states in carbon nanotubes coupled to cavity photons. *npj Quantum Information* **5**, doi:10.1038/s41534-019-0169-4 (2019).

[41] Mehring, M., Scherer, W. & Weidinger, A. Pseudoentanglement of spin states in the multilevel 15N@C60 system. *Phys Rev Lett* **93**, 206603, doi:10.1103/PhysRevLett.93.206603 (2004).

[42] Slota, M. *et al.* Magnetic edge states and coherent manipulation of graphene nanoribbons. *Nature* **557**, 691-695, doi:10.1038/s41586-018-0154-7 (2018).

[43] Dobriner, K. & Rhoads, C. The porphyrins in health and disease. *Physiological Reviews* **20**, 416-468 (1940).

[44] Perutz, M. F., Fermi, G., Luisi, B., Shaanan, B. & Liddington, R. C. Stereochemistry of cooperative mechanisms in hemoglobin. *Accounts of Chemical Research* **20**, 309-321 (1987).

[45] Venkataramani, S. *et al.* Magnetic bistability of molecules in homogeneous solution at room temperature. *Science* **331**, 445-448 (2011).

[46] Bowen, A. M. *et al.* Exploiting orientation-selective DEER: determining molecular structure in systems containing Cu(ii) centres. *Phys Chem Chem Phys* **18**, 5981-5994, doi:10.1039/c5cp06096f (2016).

[47] Wang, S.-P., Shen, Y.-F., Zhu, B.-Y., Wu, J. & Li, S. Recent advances in the template-directed synthesis of porphyrin nanorings. *Chemical Communications* **52**, 10205-10216, doi:10.1039/c6cc04556a (2016).

[48] Hoffmann, M. *et al.* Enhanced pi conjugation around a porphyrin[6] nanoring. *Angew Chem Int Ed Engl* **47**, 4993-4996, doi:10.1002/anie.200801188 (2008).

[49] Taylor, P. N. & Anderson, H. L. Cooperative self-assembly of double-strand conjugated porphyrin ladders. *Journal of the American Chemical Society* **121**, 11538-11545 (1999).

[50] Neuhaus, P., Cnossen, A., Gong, J. Q., Herz, L. M. & Anderson, H. L. A Molecular Nanotube with Three-Dimensional pi-Conjugation. *Angew Chem Weinheim Bergstr Ger* **127**, 7452-7456, doi:10.1002/ange.201502735 (2015).

[51] Svatek, S. A. *et al.* Mechanical stiffening of porphyrin nanorings through supramolecular columnar stacking. *Nano Lett* **13**, 3391-3395, doi:10.1021/nl4017557 (2013).

[52] Parkinson, P. *et al.* Ultrafast energy transfer in biomimetic multistrand nanorings. *J Am Chem Soc* **136**, 8217-8220, doi:10.1021/ja504730j (2014).

[53] Song, H.-e. *et al.* Mechanisms, pathways, and dynamics of excited-state energy flow in self-assembled wheel-and-spoke light-harvesting architectures. *The Journal of Physical Chemistry B* **110**, 19121-19130 (2006).

[54] Peeks, M. *Electronic delocalisation in linear and cyclic porphyrin oligomers*, University of Oxford, (2016).

[55] Fortage, J. *et al.* Single-step electron transfer on the nanometer scale: ultra-fast charge shift in strongly coupled zinc porphyrin-gold porphyrin dyads. *Chemistry* **14**, 3467-3480, doi:10.1002/chem.200701335 (2008).

[56] Richert, S. *Electron paramagnetic resonance studies and magnetic field effects on porphyrin nanostructures and triad systems*, University of Oxford, (2016).

[57] Soetbeer, J., Hülsmann, M., Godt, A., Polyhach, Y. & Jeschke, G. Dynamical decoupling of nitroxides in o-terphenyl: a study of temperature, deuteration and concentration effects. *Physical Chemistry Chemical Physics* **20**, 1615-1628, doi:10.1039/c7cp07074h (2018).

[58] Lombardi, F. *et al.* Dynamical nuclear decoupling of electron spins in molecular graphenoid radicals and biradicals. *Physical Review B* **101**, doi:10.1103/PhysRevB.101.094406 (2020).

[59] Souza, A. M., Alvarez, G. A. & Suter, D. Robust dynamical decoupling for quantum computing and quantum memory. *Phys Rev Lett* **106**, 240501, doi:10.1103/PhysRevLett.106.240501 (2011).

[60] Lombardi, F. *et al.* Room-temperature coherence boosting of molecular graphenoids by environmental spectral decomposition. *Physical Review B* **105**, doi:10.1103/PhysRevB.105.094106 (2022).

[61] Kveder, M., Rakvin, B. & You, J. A quantum many body model for the embedded electron spin decoherence in organic solids. *The Journal of Chemical Physics* **151**, 164124 (2019).

[62] Dimeo, R. Visualization and measurement of quantum rotational dynamics. *American Journal of Physics* **71**, 885-893 (2003).

[63] Šimėnas, M. *et al.* Magnetic excitation and readout of methyl group tunnel coherence. *Science advances* **6**, eaba1517 (2020).

[64] Usevičius, G. *et al.* Probing Methyl Group Tunneling in [(CH3) 2NH2][Zn (HCOO) 3] Hybrid Perovskite Using Co2+ EPR. *Molecules* **28**, 979, doi:10.3390/molecules28030979 (2023).

[65] Koch, W. & Holthausen, M. C. *A chemist's guide to density functional theory*. (John Wiley & Sons, 2015).

[66] Giustino, F. *Materials modelling using density functional theory: properties and predictions*. (Oxford University Press, 2014).

[67] Becke, A. D. Density-functional thermochemistry. I. The effect of the exchange-only gradient correction. *The Journal of Chemical Physics* **96**, 2155-2160, doi:10.1063/1.462066 (1992).

[68] Neese, F. Prediction of molecular properties and molecular spectroscopy with density functional theory: From fundamental theory to exchange-coupling. *Coordination Chemistry Reviews* **253**, 526-563, doi:10.1016/j.ccr.2008.05.014 (2009).

[69] Munzarová, M. L. DFT calculations of EPR hyperfine coupling tensors. *Calculation of NMR and EPR Parameters: Theory and Applications*, 461-482 (2004).

[70] Zadrozny, J. M., Niklas, J., Poluektov, O. G. & Freedman, D. E. Millisecond coherence time in a tunable molecular electronic spin qubit. *ACS central science* **1**, 488-492 (2015).

[71] Atzori, M. *et al.* Quantum Coherence Times Enhancement in Vanadium(IV)-based Potential Molecular Qubits: the Key Role of the Vanadyl Moiety. *J Am Chem Soc* **138**, 11234-11244, doi:10.1021/jacs.6b05574 (2016).

[72] Yu, C. J. *et al.* Long Coherence Times in Nuclear Spin-Free Vanadyl Qubits. *J Am Chem Soc* **138**, 14678-14685, doi:10.1021/jacs.6b08467 (2016).

[73] Zecevic, A. N. A., Eaton, G. R., Eaton, S. S. & Lindgren, M. Dephasing of electron spin echoes for nitroxyl radicals in glassy solvents by non-methyl and methyl protons. *Molecular Physics* **95**, 1255-1263, doi:10.1080/00268979809483256 (1998).

[74] Adamo, C. & Barone, V. Toward reliable density functional methods without adjustable parameters: The PBE0 model. *The Journal of chemical physics* **110**, 6158-6170 (1999).

[75] Casida, M. E. & Chong, D. Recent advances in density functional methods. *Computational Chemistry: Reviews of Current Trends* (1995).

[76] Ikeue, T. *et al.* The Importance of a β–β Bond for Long-Range Antiferromagnetic Coupling in Directly Linked Copper (II) and Silver (II) Diporphyrins. *Angewandte Chemie International Edition* **44**, 6899-6901 (2005).

[77] Wili, N. *et al.* ELDOR-detected NMR beyond hyperfine couplings: a case study with Cu (ii)-porphyrin dimers. *Physical Chemistry Chemical Physics* **21**, 11676-11688 (2019).

[78] Biktagirov, T. *et al.* In situ identification of various structural features of vanadyl porphyrins in crude oil by high-field (3.4 T) electron–nuclear double resonance spectroscopy combined with density functional theory calculations. *Energy & Fuels* **31**, 1243-1249 (2017).

[79] McInnes, E. J. & Collison, D. EPR interactions–coupled spins. *EPR Spectroscopy: Fundamentals and Methods*, 63 (2018).

[80] Eaton, S. S., More, K. M., Sawant, B. M. & Eaton, G. R. Use of the ESR half-field transition to determine the interspin distance and the orientation of the interspin vector in systems with two unpaired electrons. *Journal of the American Chemical Society* **105**, 6560-6567 (1983).

[81] Bennie, S. *Theoretical Calculations of the Magnetic Properties of Inorganic Molecules*. (The University of Manchester (United Kingdom), 2013).

[82] Yamaguchi, K., Jensen, F., Dorigo, A. & Houk, K. A spin correction procedure for unrestricted Hartree-Fock and Møller-Plesset wavefunctions for singlet diradicals and polyradicals. *Chemical physics letters* **149**, 537-542 (1988).

[83] Bae, Y. *et al.* Enhanced quantum coherence in exchange coupled spins via singlet-triplet transitions. *Science Advances* **4**, eaau4159 (2018).

[84] Baart, T. A., Fujita, T., Reichl, C., Wegscheider, W. & Vandersypen, L. M. K. Coherent spin-exchange via a quantum mediator. *Nature Nanotechnology* **12**, 26-30, doi:10.1038/nnano.2016.188 (2017).

[85] Lombardi, F. *et al.* Synthetic tuning of the quantum properties of open-shell radicaloids. *Chem* **7**, 1363-1378, doi:10.1016/j.chempr.2021.03.024 (2021).

[86] Clough, S. & Poldy, F. Tunnelling rotation rate of a weakly hindered methyl group (epr and ENDOR measurements). *Journal of Physics C: Solid State Physics* **6**, 1953 (1973).

[87] Sørnes, A. R. *et al.* Effect of isotopic substitution on the electron spin dynamics of the CH3Ċ (COOH) 2 radical in X-irradiated methyl malonic acid powder: intrinsic

potentials and activation energies. *The Journal of Physical Chemistry A* **101**, 8987-8994, doi:10.1021/jp972067n (1997).

[88] Clough, S. & Hill, J. Temperature dependence of methyl group tunnelling rotation frequency. *Journal of Physics C: Solid State Physics* **7**, L20 (1974).

[89] Amdur, M. J. *et al.* Chemical control of spin-lattice relaxation to discover a room temperature molecular qubit. *Chem Sci* **13**, 7034-7045, doi:10.1039/d1sc06130e (2022).

[90] Portella, G., Poater, J. & Solà, M. Assessment of Clar's aromatic π-sextet rule by means of PDI, NICS and HOMA indicators of local aromaticity. *Journal of Physical Organic Chemistry* **18**, 785-791, doi:10.1002/poc.938 (2005).

[91] Clar, E. Aromatic sextet. (1972).

[92] Lieb, E. H. Two theorems on the Hubbard model. *Physical review letters* **62**, 1201 (1989).

[93] Vergés, J., Chiappe, G., Louis, E., Pastor-Abia, L. & SanFabián, E. Magnetic molecules created by hydrogenation of polycyclic aromatic hydrocarbons. *Physical Review B* **79**, 094403 (2009).

[94] Eaton, S. S. & Eaton, G. R. Measurement of spin-spin distances from the intensity of the EPR half-field transition. *Journal of the American Chemical Society* **104**, 5002-5003 (1982).

[95] Chang, C. K. & Abdalmuhdi, I. A Biphenylenediporphyrin: Two Cofacially Arranged Porphyrins with a Biphenylene Bridge. *Angewandte Chemie International Edition in English* **23**, 164-165 (1984).

[96] Bleaney, B. & Bowers, K. Anomalous paramagnetism of copper acetate. *Proceedings of the Royal Society of London. Series A. Mathematical and Physical Sciences* **214**, 451-465 (1952).

[97] McMasters, D. R. & Wirz, J. Spectroscopy and Reactivity of Kekulé Hydrocarbons with Very Small Singlet−Triplet Gaps. *Journal of the American Chemical Society* **123**, 238-246, doi:10.1021/ja0004377 (2001).

[98] Wang, K. *et al.* A Robust Porphyrin-Stabilized Triplet Carbon Diradical. *Angewandte Chemie International Edition* **60**, 7002-7006 (2021).

[99] Tsvetkov, Y. D. & Dzuba, S. Pulsed ESR and molecular motions. *Applied Magnetic Resonance* **1**, 179-194 (1990).

[100] Nakagawa, K., Candelaria, M. B., Chik, W. W., Eaton, S. S. & Eaton, G. R. Electron-spin relaxation times of chromium (V). *Journal of Magnetic Resonance (1969)* **98**, 81-91 (1992).

[101] Robinson, B. H., Haas, D. A. & Mailer, C. Molecular dynamics in liquids: spin-lattice relaxation of nitroxide spin labels. *Science*, 490-493 (1994).

[102] Sato, H. *et al.* Electron spin–lattice relaxation of nitroxyl radicals in temperature ranges that span glassy solutions to low-viscosity liquids. *Journal of magnetic resonance* **191**, 66-77 (2008).

[103] Wasielewski, M. R. *et al.* Exploiting chemistry and molecular systems for quantum information science. *Nature Reviews Chemistry* **4**, 490-504, doi:10.1038/s41570-020-0200-5 (2020).

[104] DiVincenzo, D. P. The physical implementation of quantum computation. *Fortschritte der Physik: Progress of Physics* **48**, 771-783 (2000).

[105] Gallagher, N. M., Olankitwanit, A. & Rajca, A. High-Spin Organic Molecules. *The Journal of Organic Chemistry* **80**, 1291-1298, doi:10.1021/jo502505r (2015).

[106] Mirzoyan, R., Kazmierczak, N. P. & Hadt, R. G. Deconvolving Contributions to Decoherence in Molecular Electron Spin Qubits: A Dynamic Ligand Field Approach. *Chemistry – A European Journal* **27**, 9482-9494, doi:10.1002/chem.202100845 (2021).

[107] Eaton, S. S. & Eaton, G. R. Relaxation times of organic radicals and transition metal ions. *Distance measurements in biological systems by EPR*, 29-154 (2000).

[108] Canarie, E. R., Jahn, S. M. & Stoll, S. Quantitative structure-based prediction of electron spin decoherence in organic radicals. *The journal of physical chemistry letters* **11**, 3396-3400 (2020).

[109] Jeschke, G. Rotational Coupling in Methyl-Tunneling Electron Spin Echo Envelope Modulation. *Applied Magnetic Resonance* **53**, 635-651, doi:10.1007/s00723-021-01375-6 (2022).

[110] Cavagnat, D., Magerl, A., Vettier, C. & Clough, S. Methyl tunnelling in α-crystallised toluene by inelastic neutron scattering: temperature and pressure effects. *Journal of Physics C: Solid State Physics* **19**, 6665 (1986).

[111] Brown, I. Electron spin-echo envelope decays and molecular motion: Rotational and translational diffusion. *The Journal of Chemical Physics* **60**, 4930-4938 (1974).

[112] Zecevic, A., Eaton, G. R., Eaton, S. S. & Lindgren, M. Dephasing of electron spin echoes for nitroxyl radicals in glassy solvents by non-methyl and methyl protons. *Molecular Physics* **95**, 1255-1263 (1998).